

Level crossings and chiral transitions in transverse-field Ising models of adatom and Rydberg chains

Présentée le 2 juin 2022

Faculté des sciences de base
Chaire de théorie de la matière condensée
Programme doctoral en physique

pour l'obtention du grade de Docteur ès Sciences

par

Ivo AGUIAR MACEIRA

Acceptée sur proposition du jury

Prof. P. Ricci, président du jury
Prof. F. Mila, directeur de thèse
Prof. H. Pichler, rapporteur
Prof. B. Kumar, rapporteur
Prof. A. Läuchli, rapporteur

Abstract

Cette thèse est motivée par de récentes expériences sur des systèmes décrits par des extensions du modèle unidimensionnel d'Ising à champ transverse (TFI) où (1) des propriétés des phases ordonnées d'Ising – des croisements de niveaux de l'état fondamental – ont été observées et (2) des transitions de phase continues liées au modèle \mathbb{Z}_2 p-state chiral clock ont été étudiées, avec des résultats intéressants mais pas totalement concluants sur la nature des transitions de phase et l'existence d'une classe d'universalité chirale.

Pour (1), la relation entre les croisements de niveau et les modes de bord protégés topologiquement des modèles de fermions de Majorana est discutée, et il est démontré que le temps d'auto-corrélation des spins de bord peut être infini même pour des systèmes non intégrables, indépendamment de la température. Ensuite, les croisements de niveaux sont réinterprétés dans le contexte de la théorie des perturbations dégénérées comme étant une conséquence de l'interférence quantique destructive entre des processus d'effet tunnel impliquant différents nombres de retournement de spin. On montre que ce phénomène est indépendant de la géométrie du réseau et qu'il est omniprésent dans les modèles de type TFI, se retrouvant aussi dans les systèmes à spin- S unique, ces derniers ayant déjà été observés dans le domaine des molécules magnétiques. L'effet du désordre sur les croisements est étudié à l'ordre le plus bas.

Pour (2), nous effectuons des simulations de groupe de renormalisation de matrice de densité pour étudier les transitions de phase quantiques observées expérimentalement et nous concluons que des points critiques conformes existent sur les frontières critiques $p = 3$ et $p = 4$: nous localisons précisément ces points et caractérisons leurs classes d'universalité (CU), où nous trouvons que le point $p = 3$ correspond à la CU du modèle de Potts à 3 états et que le point $p = 4$ correspond à la CU d'Ashkin-Teller avec $\nu \simeq 0.80$ ($\lambda \simeq 0.5$). Nos résultats sont en faveur de l'existence de lignes de transition chirale entourant les points conformes, au-delà desquelles une phase intermédiaire sans gap est attendue.

Abstract

This thesis is motivated by recent experiments on systems described by extensions of the one-dimensional transverse-field Ising (TFI) model where (1) finite-size properties of Ising-ordered phases – specifically, ground state level crossings – were observed and (2) continuous phase transitions related to the p -state chiral clock model were probed, with interesting but only partially conclusive results regarding the nature of the phase transitions and the possible existence of a chiral universality class.

For (1), the relation of the level crossings to topologically protected edge modes of Majorana fermion models is discussed, and the implication is made explicit that the auto-correlation time of the edge spins may be infinite even for non-integrable albeit finite systems, and independently of temperature. The level crossings are then reinterpreted in the context of degenerate perturbation theory as being a consequence of destructive quantum interference between tunneling processes involving different numbers of spin-flip operations. It is shown that this phenomenon is independent of the lattice geometry, as long as this one is not geometrically frustrated, and is ubiquitous to TFI-like models, being also found in single spin- S systems, the latter having already been observed in the field of magnetic molecules. The effect of disorder on the crossings is studied in lowest order.

For (2), we perform density matrix renormalization group simulations on open chains to investigate the experimentally observed quantum phase transitions and we conclude that isolated conformal critical points exist along the $p = 3$ and $p = 4$ critical boundaries: we accurately locate such points and characterize their universality classes by determining critical exponents numerically, where we find that the $p = 3$ agrees with a 3-state Potts universality class and the $p = 4$ point agrees with an Ashkin-Teller universality class with $\nu \simeq 0.80$ ($\lambda \simeq 0.5$). Our results are in favor of the existence of chiral transition lines surrounding the conformal points, beyond which a gapless intermediate phase is expected.

Acknowledgements

I am thankful to Markus Müller¹, whose idea of how to analytically calculate the spin cluster tunneling amplitudes led to the most extensive work done during my thesis. I am thankful to Natalia Chepiga² for her advice on the efficient implementation of the DMRG algorithm and for her physical insight on the interpretations of its numerical results. I am also thankful to Ramasubramanian Chitra³ and Paolo Mognini⁴, with whom I started an interesting project studying ground state level crossings in Floquet models, which was unfortunately not completed. Finally, I am thankful to my advisor Frédéric Mila⁵, especially for giving me the freedom to work at my own pace, but also for giving me many opportunities to collaborate and to find my way in the scientific community.

Furthermore, this thesis was supported by the Swiss National Science Foundation and the Portuguese Science and Technology Foundation through the grant SFRH/BD/117343/2016.

¹markus.mueller@psi.ch , Paul Scherrer Institute (PSI), Condensed Matter Theory, CH-5235 Villigen, Switzerland

²n.chepiga@tudelft.nl , Department of Quantum Nanoscience, Kavli Institute of Nanoscience, Delft University of Technology, Lorentzweg 1, 2628 CJ Delft, The Netherlands.

³chitrar@ethz.ch , Institut für Theoretische Physik, HIT K 42.4, Wolfgang-Pauli-Str. 27, 8093 Zürich, Switzerland

⁴pm728@cam.ac.uk , TCM Group, Cavendish Laboratory, 19 JJ Thomson Avenue, Cambridge, CB3 0HE UK

⁵frederic.mila@epfl.ch , Institute of Physics, École Polytechnique Fédérale de Lausanne (EPFL), CH-1015 Lausanne, Switzerland.

Contents

1	Introduction	1
1.1	Continuous phase transitions	1
1.1.1	The Ising model	1
1.1.2	Renormalization	2
1.1.3	Conformal invariance	2
1.1.4	Topological order	3
1.1.5	The transverse-field Ising model	4
1.2	Quantum simulators	4
1.2.1	Scanning tunneling microscopy	5
1.2.2	Optical traps	6
1.3	Thesis overview	8
1.3.1	Ground state level crossings in TFI-like chains	8
2	Infinite coherence time of edge spins in finite-length chains	11
2.1	Introduction	11
2.2	Models	13
2.2.1	XY-Z Majorana edge fermions	13
2.2.2	XZ-Z prethermal strong zero mode	15
2.2.3	Level crossings	16
2.3	Edge spin time correlation	18
2.3.1	XY-Z correlation	18
2.3.2	XZ-Z correlation	20
2.3.3	Edge vs. bulk	23
2.4	Summary and discussion	25
2.A	The Kitaev model	25
3	Perturbative approach to tunneling and QI in spin clusters	29
3.1	Introduction	29
3.2	Models	32
3.2.1	Ising model with transverse field and exchange	33

3.2.2	Ising model with a staggered field	35
3.2.3	Ising model with general transverse couplings	35
3.2.4	Single spin model	38
3.3	Perturbation theory for collective tunneling	39
3.3.1	Tunneling in Ising models with transverse field and ex- change	42
3.3.2	Tunneling in Ising models with a staggered field	44
3.3.3	Tunneling in Ising models with general transverse cou- plings	44
3.4	Tunneling in 1D systems	46
3.4.1	Closed chain: a ring of spins	46
3.4.2	Open Ising spin chains	50
3.5	2D and 3D clusters	52
3.6	Weak Disorder	57
3.7	Tunneling in single spin models	59
3.7.1	Exact degeneracies of single spin model	61
3.8	Other systems with competing tunneling channels	62
3.9	Summary and outlook	63
3.A	Deduction of method	65
3.B	Cluster independence	68
3.C	General derivation of zeros in single spin model	71
4	Conformal and chiral phase transitions in Rydberg chains	73
4.1	Commensurate-Incommensurate transitions	73
4.1.1	Chiral clock models	73
4.1.2	The Rydberg model	75
4.1.3	Blockade models	75
4.2	The DMRG Algorithm	78
4.2.1	Singular value decomposition of tensors	78
4.2.2	Full tensor decomposition	79
4.2.3	Tensor representation of quantum objects	80
4.2.4	The one-site DMRG algorithm	82
4.2.5	Optimal contraction order	82
4.2.6	Why DMRG works	84
4.2.7	Convergence of DMRG	86
4.2.8	Two-site DMRG	87
4.2.9	The starting MPS	88
4.2.10	Implementation	89
4.3	DMRG implementation of the Rydberg model	89

4.3.1	MPO form of the Hamiltonian	89
4.3.2	Correlations and q-vector	90
4.3.3	Convergence	93
4.4	Results	93
4.4.1	Period-2 cuts	94
4.4.2	The product criteria	95
4.4.3	Procedure for period-3 and 4 phases	95
4.4.4	Determining the P and AT cuts	96
4.4.5	Period-3 cuts	96
4.4.6	Period-4 cuts	100
4.4.7	Order parameter scaling	100
4.4.8	Finite-size scaling	102
4.4.9	Floating phase boundary	103
4.5	Comparing with previous work	105
4.5.1	The Kibble-Zurek exponent	106
5	Future work	109

Chapter 1

Introduction

This thesis is based on three articles published during the course of the PhD, the first two being closely related in their subject matter [1, 2], with the last one being a separate line of research [3]. Each of them is presented in its own chapter with some adaptations, and this introduction aims to connect the three chapters by contextualizing them in the broader picture of statistical physics and condensed matter, both theoretical and experimental. While this introduction is not essential in the sense that each chapter could stand on its own, here we present some of the concepts used throughout the thesis as they were introduced historically and with a focus on their impact and/or limitations, without going into details and exact definitions, as only a thorough survey through the cited literature would do justice to these complex subjects. Review articles and books are cited as [–, Review].

In this introduction, we start with a review of some of the theoretical advances in the subject of continuous phase transitions, which will be especially relevant for Chapter 4. We then briefly review the experimental techniques which made the research in this thesis relevant, and we present the main topics of this thesis in the context of such experiments.

1.1 Continuous phase transitions

1.1.1 The Ising model One of the paradigmatic models in statistical and condensed matter physics is the Ising model [4]. Introduced to explain the emergence of ferromagnetism from the interaction of individual microscopic degrees of freedom, it failed to show a continuous phase transition at a finite temperature in 1D [4]. Years later, the Ising model on a 2D square lattice was solved [5]: Its partition function was analytically determined and it was the first exactly solved model featuring a continuous phase transition, this one between a (anti-)ferromagnetic phase and a disordered phase at high temperatures, demonstrating that the partition function formalism is sufficient to describe critical phenomena, provided it can be computed exactly.

The proof also demonstrated the asymptotic scale-free behavior of thermodynamic quantities like the order parameter (magnetization) as we approach the non-analytic critical point.

1.1.2 Renormalization The properties of critical points and their surrounding were further elucidated by the renormalization group formalism [6, 7][8, 9, Reviews], in which critical points are fixed points of a renormalization group flow in a possibly infinite space of Hamiltonians. The correlation length can only decrease along the renormalization flow lines, so the fixed points of the renormalization group flow must necessarily have zero correlation length for attractive fixed points or infinite correlation length when they have at least one flow line that points outwards from the fixed point, the latter corresponding to critical points. The scale invariance at the critical point lets us determine most critical exponents from a linearization of the recursive flow equations at the critical point. Renormalization also explains the origin of the scaling relations between critical exponents, and provides a partial explanation for the universality of the families of critical exponents, as some Hamiltonians might flow out of their parameter space through irrelevant perturbations towards the critical fixed point of a simpler model.

However, renormalization does not fully explain universality: Assuming all the scaling relations hold true, they leave room for a 2-dimensional space of two independent critical exponents, all others being determined by the scaling relations, and yet most of this space is never realized, while a few points of this space appear everywhere in physics. Also, the renormalization group procedure cannot be applied exactly except in a few cases, so most of the time we are left without accurate exponent predictions.

1.1.3 Conformal invariance Another line of progress started when it was realized that the full emergent symmetry at the critical point of most theories was conformal symmetry [10], which extends scale invariance. In that case, the Hamiltonian at the critical point is connected through a continuum limit to a conformal field theory (CFT). CFTs in two dimensions are special in that the 2D conformal group spans all the analytic functions on the complex plane, which are locally-conformal, so the group has an infinite number of generators. This imposes a large restriction in the form of the correlation functions and leads to many more exact results on 2D CFTs than in higher dimensions [11]. 2D CFTs are characterized by their central charge c and the scaling dimensions of the associated primary fields. All the possible CFTs with a finite number of primary fields have been determined and classified

as a series known as the minimal models [11, 12]. All the minimal models have $c < 1$, and there is no undetermined parameter that continuously tunes the central charge and scaling dimensions: these quantities are fixed at certain rational numbers. If one further requires unitarity, then the central charge and the scaling dimensions are all non-negative fractions [13]. The unitary minimal models can be uniquely classified and ordered in a sequence of increasing central charge, and the first few CFTs of the series have been identified as the universality classes of several well-known statistical models [11, 14, 13], the Ising critical point corresponding to the first non-trivial CFT in the series. Thus, on the two-dimensional space of possible conformal universality classes, enough restrictions can be imposed through 2D CFT such that isolated universality classes appear, and the Ising universality class is an extreme case in this space, and this last point also seems to hold in three dimensions [15, 16]. There are also important unitary CFTs with $c \geq 1$, but in this case a continuum of universality classes can be found, as is the example of the Ashkin-Teller universality class with $c = 1$, which is parametrized by a coupling λ .

While conformal field theory seems to be a definitive answer to a lot of the critical behavior we observe, conformal phase transitions do not amount to all the possible and relevant phase transitions. For example, in models which break rotational symmetry either explicitly in the Hamiltonian or through emergent chiral degrees of freedom, the full conformal symmetry on critical points is lost, although scale invariance remains. We shall see some examples of these models in Chapter 4. Other phase transitions show unconventional (or no) signs of emergence of order, as we will see next.

1.1.4 Topological order Some phase transitions are still critical, in the sense that correlations become power-law at the critical point, but don't completely fit with the regular picture of continuous phase transitions. For example, in the Kosterlitz-Thouless (KT) transition [17] of the 2D classical XY model the correlation length diverges exponentially and remains infinite below the critical temperature, while no symmetry-breaking occurs across the transition [18].

Another famous example of irregular phases of matter is the gapped Haldane phase of the spin-1 Heisenberg chain [19], where open chains have four-fold degenerate ground states while no local order parameter is finite [20, 21], although a non-local order parameter can be defined [22]. The ground state degeneracy of open chains can be understood as a consequence of effective spin-1/2 degrees of freedom that are localized at both edges of the chain,

which are exactly decoupled in the AKLT limit of the spin-1 chain [20, 21]. In contrast, when the chain is closed into a ring, the now interacting spin-1/2s at the edges will form a singlet [20] and thus a single ground state is observed in this phase when the boundary is periodic.

The Haldane phase was the first example of a symmetry-protected topological (SPT) phase [23]. In such phases, the ground state is guaranteed to be degenerate due to the existence of zero energy excitations (zero modes) which are symmetry-protected and are localized at the edges of systems with open boundaries. Surprisingly, while no such modes are present for periodic boundaries, in fermionic systems one can instead define an integral of some geometric function of the dispersion relation over the Brillouin zone that can only take discrete values and which indicates the number of edge excitations observed for open boundaries [24, 25, 26], thus both approaches (periodic or open) can lead to the identification of such phases. This connection between a geometric bulk quantity and edge excitations is known as the bulk-edge correspondence [27][28, Review]. Perturbations of the model that preserve its symmetry will also preserve the number of existing zero modes. For such perturbations, only if the Hamiltonian becomes gapless (quantum critical point) can the number of zero modes change.

1.1.5 The transverse-field Ising model The model which is at the basis for all the work in this thesis, the one-dimensional transverse-field Ising (TFI) model [29], is right at the intersection of conventional ordered phases and of topological order. All the models we will be concerned with are extensions of this model, which is an important minimal model in that it can be exactly solved in terms of free fermions and also features a continuous quantum phase transition, that is, a zero temperature phase transition that is driven by a quantum coupling instead of the temperature or other thermodynamic quantities. The TFI phase transition is in fact in the 2D classical Ising universality class. Without solving the model, this can be proved by a mapping between the partition functions of both systems, which is a particular case of a general mapping between the partition functions of quantum systems in D dimensions and corresponding classical systems in $D + 1$ dimensions [30][31, Sec. 5.6, Review]. The exact mapping between spins and fermions allows the reinterpretation of the Ising ordered phase as an SPT phase where the zero modes at the edges are Majorana fermions [32], as we will see in more detail in Chapter 2.

1.2 Quantum simulators Some efforts in experimental physics try to push the boundaries of what current techniques are capable of in the hope of tack-

ling still-open questions in two or more dimensions through the design of systems that could model arbitrary quantum Hamiltonians. In the meantime, some experimental achievements of the past few decades have already made much more accessible experimentally what was already reachable theoretically – in particular in 1D quantum physics – encouraging theorists to revisit somewhat forgotten problems and build upon past ideas, which is the spirit of this thesis. Two experimental advances are precursors to the work presented here: the scanning tunneling microscope (STM), and optical traps of neutral atoms.

1.2.1 Scanning tunneling microscopy In scanning tunneling microscopy, a conducting probe ending at a sharp tip is lowered in a controlled manner close to a bulk surface, at distances of the order of the nanometer, not close enough for atoms to chemically bind and so create a conductive channel, but close enough to allow for significant tunneling of electrons to occur across the vacuum between the electron clouds of tip and surface, so that a tunneling current is observed when a voltage bias is applied. This technique allowed for the first direct “observations” of individual atoms [33, 34]. To achieve such precision, the tip of the probe must be extremely sharp and terminating in just a few atoms, possibly down to a single atom [35].

One can image the surface by sweeping different voltage biases V and calculating the differential conductance dI/dV , which is approximately proportional to the local electron density. One can also image in this way lone atoms that were adsorbed, so-called *adatoms*: atoms that attached (often weakly) to the bulk surface and are now single “defects” on top of a surface. If the tip moves too close to an adsorbed atom, the atom might prefer to attach to the tip. This increased influence of the tip on the sample can be exploited to remove, move, and place individual atoms [36], and thus it is possible to create quantum structures atom by atom [36, 37][38, Review].

If the STM tip is magnetically polarized, the tunneling current becomes sensitive to the spin state of the electrons [39, 40, 41], so it’s possible to obtain the local magnetic states of surfaces or of the adatoms on them. The possibility then arises of building adatom systems which are effectively described by minimal models like the Ising model (TFI-like by applying an external field) and which can be probed magnetically with great accuracy. This was realized successfully not so long ago with experiments on 1D chains of Cobalt adatoms [42], the results of which started the line of research which lead to Chapters 2 and 3 of this thesis.

The STM [33, 34, 43] and its offspring the atomic force microscope [44,

45] have become standard tools in many condensed matter labs and other fields with plenty of applications [46, 47, 48, Reviews]. This type of microscopes are collectively called scanning probe microscopes (SPM) [49, 50, Reviews].

Even with the great versatility they provide, structures of adatoms on surfaces controlled by SPMs might not classify completely as quantum simulators, in the sense that one does not have full control over all of the model parameters: For example, interaction couplings between adatoms only take discrete values set by the possible distances between them, since adatoms naturally adsorb at symmetry points of the underlying lattice. However, the underlying discreteness could be made irrelevant if a universal quantum computer were to be built from such systems [51]. Still, the next technique we present seems to be some steps closer towards that goal.

1.2.2 Optical traps Trapping neutral particles in a small region of space is a problem of its own, as obviously one cannot exploit strong electromagnetic fields for the confinement. In 1970, after the then-recent invention of the laser, it was demonstrated how focused laser beams can be used to trap transparent neutral particles of sizes of the order of the incident beam wavelength [52]. At such scales, the stability of the particle inside the laser can be understood with classical optics as an imbalance of momentum transfers from refracting rays of light of different intensities if the particle is not at the center of the beam where intensity is maximal [52]. The resulting force is approximately proportional to the gradient of the intensity. A uniform-width beam will also push the particle forward, but this can be counteracted by focusing the beam at a point, creating a single point of highest beam intensity which is effectively the center of a potential well for the particle [52].

Such an intensity gradient force is also observed for particles much smaller than the laser wavelength [53][54, Review], in which case the light beam can be seen as an average electromagnetic field from the point of view of the particle. In this regime the gradient force is due to the interaction between the electric field and a (possibly induced) electric dipole moment of the particle, thus the force is also proportional to the polarizability of the particle.

The average time that particles remain trapped is greatly influenced by their thermal velocity, thus better cooling techniques were essential to improve this measure. In particular, six-beam configurations distributed in pairs¹ along orthogonal axes, all focusing on a single point, were used to optically

¹One of the beams of each pair can be replaced by a mirror, thus achieving the same with three beams.

cool neutral atoms [55, 56, 57]: Tuning the lasers at a slightly lower frequency than a specific electronic transition, one can exploit the Doppler shift seen by atoms moving towards the beam sources, which brings the laser frequency closer to resonance, and so has a cooling effect on faster atoms. The development of this technique lead to the first optically trapped clouds of neutral atoms [55, 56].

The stability and cooling of the six-beam trap can be enhanced with a spatially-varying magnetic field [58], forming what are called magneto-optical traps [59, Review], which were later used in the first experimental observations of Bose-Einstein condensation [60, 61]. Many experiments nowadays use some combination of these techniques: A common experimental setup is to load single-beam optical traps with single atoms coming from a cooled cloud of atoms in a magneto-optical trap [62]. Atoms can then be set to interact with each other by setting single-atom traps close to each other, and one can continuously tune the inter-atomic interaction by adjusting the trap spacing.

The emphasis of many such experiments is on single-atom traps of Rydberg atoms[63, Review]: atoms with very large principal quantum number, either from a naturally large atomic number or from valence electrons in highly excited states, or both². These atoms have a very large electric dipole moment given their equally large atomic radius, which could be increased even further through electron excitations at very little cost due to the high density of atomic levels close to the vacuum energy. Optically trapped atoms can be excited to a chosen Rydberg state with lasers of appropriate frequencies.

Interactions between Rydberg atoms have been extensively probed using optical traps, starting with the interaction between two atoms in different traps [64, 65], demonstrating a repulsive dipole-dipole interaction ($\sim r^{-3}$) between atoms in Rydberg states which suppresses simultaneous excitations when the atoms are close enough to each other, in what is known as the Rydberg blockade, its uses having been recognized before [66, 67]. If the two atoms are excited to the same Rydberg state and are at sufficient distance from each other, the direct dipole coupling vanishes and the leading interactions are of Van der Walls type ($\sim r^{-6}$) [68, 69, Reviews][70].

The single-atom traps can be arranged in 1D [71] or 2D [72, 73] geometries to create optical lattices on which Rydberg atoms interact and effectively simulate minimal models with highly tunable parameters [74]. Of particular interest to us is a set of experiments of this kind where a 1D array of Rydberg

²Rubidium-87 atoms are an example of such atoms which are used particularly often, for reasons that escaped me during my survey.

atoms realized a TFI-like Hamiltonian with long-range Van der Waals interactions [75, 76] and where disordered to periodic phase transitions were probed dynamically, in an attempt to answer a question set 40 years ago on the nature of the incommensurate-commensurate phase transitions [77] and which will occupy us throughout Chapter 4.

More recently, similar experiments have been carried out on 2D Rydberg atom arrangements where the same model is realized [78, 79], with observations of “antiferromagnetic” phases.

1.3 Thesis overview We present two main topics: ground state level crossings in Ising-ordered phases (Chapters 2 and 3) and quantum phase transitions between ordered phases and phases where correlations are incommensurate with respect to the lattice of sites (Chapter 4).

The next two chapters follow their respective published manuscripts almost completely, so a preface to this work is given here which will recount how these advances came to be. The last chapter has been appropriately adapted with respect to the published manuscript and so no further introduction was deemed necessary.

1.3.1 Ground state level crossings in TFI-like chains The first main topic of this thesis is motivated by STM experiments on Ising chains of cobalt adatoms constructed atom by atom [42]. By building the chain atom by atom, the progression towards the infinite-system spectrum can be probed, which for TFI-like systems one can already observe with relatively few atoms due to the exponentially decreasing gap between the two lowest energy states. However, it was also observed that for particular values of the applied external magnetic field, exact degeneracies between these two states occurred at finite size, and the number of degeneracies (or crossings of the two states) in the full interval of the applied magnetic field from minus infinity to infinity is equal to the number of adatoms.

This led to a more careful analytical and numerical study of the degeneracies [80], where the most successful explanation for these crossings came from the mapping to the Kitaev model [32] which can be written in terms of coupled pairs of Majorana fermions. The wavefunction of the edge Majoranas shows phase oscillations along the chain on a particular region of the SPT phase of the model. When these oscillations become commensurate with the lattice, the pair of edge Majoranas are exactly decoupled, leading to a regular zero energy fermion.

A subsequent study followed on the implications of the degeneracies re-

garding the autocorrelation time of spins [1], which is presented in this thesis in Chapter 2. This was motivated by a recent theoretical result that non-integrable extensions of the TFI model still preserve some sort of edge operator referred to as “strong zero modes” [81] which are connected adiabatically in some limit to the edge Majoranas. The implications on the autocorrelation time are strongest for the edge spins because both edge Majoranas and the strong zero modes reduce, in lowest-order, to single edge Pauli matrices.

The Majorana interpretation of the level crossings suggests that both boundary conditions and dimensionality could play an important role in this phenomena, since the mapping from TFI to Majorana fermions is only effective for open boundaries and in one-dimension, as we discussed before. However, simple numerical calculations in small systems immediately tell us otherwise: both periodic chains (rings) or small 2D and 3D clusters of spins governed by the same models show again the same number of crossings when we sweep the full range of the applied magnetic field.

Thanks to the input and ideas of our collaborator Markus Müller, the topic of the ground state level crossings was revisited but in the context of high-order degenerate perturbation theory (DPT) [2], which made clear the independence of this phenomena from the chosen geometry. The energy splitting between the two ground states of Ising-like models can be calculated in DPT from the matrix element of an effective Hamiltonian between the two Ising ground states, one state becoming the other by flipping all spins. The resulting infinite sum is interpretable as a sum over infinitely many tunneling paths between the Ising ground states where on each tunneling step one or two spins are flipped, as we shall demonstrate in Chapter 3.

Studying the level crossings with perturbation theory had already been attempted [80], but here the TFI Hamiltonian was considered as the unperturbed Hamiltonian, and the resulting perturbative series quickly becomes intractable after just a few iterations. By considering instead the Ising Hamiltonian as the unperturbed basis and then reorganizing the terms in the series by the total number of spin flip operations which acted on one of the ground states, meaning that all terms of “rescaled order” lower than the length of the chain are zero, we can calculate the lowest rescaled order term of the series through simple recursion relations, and we see that this term predicts a number of crossings equal to the length chain and thus contains in it all the relevant physics to understand the crossings.

Later, it came to our attention that the problem of tunneling of spin magnetization had already been tackled in the field of molecular magnets [82, Review]. The total spins of some of the atoms of these molecules couple to-

gether with almost-isotropic Heisenberg exchange interactions and can realize ground states of large spin- S . Slight molecular anisotropy causes the ground state S multiplet to split, thus the low-energy spectrum of these magnets is described by a single anisotropic spin- S . One again finds ground state level crossings in such a model for some values of the external magnetic field, the number of which is equal to $2S$, which was also demonstrated experimentally [83]. Naturally, the largest spin- S one can form given N spin- $1/2$ s is $S = N/2$, thus the connection between the crossings in both systems is obvious. We revisited this model and applied our recursive tunneling calculation, in this case the tunneling being between the $-S$ and $+S$ states, the result being a simpler and arguably more intuitive explanation of the crossings than what previous analytical work offered [84].

Chapter 2

Infinite coherence time of edge spins in finite-length chains

The work in this chapter was done in collaboration with my supervisor Frédéric Mila and it was published in 2018 [1]. This chapter follows the published work exactly except for minor corrections, a change in notation, and the addition of an appendix on the determination of the zero modes of the Kitaev model.

2.1 Introduction In recent experiments on chains of cobalt adatoms [42], level crossings of the two lowest energy states have been observed as a function of the external magnetic field h . An analysis of the effective spin model of that system, the spin-1/2 XY chain with in-plane magnetic field, has revealed the presence of N level crossings as a function of the magnetic field h between the two lowest energy states [85, 80]. In Ref. [80], it was shown in particular that the model can be approximately mapped through a self-consistent mean-field method to a well-known fermionic non-interacting model, the Kitaev chain [32], which can in turn be described as a system of Majorana fermions coupled in pairs. This model has a topologically non-trivial phase when the chemical potential lies inside the free-fermion band. In this phase, two Majorana fermions located at opposite edges have an exponentially small coupling. For N values of the magnetic field (inside the topological phase), this coupling vanishes. The two edge Majoranas can then be combined to form a zero energy regular fermion, implying that all many-particle states are degenerate. This explains in particular the ground state crossings in the spin model [80]. In topological superconducting systems, uncoupled edge Majoranas are commonly referred to as Majorana zero modes [86]. After a Jordan-Wigner transformation the Kitaev chain becomes the XY chain with transverse field. This model has been extensively studied and its spin correlation functions [87, 88, 89, 90] and free energy [91] were calculated a long time ago, but the fact that there are zero modes at non-zero values of the field has only been noted recently. In the spin model the topological phase translates exactly to an ordered phase which is either ferro or antiferromagnetic

depending on the spin couplings. This phase is realized at small transverse fields, below the Ising quantum critical point.

In another recent work [81], it was shown that "strong zero modes" associated to an ordered phase of integrable models such as the transverse field Ising (TFI) model [29] or the anisotropic Heisenberg XYZ model lead to a high coherence of the edge spin for long times, even for infinite temperature. The strong zero modes are operators localized at the edges of the chain that guarantee a quasi-degeneracy of all eigenstates, with a splitting that becomes exponentially small upon increasing the system size, leading to an infinite coherence time in the thermodynamic limit. A strong zero mode is still a Majorana zero mode in the sense of [86], but the definition of strong zero mode stresses the existence of a \mathbb{Z}_2 symmetry which anti-commutes with the mode operator. The strong zero mode of TFI is exactly the Majorana edge quasi-particle that is decoupled from the Hamiltonian in the thermodynamic limit. When considering a perturbation that breaks the integrability of TFI, a strong zero mode could no longer be obtained, but applying the iterative method used to obtain the XYZ strong zero mode to this model resulted in an "almost strong zero mode", whose existence implies a plateau of coherence for long albeit always finite times that was observed numerically [81]. One of the perturbation terms considered was precisely a spin-spin coupling along the field, resulting in the XY chain with in-plane magnetic field.

In this chapter, we concentrate on the topological phase of the model, and we explore the following idea: since degeneracies due to strong zero modes lead to a high coherence of edge spins that is maintained forever in the thermodynamic limit because the degeneracies become exact in that limit, then we can expect to get the same result if there are exact degeneracies for finite sizes, like in the XY model with in-plane or transverse field.

The chapter is organized as follows: in Sec. 2.2, we introduce the two models we focus on, we review the exact solution of the non-interacting model and the relevant edge operators of both models, and we investigate the evolution of the level crossings as we interpolate from one model to the other. In Sec.2.3, we show how the edge spin time correlation can be approximated by a single exponential (or cosine) in the ordered phase for any eigenstate, and we explore the consequences of the degeneracies for both models. We point out that the zero modes only have significant consequences for the edge spin, and we illustrate the difference numerically by comparing the correlation of edge and bulk spins. We also compare the spin time correlation of the two models for infinite temperature, where significant differences show up because the models differ by an interaction term in the fermionic language that

destroys integrability.

2.2 Models Let us start by introducing the anisotropic spin-1/2 Heisenberg chain with open boundary conditions and a magnetic field h along z :

$$\mathcal{H} = \sum_{i=1}^{N-1} (J_x \sigma_i^x \sigma_{i+1}^x + J_y \sigma_i^y \sigma_{i+1}^y + J_z \sigma_i^z \sigma_{i+1}^z) - h \sum_{i=1}^N \sigma_i^z, \quad (2.1)$$

where $\sigma^{a=x,y,z}$ are the Pauli matrices. We denote this model as XYZ-Z, with the convention that the letters before the hyphen indicate the non-zero components of the J couplings, while the letter after the hyphen (if any) refers to the direction of the magnetic field if there is one. In what follows, we mostly focus on two limits of this model: XZ-Z and XY-Z, which are equivalent to an XY chain with in plane or out of plane magnetic field. Fixing the field direction and changing the couplings will prove to be more convenient when comparing the crossings of both models.

All the terms of the Hamiltonian either flip two adjacent spins or none when applied to a state with spins quantized along z , implying that there are no couplings between states of different z spin parity. This can be quantified by the operator $P = \prod_{i=1}^N \sigma_i^z$ with eigenvalues ± 1 and $[H, P] = 0$. Both models, XY-Z and XZ-Z, have an ordered phase in which the ground state is two-fold degenerate in the thermodynamic limit. For XY-Z, this phase is defined by $|h| \leq |J_x + J_y|$. For XZ-Z, $|h| \lesssim |J_x + J_z|$ is a good approximation for large J_z , while $|h| \lesssim |J_x + \frac{3}{2} J_z|$ is more accurate for small J_z [92]. For finite size, there is an energy splitting between the two lowest energy states, which belong to different P parity sectors. This splitting is exponentially small with the size of the system.

2.2.1 XY-Z Majorana edge fermions We review here the exact solution of XY-Z. After a Jordan-Wigner transformation into Majorana fermions and a subsequent orthogonal transformation [32, 80],

$$\gamma_i^a = \sigma_i^a \prod_{j=1}^{i-1} \sigma_j^z, \quad \sigma_i^z = i \gamma_i^x \gamma_i^y, \quad \tilde{\gamma}_i^a = \sum_j Q_{ij}^a \gamma_j^a, \quad (2.2)$$

where $Q^{a=x,y}$ are orthogonal matrices, and $\gamma^a, \tilde{\gamma}^a$ obey

$$\{\gamma_i^a, \gamma_j^b\} = 2\delta_{ab}\delta_{ij}, \quad \gamma_i^a = (\gamma_i^a)^\dagger, \quad (\gamma_i^a)^2 = 1, \quad (2.3)$$

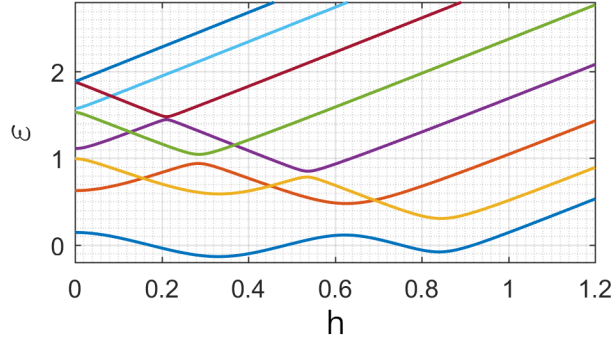


Figure 2.1: Spectrum of the quasi-particle energies ε_i (Eq. 2.4) of XY-Z, for $J_x = 0.6$, $J_y = 0.4$, and $N = 8$. The model is topologically non-trivial when $|h| \leq |J_x + J_y| = 1$. Four $\varepsilon = 0$ points are observable inside this phase and there are four more at negative h , symmetric to those shown here.

the XY-Z model becomes a model of Majorana fermions coupled in pairs, or, equivalently, a system of free fermions with particle-hole symmetry:

$$H = \frac{i}{2} \sum_{i=0}^{N-1} \varepsilon_i \tilde{\gamma}_i^x \tilde{\gamma}_i^y = \frac{1}{2} \sum_{i=0}^{N-1} \varepsilon_i (\mu_i^\dagger \mu_i - \mu_i \mu_i^\dagger), \quad (2.4)$$

where $\mu_i^\dagger = (\tilde{\gamma}_i^x - i\tilde{\gamma}_i^y)/2$ obeys the usual fermionic commutation relations. An ε -spectrum for a finite system is illustrated in Fig. 2.1. We observe in particular that there are $\varepsilon = 0$ solutions at the fields

$$h_n = 2\sqrt{J_x J_y} \cos\left(\frac{n\pi}{N+1}\right), \quad (2.5)$$

with $n = 1, 2, \dots, N$. Note that these points only exist if $J_x J_y > 0$. The Majorana operators $\tilde{\gamma}_i^a$ corresponding to $\varepsilon \approx 0$, which we denote as $\tilde{\gamma}^a$ with energy ε_0 , are

$$\tilde{\gamma}^a \approx \frac{\mathcal{N}}{\lambda_+^a - \lambda_-^a} \sum_{n=1}^N ((\lambda_+^a)^n - (\lambda_-^a)^n) \gamma_n^a, \quad (2.6)$$

$$\lambda_\pm^a = \frac{h \pm \sqrt{h^2 - 4J_x J_y}}{2J_a}, \quad (2.7)$$

with $a = x, y$. They are exact when the energy is exactly zero (as shown in Appendix 2.A), so at the points given by (2.5). The operators $\tilde{\gamma}^x$ and $\tilde{\gamma}^y$ are localized at the edges of the system, and one is the reflection of the other with respect to the middle of the chain. When $|J_x| > |J_y|$ (resp. $|J_y| > |J_x|$)

, $\tilde{\gamma}^x$ (resp. $\tilde{\gamma}^y$) is localized at the first site. While we have two uncoupled Majorana fermions at the h_n points, that only means we have one zero energy fermion, resulting in the 2-fold degeneracy of all eigenstates. The Majorana edge fermions of the Ising chain (X) and TFI (X-Z) can be obtained from (2.7) using appropriate limits.

In the fermionic language the ordered phase corresponds to a topologically non-trivial phase where the $\tilde{\gamma}^a$ are uncoupled in the thermodynamic limit. Equation (2.5) guarantees this in the region $h^2 < 4J_x J_y$, but the full ordered phase goes beyond that. $\tilde{\gamma}^x$ is a solution in the thermodynamic limit as long as $(\tilde{\gamma}^x)^2 = 1$ for some \mathcal{N} . Using this condition to calculate \mathcal{N}^2 for $N \rightarrow \infty$ we obtained

$$\mathcal{N}^2 = \frac{(J_x - J_y)(-h + J_x + J_y)(h + J_x + J_y)}{J_x^2(J_x + J_y)} \quad (2.8)$$

$$= 1 - \left(\frac{h}{J_x}\right)^2 - \left(\frac{J_y}{J_x}\right)^2 + O\left(\frac{1}{J_x^3}\right). \quad (2.9)$$

The critical lines of the x-ordered phase can be deduced from the condition $\mathcal{N}^2 = 0$. They are given by $|h| = |J_x + J_y|$, corresponding to the order-disorder (topological-trivial) transition, and $J_x = J_y$, the transition into the gapless XY phase. Beyond this line ($J_x < J_y$) the norm of $\tilde{\gamma}^x$ diverges and the well-defined edge Majorana is $\tilde{\gamma}^y$. The phase diagram was first obtained from the spin-spin correlations in Ref. [88]. For a recent review of the model see Ref. [93].

Denoting by $|E\rangle$ an eigenstate of energy E , we have

$$\tilde{\gamma}^x |E\rangle = (\mu^\dagger + \mu) |E\rangle = |E'\rangle, \quad |E\rangle = \tilde{\gamma}^x |E'\rangle, \quad (2.10)$$

where $|E'\rangle$ is the eigenstate of energy $E' = E \pm \varepsilon_0$ differing from $|E\rangle$ by a quasi-particle. Each term of $\tilde{\gamma}^x$ flips one spin when the quantization axis is along z , so the P parity is changed. Separating the eigenstates in parity sectors, we can write

$$\tilde{\gamma}^x |E_n^\pm\rangle = |E_n^\mp\rangle, \quad (2.11)$$

where $|E_n^\pm\rangle$ is an eigenstate with $P |E_n^\pm\rangle = \pm |E_n^\pm\rangle$.

2.2.2 XZ-Z prethermal strong zero mode The J_z term of XZ-Z becomes a four fermion term after the Jordan-Wigner transformation in Eq.2.2, so we no longer have a free fermion solution. In fact, the model is non-integrable, an important piece of information since integrability is believed to be a condition for the existence of a "strong zero mode"[94]. A strong zero mode (Ψ) is an operator that squares to 1, obeys $[H, \Psi] \sim e^{-|\alpha|N}$ and changes the P parity of a

state of well-defined parity. For the XY-Z model, the operator $\tilde{\gamma}^x$ with $N \rightarrow \infty$ matches exactly this definition. In the thermodynamic limit, a strong zero mode commutes with the Hamiltonian but changes the parity of the state. So each level must contain a state of each symmetry, and the spectrum of both sectors are identical. This is the case of XYZ, which has a strong zero mode inside the ordered phase [94].

The XZ-Z model does not have a strong zero mode, but it has an "almost strong zero mode"[81], later understood as a "prethermal strong zero mode"[95], implying the emergence of a conserved quantity for a quasi exponential time [96, 97]. Such an operator, which we denote as Φ , has the same properties as a strong zero mode except that the commutator is always finite: $[H, \Phi] = \nu$, where ν is an operator whose norm decreases exponentially with the size up to some limiting system size where a minimum is reached. Using this commutator we have

$$(H\Phi - \nu) |E_n^\pm\rangle = E_n^\pm \Phi |E_n^\pm\rangle \quad (2.12)$$

for an eigenstate $|E_n^\pm\rangle$. Assuming that the norm of ν is sufficiently small, we may write

$$\Phi |E_n^\pm\rangle \approx |E_n^\mp\rangle, \quad (2.13)$$

with $E_n^\pm - E_n^\mp \sim \|\nu\|$. In the limit $J_z = 0$, Φ would become the X-Z edge Majorana fermion $\tilde{\gamma}^x$ and we would recover Eq. 2.11. The operators Φ and $\tilde{\gamma}^x$ have an important similarity in that their leading operator is the same:

$$\tilde{\gamma}^x = \mathcal{N}\sigma_1^x + \dots, \quad \Phi = \mathcal{M}\sigma_1^x + \dots, \quad (2.14)$$

$$\mathcal{M}^2 = 1 - \left(\frac{h}{J_x}\right)^2 - \left(\frac{J_z}{J_x}\right)^2 + O\left(\frac{1}{J_x^3}\right). \quad (2.15)$$

The second order expansions of their normalization constants \mathcal{N} and \mathcal{M} are also identical. In the limit of the Ising model ($J_y = J_z = h = 0$) both operators become equal to $\sigma_1^x = \gamma_1^x$, which is exactly the uncoupled edge Majorana fermion of that model. As we will see, the existence of the operators $\tilde{\gamma}^x$ and Φ together with the level crossings are the factors that allow a high coherence of the edge spins for an infinite time for both models.

2.2.3 Level crossings The addition of a J coupling to X-Z, be it J_y or J_z , creates oscillations in the energies as a function of h inside the ordered phase, which causes crossings between pairs of quasi-degenerate states of different parity, a behaviour not present in the TFI. In particular, both models have N

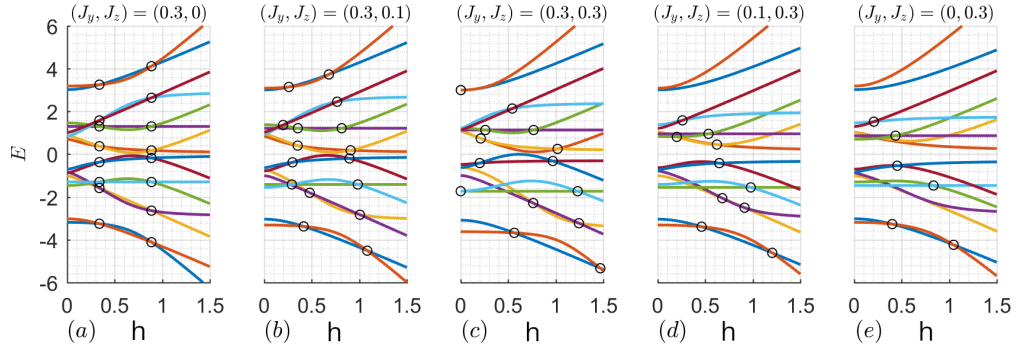


Figure 2.2: Spectrum of XYZ-Z for $N = 4$, $J_x = 1$, and several values of (J_y, J_z) with XY-Z on the left and XZ-Z on the right. The level crossings associated to zero modes are highlighted with circles. The non-interacting nature of XY-Z of panel (a) is noticeable: the level crossings of different pairs of states occur all at the same fields. This is no longer true when the model is not integrable, as in panels (b) to (e).

points of exact ground state degeneracy as a function of h in some parameter region. The ground state crossings of XZ-Z have already been studied in detail [80]: when $|J_x| > |J_z|$, the two lowest energy states form a low energy sector isolated from the rest, and if $J_z > 0$, there are N crossings between these two states, while there are no crossings for $J_z < 0$. However, the spectrum of XZ-Z is independent of the sign of J_x and h , so the spectrum of $-H(J_z)$ is the same as $H(-J_z)$, implying that for $J_z < 0$ the crossings are present in the highest energy state.

Depending on which J coupling is the largest and on its sign, we have different ordered phases. We study the phase $|J_x| > |J_{y,z}|$ where there is order in x . The signs of the couplings are not very important for the correlation, but we want crossings to exist in the ground state. So, from now on we restrict ourselves to $J_x > J_{y,z} > 0$. Also, the physical situations of positive or negative field h are equivalent by rotation, so we only discuss $h > 0$.

In Fig. 2.2 we show how the crossings in each model are adiabatically related to each other: starting from the XY-Z model (Fig. 2.2(a)), where the non-interacting nature is noticeable and where all energies are degenerate at h_n , and adding a coupling in the z direction that obeys $J_x > J_z > 0$, the ground state crossings continuously move towards higher h . Then when decreasing $J_y \rightarrow 0$ they become the N crossings of XZ-Z (Fig. 2.2(e)). The middle spectrum (Fig. 2.2(c)) corresponds to $J_y = J_z$, which is a turning point where some of the crossings disappear if we start from XY-Z and increase J_z . In particular,

both crossings of the highest energy pair meet at $h = 0$, after which a gap appears between these states. When J_y finally becomes zero, a second set of crossings vanishes. The energy pairing in XZ-Z is highly asymmetrical: lower energy pairs have a small gap up to fields much higher than their high energy counterparts. Note that the roles would be reversed for negative J_z . Changing the sign of J_z would invert the spectra in energy, and the ground state of XZ-Z would have no crossing. The three middle plots in Fig. 2.2 show that the XYZ-Z model also has energy crossings in some parameter region, implying that some of our results could be extended to the more general case.

2.3 Edge spin time correlation This section is devoted to analytical and numerical results regarding the auto-correlation of edge spins. Following Ref. [81], we consider the edge spin time auto-correlation of an eigenstate $|E_n^\pm\rangle$ of energy E_n^\pm and P parity ± 1 defined by

$$A_n^\pm(t) \equiv \langle E_n^\pm | \sigma_1^x(t) \sigma_1^x(0) | E_n^\pm \rangle \quad (2.16)$$

where the component of the spin is that along which the system is ordered. We introduce $I = \sum_m |E_m^+\rangle \langle E_m^+| + |E_m^-\rangle \langle E_m^-|$ to obtain

$$\begin{aligned} A_n^\pm(t) &= \langle E_n^\pm | e^{-iHt} \sigma_1^x e^{iHt} I \sigma_1^x | E_n^\pm \rangle \\ &= \sum_m |\langle E_m^\mp | \sigma_1^x | E_n^\pm \rangle|^2 e^{i(E_m^\mp - E_n^\pm)t}. \end{aligned} \quad (2.17)$$

In this form it becomes obvious that any degeneracy creates time-independent positive terms in the correlation, as long as the appropriate matrix element is non-zero. However, not only is the matrix element between the states with crossings circled in Fig. 2.2 non-zero, but we found that it dominates over all other matrix elements while inside the bulk of the ordered phases, implying that we have both degeneracies and a high value of coherence.

Coherence can still be present when considering higher temperatures [81]. The limit of lowest coherence should be at infinite temperature, where the average edge spin correlation will be

$$\bar{A}(t) \equiv \langle \sigma_1^x(t) \sigma_1^x \rangle_{T=\infty} = \frac{1}{2N} \sum_n [A_n^+(t) + A_n^-(t)]. \quad (2.18)$$

2.3.1 XY-Z correlation The correlation of XY-Z can be determined exactly since σ_1^x is exactly the local Majorana fermion γ_1^x , which, inverting the last

equation of (2.2), is given by

$$\sigma_1^x = \gamma_1^x = \sum_k Q_{k1}^x \tilde{\gamma}_k^x, \quad (2.19)$$

where we sum over the N Majorana fermions, one of them being the edge Majorana $\tilde{\gamma}^x$. Substituting in (2.17), we get

$$\begin{aligned} A_n^\pm(t) &= \sum_m |\langle E_m^\mp | \sum_k Q_{k1}^x \tilde{\gamma}_k^x | E_n^\pm \rangle|^2 e^{i(E_m^\mp - E_n^\pm)t} = \\ &= \sum_k |Q_{k1}^x|^2 e^{i g_{nk}^\pm \epsilon_k t} \end{aligned} \quad (2.20)$$

where $g_{nk}^\pm \equiv -i \langle E_n^\pm | \tilde{\gamma}_k^x \tilde{\gamma}_k^y | E_n^\pm \rangle$ is equal to -1 or 1 depending on whether the fermion μ_k^\dagger is present in the state or not. The correlation of any state consists of the same N terms with different signs in the exponentials. By symmetry, the result must be the same at the other edge of the chain. Note that we cannot write the same decomposition for the correlation of spins in the bulk since only σ_1^x corresponds directly to one of the local Majorana fermions in the Jordan-Wigner transformation. So we expect a difference between edge and bulk spins.

In the disordered phase, there is no Majorana fermion that is localized at the edge, so all terms are of the same order of magnitude but differ in amplitude and frequency. Accordingly, the system quickly becomes decoherent (Fig. 2.3(a)). In the thermodynamic limit, assuming that all modes have the same amplitude at the edge spin and considering the ground state correlation in which $g_{nk}^\pm = 1$ for all k , we have

$$A_{GS}(t) \approx \frac{1}{\epsilon_t - \epsilon_b} \int_{\epsilon_b}^{\epsilon_t} e^{i\epsilon t} d\epsilon = -\frac{i}{t} \frac{e^{i\epsilon_t t} - e^{i\epsilon_b t}}{\epsilon_t - \epsilon_b}, \quad (2.21)$$

where ϵ_t and ϵ_b are the limits of the band, leading to $A_{GS}(\infty) = 0$. We expect the same result for all states. In the ordered phase, the edge mode term stands out in amplitude and frequency. Writing explicitly the $\tilde{\gamma}^x$ term we have

$$A_n^\pm(t) = \mathcal{N}^2 e^{i g_{n0}^\pm \epsilon_0 t} + z(t), \quad (2.22)$$

where $|z(t)| \leq (1 - \mathcal{N}^2)$ and $z(t)$ is the bulk contribution to the correlation which, as we saw in (2.21), disappears for infinite N and t , so that $A_n^\pm(\infty) = \mathcal{N}^2$ in the thermodynamic limit. For finite sizes, ϵ_0 can be orders of magnitude lower than the other energies, so the term $z(t)$ looks like noise on the

time-scale of $1/\varepsilon_0$ (Fig. 2.3(b)), even though it is well-defined. We can thus approximate

$$A_n^\pm(t) \approx \mathcal{N}^2 e^{ig_{n0}^\pm \varepsilon_0 t}. \quad (2.23)$$

So the edge spin flips after an interval of time $\tau = \pi/\varepsilon_0$, independently of the eigenstate the system is in. Close to the h_n points of Eq. (2.5), ε_0 is approximately linear with $\Delta h_n = h - h_n$, so $\tau \sim 1/\Delta h_n$. Since ε_0 is exponentially suppressed with system size, we have $\tau \sim e^{|\alpha|N}/\Delta h_n$, allowing for a better fine-tuning of the coherence time for larger sizes. Exactly at h_n we have $A_n^\pm(t) \approx \mathcal{N}^2$, so the edge spin remains coherent for an infinite time (Fig. 2.3(c)). Even for infinite temperature, we have

$$\bar{A}(t) = \text{Re}(A_n^\pm(t)) \approx \mathcal{N}^2 \cos(\varepsilon_0 t). \quad (2.24)$$

so the same discussion applies in this limit. However, this result is very sensitive to any realistic perturbation. For example, adding a very small J_z coupling does not alter significantly \mathcal{N}^2 , but each pair of states will have a slightly different energy difference and the crossings will move away from h_n as we saw in Fig. 2.2 so that at some point we must reach decoherence, and an infinitely-lived plateau is no longer present at the h_n points (Fig. 2.3(d)). However, if we were to change the field slightly to a value where one of the crossings moved to, then we would recover a (small) positive constant term in the correlation and the coherence time would be infinite again. We explore this fact in more detail in the next section.

2.3.2 XZ-Z correlation We cannot obtain any exact result for the XZ-Z correlation, but as we saw in Sec. 2.2.2 there is an operator that gives us a pairing between states of different parity of the form $\Phi |E_n^\pm\rangle \approx |E_n^\mp\rangle$. Using this with the properties of σ_1^x , we have

$$\begin{aligned} \langle E_n^\mp | \Phi \sigma_1^x | E_n^\mp \rangle &\approx \langle E_n^\pm | \sigma_1^x | E_n^\mp \rangle \approx \langle E_n^\pm | \sigma_1^x \Phi | E_n^\pm \rangle \Rightarrow \\ \langle E_n^\pm | \sigma_1^x | E_n^\mp \rangle &\approx \frac{1}{2} \langle E_n^\pm | \{ \sigma_1^x, \Phi \} | E_n^\pm \rangle. \end{aligned} \quad (2.25)$$

If $J_z = 0$, the expression would have no error term, Φ would become $\tilde{\gamma}^x$, and the anti-commutator would be a constant: $\{ \sigma_1^x, \tilde{\gamma}^x \} = 2\mathcal{N}$. Using the next-order terms of Φ determined in [81], we find $\{ \sigma_1^x, \Phi \} = 2\mathcal{M} + \hat{O}(J_z^2/J_x^2)$, and substituting in Eq. 2.25 we have

$$\langle E_n^\pm | \sigma_1^x | E_n^\mp \rangle = \mathcal{M} + O\left(\frac{J_z^2}{J_x^2}\right) \quad (2.26)$$

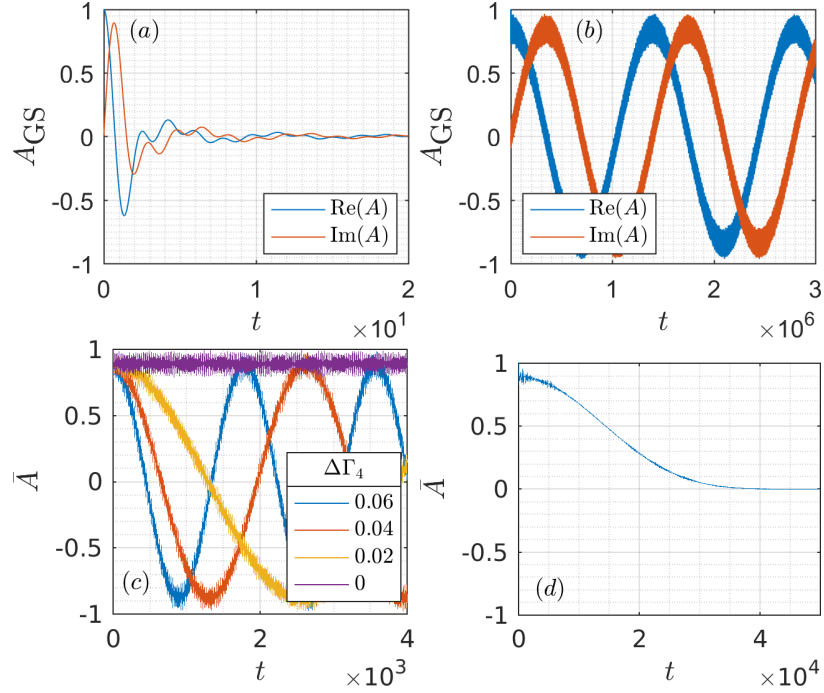


Figure 2.3: (a,b) Ground state edge spin correlation of XY-Z for $N = 20$, $J_x = 1$, $J_y = 0.3$: (a) Disordered phase ($h = 2.2$). The correlation function decays very fast; (b) In the ordered phase, away from a level crossing ($h = 0.35$). The correlation function oscillates with period $\tau = \pi/\epsilon_0$, where ϵ_0 is the splitting between the quasi-degenerate ground states. The noise-like component is due to the bulk. (c,d) Average (infinite temperature) edge spin correlation for $N = 8$, $J_x = 1$, $J_y = 0.3$: (c) Close to a level crossing ($h_4 \approx 0.19$). At the level crossing, indefinite coherence is achieved. (d) Close to a level crossing of XY-Z ($h_4 \approx 0.19$), but with an extra coupling $J_z = 0.001$. The coherence is lost after a time inversely proportional to J_z .

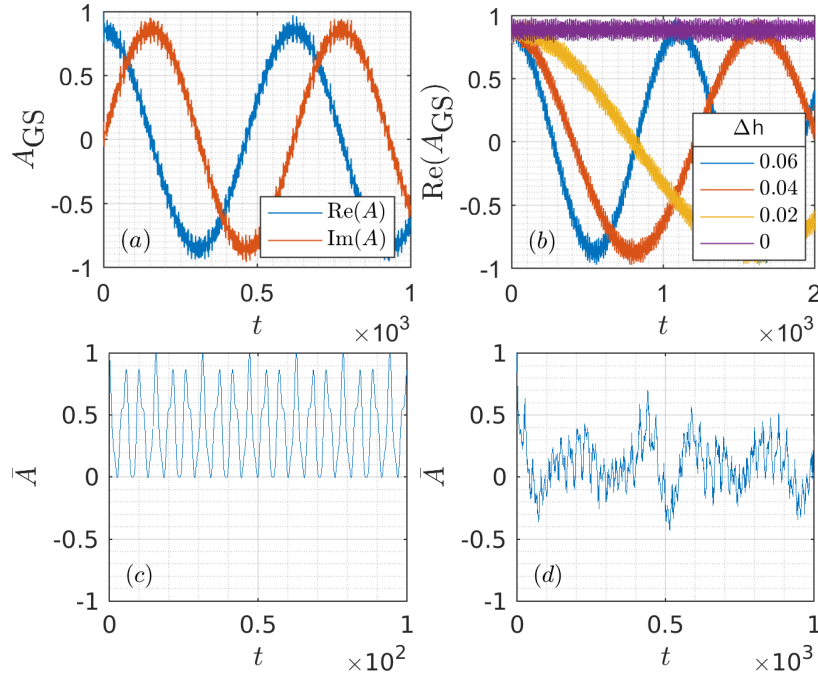


Figure 2.4: (a),(b) Ground state edge spin correlation of XZ-Z for $N = 8$, $J_x = 1$, $J_z = 0.3$ (a) in the ordered phase ($h = 0.35$), (b) approaching the first ground state crossing at $h \approx 0.2341$. Although the XZ-Z model is not integrable, the situation is very similar to that of the XY-Z model (Figs. 3(b,c)). (c,d) Average (infinite temperature) edge spin time correlation at ground state crossings, with $J_x = 1$, $J_z = 0.3$ and (c) $N = 2$, $h \approx 0.62$, (d) $N = 4$, $h \approx 0.4$. The constant part of the correlation corresponds to the time-average of these curves. It is much smaller than in the XY-Z case because the crossings do not occur at the same fields for all pairs, and it decreases fast when the system size increases.

In the ordered phase, the correlation can be approximated by its main term:

$$\begin{aligned} A_n^\pm(t) &\approx |\langle E_n^\mp | \sigma_1^x | E_n^\pm \rangle|^2 e^{i(E_n^\mp - E_n^\pm)t} \\ &\approx \mathcal{M}^2 e^{i(E_n^\mp - E_n^\pm)t}, \end{aligned} \quad (2.27)$$

where in the first equation we ignore all other terms and in the second equation we use Eq. (2.26). As seen in Fig. 2.4(a), this result is confirmed numerically. For finite sizes, we have $A_n^\pm(t) \approx \mathcal{M}^2$ when the paired states are degenerate, which happens N times for the ground state (Fig. 2.4(b)). The discussion regarding the XY-Z coherence time close to the degeneracy points is also applicable here. However, by contrast with XY-Z, the time-independent term of the average correlation can be quite small since the crossings of different pairs do not happen for the same field. At a pair crossing we have

$$\bar{A}(t) \approx \mathcal{M}^2/2^{N-1} + f(t), \quad (2.28)$$

for some real function $|f(t)| \leq 1 - \mathcal{M}^2/2^{N-1}$ whose time average is approximately zero. The constant term may not be noticeable due to the noise $f(t)$. The constant term could be doubled or, although very unlikely, tripled, if for certain J couplings there are coincident crossings. In Figs. 2.4(c) and 2.4(d) we show \bar{A} at the ground state crossings of very small chains. The time average in both cases gives approximately the expected constant term, but it is clear that the constant term will be harder to detect under the noise as we increase the chain size.

2.3.3 Edge vs. bulk The fact that the main term of the $\tilde{\gamma}^x$ and Φ operators is σ_1^x has important consequences for the edge spin, but that is the only term which is a single Pauli matrix, all others being products of Pauli matrices. So we cannot conclude anything about the bulk correlation from them. To highlight the difference between edge and bulk spins, we show in Figs. 2.5 (XY-Z) and 2.6 (XZ-Z) the correlation along the spin chain at a crossing point of the ground state and of a pair of excited states. While the ground state correlation is even higher and consequently has less noise in the bulk, this behavior is mainly lost in the excited states, but some state pairing is still manifest. For example, on the second spin of the XY-Z chain, the plateau visible for the first excited state (index $n = 2$) pair implies that the term $|\langle E_2^+ | \sigma_2^x | E_2^- \rangle|^2 \approx 0.5$ dominates over the rest. The third spin has no plateau, but the σ_3^x elements reveal a pairing in $|\langle E_4^\pm | \sigma_3^x | E_2^\mp \rangle|^2 \approx 0.9$, resulting in a correlation that can be approximated by $0.9e^{i(E_4^\pm - E_2^\mp)t}$.

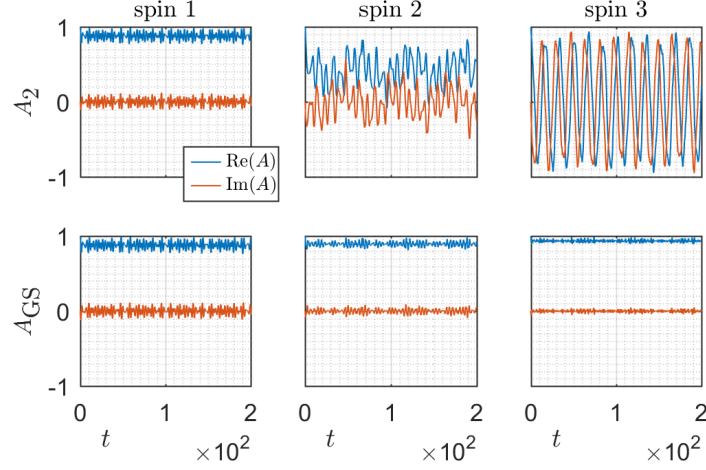


Figure 2.5: Spin time correlation of the first 3 spins ($N = 6$) for the first (A_{GS}) and second (A_2) lowest-energy pair of states of XY-Z, with $J_x = 1$, $J_y = 0.3$, at the first crossing ($h \approx 0.244$). High coherence is maintained away from the edge for the lowest pair (bottom panels), but it is only maintained at the edge for the second pair and disappears fast away from it (top panels).

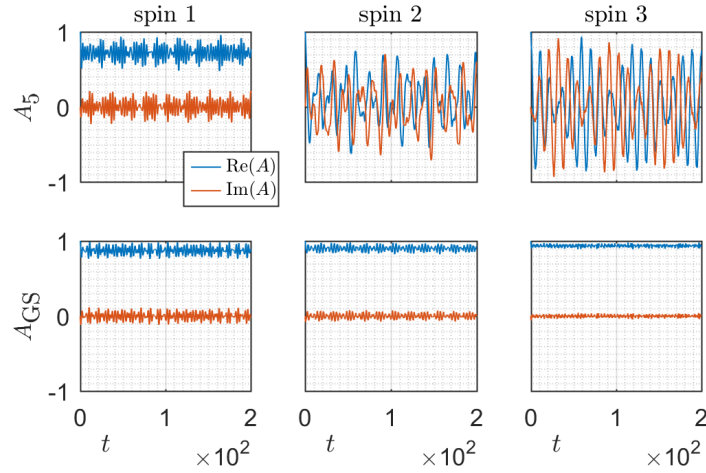


Figure 2.6: Spin time correlation of the first 3 spins ($N = 6$) for the first (A_{GS}) and fifth (A_5) lowest-energy pair of states of XZ-Z, with $J_x = 1$, $J_z = 0.3$, at their respective first crossings ($h_{\text{ground}} \approx 0.295$, $h_{\text{excited}} \approx 0.376$). The situation is the same as for the integrable XY-Z case of Fig. (5), although the crossings occur at different fields.

The fact that the coherence is maintained at all sites in the ground state is easy to understand in the limit of the slightly perturbed Ising model (i.e. small J_y and h). In that limit, the two quasi-degenerate ground states are given by

$$|E_1^\pm\rangle \sim \frac{1 \pm P}{\sqrt{2}} |\rightarrow\leftarrow\rightarrow\leftarrow\rightarrow\leftarrow\leftarrow\rangle_x, \quad (2.29)$$

where the spins are along the x direction. Calculating the matrix elements explicitly from here, and noting that $\{\sigma_n^x, P\} = 0$, we have $|\langle E_1^+ | \sigma_n^x | E_1^- \rangle|^2 \sim 1$, from which the ground state coherence of all spins follows. It would be interesting to see to which extent the observations for the excited states can be rationalized along similar lines. This goes beyond the scope of the present paper however and is left for future investigation.

2.4 Summary and discussion In both the XY-Z and the XZ-Z models, the edge spin time correlation of any eigenstate can be simplified to a single exponential in the ordered phase due to Majorana-like operators localized at the edges that commute or almost commute with the Hamiltonian. At the crossing points of two paired states the edge spin state is partially conserved: its time autocorrelation does not decay to zero but goes to a finite value (generically smaller than 1) in the limit of infinite time. Close to the crossing point the edge spin seems to be rotating with a period that is proportional to $1/\Delta h$. This could prove of experimental relevance since the edge spin can be controlled by an external magnetic field.

While all the spins of the chain show coherence at the crossings in the ground state, the edge spins are different in that they are coherent in any excited state. As a consequence, the coherence remains relatively unaltered for XY-Z at high temperatures, although the system becomes more sensitive to perturbations the higher the temperature. For XZ-Z, coherence can be maintained at a plateau of value \mathcal{M}^2 for long times as found in [81], after which it decays to $n\mathcal{M}^2/2^{N-1}$ if there are n degenerate pairs for the current field. Thus for any temperature there has to be a plateau between \mathcal{M}^2 and $\mathcal{M}^2/2^{N-1}$.

2.A The Kitaev model As we have discussed, the XY-Z limit of model (2.1) preserves the free fermion nature. Following the calculation done in Ref. [80], we review here a simple way to determine in the fermionic language the zero mode solutions of the model, which are central for all the discussion of this chapter. We map the spins to Majorana fermions $\gamma^{a=x,y}$ through the Jordan-Wigner transformation in Eq. (2.2). The chain product of σ^z operators in the transformation is responsible to count the number of fermions to the left of

the site i and then give a sign ± 1 depending on the parity of that count, which results in the anti-commutative property of fermionic operators if one thinks of the normal ordering of operators. The resulting model is known as the Kitaev model [32]:

$$\mathcal{H} = i \sum_{l=1}^{N-1} J_x \gamma_l^y \gamma_{l+1}^x + J_y \gamma_{l+1}^y \gamma_l^x + h_z \gamma_l^y \gamma_l^x, \quad (2.30)$$

Note that this is the result of the mapping for open boundary conditions, while the same mapping for periodic boundaries would create an additional term with a chain product of $2N$ Majorana operators. This is important to note since the ground state degeneracy of the spin model only changes for periodic boundaries if there is frustration (antiferro interaction on an odd length ring), while in the Kitaev model there is no cause for frustration and the degeneracy actually reduces to a single state for a finite periodic boundary system.

Noting that the Hamiltonian only couples γ^x with γ^y Majoranas¹, we can write it as $\mathcal{H} = i \vec{\gamma}^y M \vec{\gamma}^x$, where $(\vec{\gamma}^a)_l \equiv \gamma_l^a$ and M is an $N \times N$ tridiagonal matrix with $M_{l,l+1} = J_x$, $M_{l,l} = h_z$ and $M_{l+1,l} = J_y$. A decomposition of this matrix with a singular value decomposition would result in a model written in terms of coupled pairs of Majoranas as in Eq. (2.4). The left and right vectors associated with the null singular value are precisely the wave-functions of the edge Majorana fermions. These two vectors transform into each other by transposing the matrix M , which is equivalent to $J_x \leftrightarrow J_y$. Let us solve for the right vector, $M \vec{v} = \vec{0}$, which corresponds to finding the solution to

$$\begin{aligned} h v_1 + J_x v_2 &= 0, \\ J_y v_{n-1} + h v_n + J_x v_{n+1} &= 0, \\ J_y v_{N-1} + h v_N &= 0. \end{aligned} \quad (2.31)$$

From the first and second equalities, it follows that

$$v_n = \mathcal{N} \frac{\lambda_+^n - \lambda_-^n}{\lambda_+ - \lambda_-}, \quad \lambda_{\pm} = \frac{h \pm \sqrt{h^2 - 4J_x J_y}}{2J_x}. \quad (2.32)$$

The definitions in Eqs. (2.7) then follow given the relation between left and right edge modes. We can already identify two regimes delimited by $h^2 = 4J_x J_y$. When $h^2 > 4J_x J_y$, both λ_{\pm} are real, one being larger than the other, so v_n is strictly non-zero for any $n > 0$, which means that the third equality

¹This is a consequence of the particle-hole symmetry of the model which is precisely the symmetry that protects the zero modes from gaining energy.

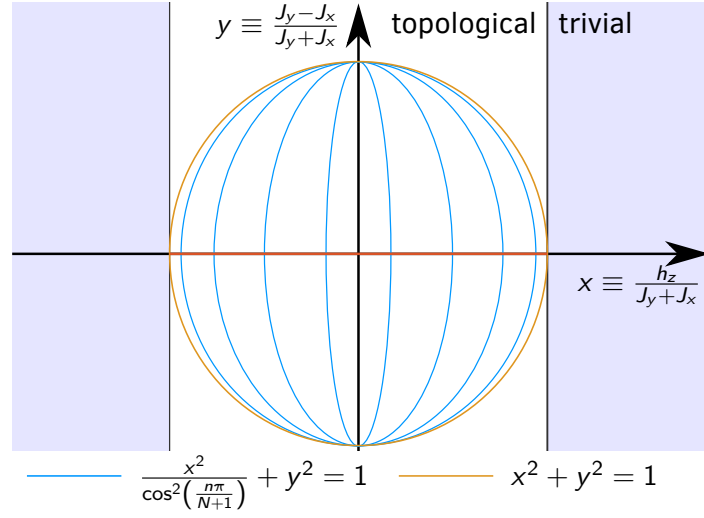


Figure 2.7: The phase diagram of the Kitaev model. The ground state is degenerate when $|x| < 1$, being unique otherwise. The blue ellipses are the finite-size zero mode solutions (Eq. (2.8), $N = 8$ represented). A horizontal cut in $|y| < 1$ will cross the blue lines N times. The cuts $|y| = 1$ are the TFI limits of the model, where a finite-size zero mode is only present when $x = 0$ (Ising model). The orange line ($y = 0$, the gapless XY model [98]) corresponds to a transition between x and y ordered phases in the spin language.

(equivalent to $v_{N+1} = 0$) cannot be satisfied. When $h^2 < 4J_xJ_y$, we can write

$$\lambda_{\pm} = re^{\pm i\theta}, \quad r \equiv \sqrt{\frac{J_y}{J_x}}, \quad \cos(\theta) \equiv \frac{h}{2\sqrt{J_xJ_y}}. \quad (2.33)$$

Solving now for $v_{N+1} = 0$, we get $\sin(N+1)\theta = 0$, from which the zero condition (Eq. (2.5)) follows. Given that \mathcal{N} should go to zero at a phase transition (Eq. (2.8)), we can now map the phase diagram as shown in Fig. 2.7. We can see that the finite-size zeros are governed by the constants λ_{\pm} , which will appear again in the next chapter, where they play the same role as here.

Chapter 3

Perturbative approach to tunneling and quantum interferences in spin clusters

The work in this chapter was done in collaboration with Markus Müller and my supervisor Frédéric Mila, and it was published in 2020 [2]. With respect to the published work, an alternative proof of the cluster independence is offered (Sec. 3.B) and a more general derivation of the zeros of the single spin model is added (Sec. 3.C). Note that we exchange the Ising and magnetic field axes with respect to the equivalent models in the previous chapter ($x \leftrightarrow z$).

3.1 Introduction Quantum tunneling in magnetic clusters has been intensively studied in the nineties as a special case of macroscopic quantum tunneling [99]. Quantum tunneling between two states with very different quantum numbers, e.g. $S_z = S$ and $-S$ for large spin S , is in general a very high-order process since elementary terms such as a transverse field or exchange processes only change this quantum number by 1 or 2, and high-order perturbation calculations of the tunneling were limited to systems with a single tunneling channel [100, 101]. Other approaches included a Wentzel-Kramers-Brillouin (WKB) approximation in the semi-classical limit [101, 102], but the most successful approach proved to be an instanton and path integral formulation [103, 104, 105, 106, 84, 107]. The predictions of these theories, for instance the difference between half-integer and integer spin [105, 106], or the presence of oscillations of the tunneling as a function of a transverse field [84], have been beautifully confirmed by experiments on ferromagnetic molecules that measured Landau-Zener transition probabilities, which are sensitive to the tunneling between nearly degenerate levels [83]. The tunnel splitting was found to oscillate with the transverse field, and the position of the minima of the tunneling amplitudes were shown to alternate depending on whether the difference between the S_z components of the initial and final spin states was even or odd. For a review, see Refs. [82, 108].

More recently, it has become possible to create and control very small clusters of magnetic adatoms deposited on surfaces [51, 109, 110], where

the exchange couplings between adatoms can be tailored by their positioning [111]. One promising idea is to use arrays of small antiferromagnetic (AFM) chains or ladders of Ising spins as a means to store bit information in a very compact way [109]. Applying a large enough voltage pulse with the scanning tunneling microscope (STM) tip, tunneling between the AFM Ising ground states can be induced, providing a way to switch between bit states. The limitation of the associated memory comes from spontaneous tunneling, thermal or quantum, between the two AFM ground states. For low enough temperature, the switching rate between the Ising AFM ground states saturates to the quantum tunneling rate, which decays exponentially with system size. Thus, one way to preserve the bit state longer is to increase the size of the cluster, at the cost of lower density of information. If however quantum tunneling depends strongly on an applied transverse field, with marked minima as in the case of molecular magnets, one could reduce the rate of quantum tunneling without increasing the cluster size. Turning on and off the tunneling by tuning an external parameter, such as the applied transverse field, is not only a way to control the switchability of classical storage units, but it is also a way to manipulate quantum two-level systems (qubit). This is particularly interesting in cases where the relevant two-level system is topologically protected from dephasing noise, as happens e.g. in one-dimensional p-wave superconductors, discussed below.

The first indication that quantum tunneling can be reduced very effectively comes from a recent experiment that demonstrated that anisotropic chains of N spins-1/2 can have ground state crossings as a function of an applied magnetic field [42]. The crossings occur between the two lowest levels which form a quasi-degenerate subspace (which becomes exactly degenerate in the thermodynamic limit). At these crossings, the quantum tunneling between the two states is completely suppressed. For small spin chains, this can easily be demonstrated numerically [85]. A general theory of these level crossings has not yet been developed, however. One step in this direction has been achieved in Ref. [80]. This approach relies on a mapping of the spin model onto a fermionic chain using Jordan-Wigner transformation, and it is thus limited to open chains. A mean-field decoupling of this fermionic model maps it onto the Kitaev model of a one-dimensional p-wave superconductor [32]. This leads to the prediction of exactly N crossings, where N is the number of sites of the chain. In this framework, the crossings are naturally interpreted in terms of the oscillating, exponentially weak coupling between the two Majorana edge states on either end of the chain.

In the following sections, we develop a perturbative approach that pro-

vides a unified and general framework for all these phenomena. It relies on a reformulation of degenerate perturbation theory to lowest non-trivial order in terms of a simple recurrence between flipping amplitudes. This approach leads to a general expression of the tunneling amplitude as a homogeneous polynomial in the amplitude of the transverse exchange processes and of the square of the transverse field. In this approach, the destructive quantum interferences that lead to level crossings appear as a natural consequence of the competition between tunnel processes with positive and negative amplitudes. In the case of a single exchange channel, level crossings will be present as soon as the amplitude of this process is positive (AFM) since it will then compete with the second order process due to the transverse field, which is intrinsically negative. Our approach leads to a number of analytical results in the limit of small exchange processes and transverse field (e.g. the exact solution for the open chain, or for a macroscopic spin), to very good asymptotic expressions for large closed rings and the effect of weak disorder, as well as to general qualitative conclusions (e.g. concerning the number of level crossings in a ring).

In higher dimension, our method still works, as we show on small rectangular, triangular, and cubic clusters, but it becomes rapidly very complex because of the large number of cluster shapes generated in the recurrence. The interest of the method is to show for the example of small clusters that the interference leads to a number of ground state crossings equal to the number of Ising spins, independently of the geometry, suggesting that this remains true for larger systems.

Our formalism turns out to be particularly convenient to study the effect of disorder (such as heterogeneities among different clusters, spatial g -factor variations, weak random fields, etc.) on the suppression of tunneling amplitudes. As we shall see, the suppression of tunneling in the lowest transverse fields is the least affected by disorder. This leads us to the conclusion that in order to achieve a maximally robust suppression of tunneling over a range of potentially fluctuating parameters of clusters, one should use the lowest transverse field for which a ground state crossing occurs in the disorder-free limit.

This chapter is organized as follows: In Sec. 3.2 we introduce the spin models used throughout the rest of the chapter. In Sec. 3.3 we present the iterative perturbation theory method applied to Ising models. In Sec. 3.4, we apply the method to a 1D ring and chain, and in Sec. 3.5 to small 2D and 3D clusters. In Sec. 3.6 we introduce disorder on the perturbative couplings of a ring and obtain the mean square displacement of the transverse field zeros,

as well as the second moment of the tunneling to leading order in the disorder strength. In Sec. 3.7 we apply our method to an anisotropic single spin model and obtain the tunneling amplitude, including an exact result for the crossing field values. In Sec. 3.8 we discuss other systems where one can observe interference between different tunneling paths, and consequently crossings. Finally, in Sec. 3.9 we discuss our results and their experimental consequences.

3.2 Models All the models we consider are spin models and can be written in the form

$$H = H_0 + V, \quad (3.1)$$

where H_0 is a dominant diagonal term with a doubly-degenerate ground state where the two states transform into each other by flipping all spins, and

$$V = \lambda V_1 + \lambda^2 V_2, \quad (3.2)$$

where V_1 and V_2 are perturbations that respectively flip one or two spins. λ is only an auxiliary parameter which we introduce to organize the perturbation expansion. It will be set to 1 later on. We thus require that the matrix elements of $V_{1,2}$ are much smaller than the norm of the terms in H_0 . We use the following notation for the two lowest energy states of the full Hamiltonian H ,

$$H |\Psi_{\pm}\rangle = E_{\pm} |\Psi_{\pm}\rangle. \quad (3.3)$$

Our main goal is to calculate in leading order in λ the splitting $\Delta E \equiv E_+ - E_-$ of the ground state doublet of H_0 .

All the Hamiltonians we consider share the same symmetry, which physically corresponds to a spin reflection across the x - y plane, $S^z \rightarrow -S^z$. We write the symmetry formally in a way that applies to all models, as

$$R \equiv T e^{i\pi S_z}, \quad R^2 = 1, \quad [H, R] = 0, \quad (3.4)$$

where S_z is the total spin projection along z , so that $\exp(i\pi S_z)$ rotates all spins by π around their z axis, and T is the time-reversal operator which inverts all spins.

Let us call the two ground states of H_0 as $|\emptyset\rangle, |\Sigma\rangle$. The operator R flips all spins and transforms one ground state into the other,

$$R |\emptyset\rangle = |\Sigma\rangle, \quad R |\Sigma\rangle = |\emptyset\rangle. \quad (3.5)$$

Taking this into account together with the fact that R is anti-linear, we may

write the (unnormalized) ground states as simultaneous eigenstates of H and R , as

$$|\Psi_{\pm}\rangle = e^{-i\phi_{\pm}/2} |\emptyset\rangle \pm e^{i\phi_{\pm}/2} |\Sigma\rangle + \dots, \quad (3.6)$$

with two unknown phases ϕ_{\pm} . In all the models we consider, ΔE becomes zero for some specific combinations of the couplings. At such points the flipping of the effective two level system is completely suppressed, and thus the information contained in its state is preserved [1]. If in addition the considered two-level system is well isolated from environmental noise (e.g. by topological protection) and from coupling to other degrees of freedom, the exact degeneracy of the two ground states ensures the absence of dephasing in the two-level system, if considered as a qubit.

In the following subsections we introduce the spin models used throughout this chapter. We start with an Ising model with transverse terms, followed by other Ising models which are extensions of that model. One can solve the extended models straightforwardly, only requiring a transformation of the couplings to be able to use the solution of the first Ising model. Finally, we introduce an anisotropic single spin model, a conceptually simpler model than the Ising models, which was studied in the literature to analyze ground state degeneracies, having many similarities to a ferromagnetic Ising model.

3.2.1 Ising model with transverse field and exchange We first consider the Ising model in a small transverse field and subject to weak transverse exchange interactions [80]:

$$\begin{aligned} H_0 &= J_z \sum_{\langle ij \rangle} \sigma_i^z \sigma_j^z, \\ V_1 &= -h_x \sum_i \sigma_i^x, \quad V_2 = J_x \sum_{\langle ij \rangle} \sigma_i^x \sigma_j^x. \end{aligned} \quad (3.7)$$

Here σ are the Pauli matrices and N is the number of Ising spins. We keep the lattice general for now, however, we do require that the lattice be classically unfrustrated, such that the ground state manifold of H_0 is only doubly degenerate. In the following sections we will carry out more detailed calculations by restricting ourselves to specific lattices and Ising interactions.

We denote the Ising eigenstates and energies as

$$H_0 |m\rangle = \varepsilon_m |m\rangle, \quad (3.8)$$

where $|m\rangle$ are the classical Ising configurations with the spins either up or

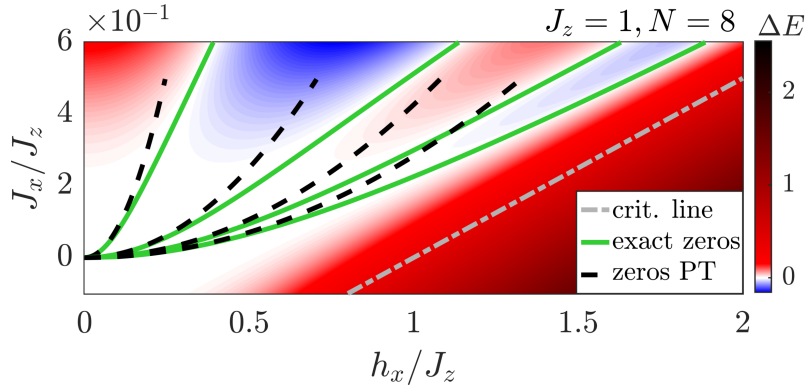


Figure 3.1: Color plot of the energy difference between the two lowest energy eigenstates $|\Psi_{\pm}\rangle$ (Eq. (3.6)) of the full Hamiltonian (3.7) on a spin chain of 8 spins, obtained with exact diagonalization. A change of sign in ΔE indicates a crossing between the opposite parity states and therefore a change of the ground state parity. The full lines indicate the locations where the ground state is degenerate, while the dashed lines indicate our perturbative prediction (Eq. (3.63)), which works very well for small fluctuation parameters J_x and h_x . Calculating the energy gap close to the phase transition $h_x = J_z, J_x = 0$ perturbatively in the small parameters $h_x - J_z$ and J_x yields $\Delta \approx 2(h_x - J_z - 2J_x)$ [112]. This gives the approximate location of the quantum critical line between the Ising-ordered and the paramagnetic phases as $J_x \approx (h_x - J_z)/2$, as shown in the plot. This is still accurate for large J_x since a similar calculation close to the phase transition at $(h_x = 2J_x, J_z = 0)$ gives the same gap [92]. For the full phase diagram, see Ref. [113]. There are no zeros when $J_x < 0$, and the ordered phase shrinks with increasingly negative J_x . Both reflect the fact that the transverse terms reinforce each other for $J_x < 0$, while they compete for $J_x > 0$.

down along the axis z . We label the states $|m\rangle$ by the set m of spins that are flipped with respect to one of the Ising ground states. By definition, our reference ground state corresponds to the empty set $m = \emptyset$, and the other ground state to $m = \Sigma$, the set of all spins. The energy of these two states is $\varepsilon_\emptyset (= \varepsilon_\Sigma)$.

Before proceeding with introducing various extensions, let us comment on the ground state degeneracies of the full Hamiltonian H on the spin chain with even N . When $J_x > 0$ and for finite size, there are lines in the (J_x, h_x) -plane where the ground state is degenerate, as shown in Fig. 3.1. In our perturbative regime, these lines scale as $h_x \sim \sqrt{J_x |J_z|}$. The lines continue for larger J_x, h_x , but the scaling becomes linear. In fact, when $J_x, h_x \gg J_z$, all lines except one approach the critical line $J_x = h_x/2$ of the $J_z = 0$ classical model (an AFM Ising with longitudinal field), separating the AFM-ordered phase along x from the PM phase. The classical ground state on this critical line is highly degenerate, but the J_z exchange coupling lifts the degeneracy and induces many ground state crossings close to the classical critical line. The line corresponding to the smallest field for given J_x instead approaches the classical critical line $J_x = h_x$. On that line it costs no energy to flip the terminal spin of the chain which is anti-aligned to the external field in the AFM phase. This separate degeneracy line is present only for chains with even N .

3.2.2 Ising model with a staggered field The first extension we consider is a staggering of the magnetic field on bipartite lattices with the same number of sites on either sublattice, but different transverse fields $h_{x,A}$ and $h_{x,B}$ acting on the two sublattices A and B , respectively. Thus, the modified perturbation is

$$V_1 = - \left(h_{x,A} \sum_{i \in A} \sigma_i^x + h_{x,B} \sum_{i \in B} \sigma_i^x \right), \quad (3.9)$$

with unchanged V_2 . In Fig. 3.2 we show the ground state energy splitting of the full Hamiltonian H of this model as a function of the staggered fields. The zero lines scale as $h_{x,A} h_{x,B} \sim J_x |J_z|$, but only when $h_{x,A} h_{x,B} J_x > 0$ do ground state degeneracies occur, that is, only when the field and the exchange coupling favor opposite ground state configurations. In general we can state that tunneling suppression occurs when the transverse fluctuations are competing or "frustrated".

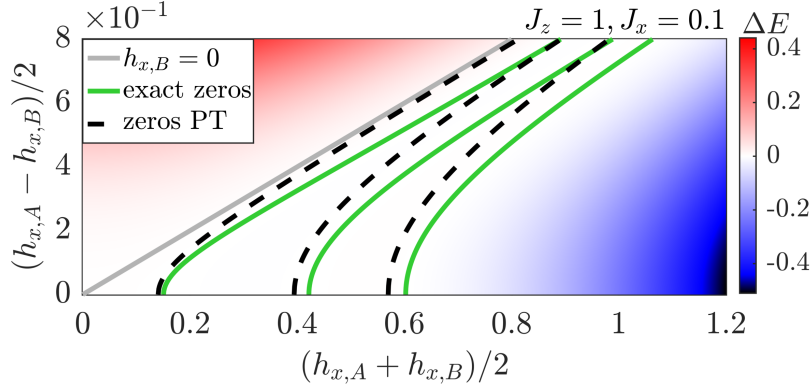


Figure 3.2: Color plot of the exact energy difference between the two lowest energy eigenstates $|\Psi_{\pm}\rangle$ (Eq. (3.6)) of the full Hamiltonian defined in Sec. 3.2.2 on a spin chain of 6 spins, obtained with exact diagonalization. The full green lines indicate the locations where the ground state is degenerate, while the dashed lines indicate the prediction from perturbation theory (Eqs. (3.35, 3.63)). The diagonal $h_{x,B} = 0$ is marked to show that the zeros only occur in the region where the field and the exchange term V_2 favor opposite ground states.

3.2.3 Ising model with general transverse couplings We will also extend the model by having transverse couplings along both transverse axes,

$$\begin{aligned} V_1 &= - \sum_i (h_x \sigma_i^x + h_y \sigma_i^y), \\ V_2 &= \sum_{\langle ij \rangle} (J_x \sigma_i^x \sigma_j^x + J_y \sigma_i^y \sigma_j^y). \end{aligned} \quad (3.10)$$

On a 1D chain of spins with open boundary conditions, this model has an interesting limit in which it is exactly solvable. Taking $J_y = h_x = 0$, one can map the model with a Jordan-Wigner transformation [29] onto the Kitaev chain model [32], a free fermion model which one can solve exactly [80, 1] to obtain field values in which not only the ground state is degenerate, but all eigenstates are:

$$h_y^{(n)} = 2\sqrt{J_x J_z} \cos \left(\frac{\lfloor N/2 \rfloor + 1 - n}{N+1} \pi \right), \quad (3.11)$$

where $n = 1, \dots, \lfloor N/2 \rfloor$. If we take $J_x > 0$, these zeros only appear if $J_z > 0$, as one can see in Fig. 3.3. Interestingly, our perturbative approach yields exactly the same expression in the appropriate limit (Eqs. (3.63, 3.44)), with no higher order corrections. This is presumably a consequence of the fact that the zero energy Majorana fermions do not backscatter, so that our leading or-

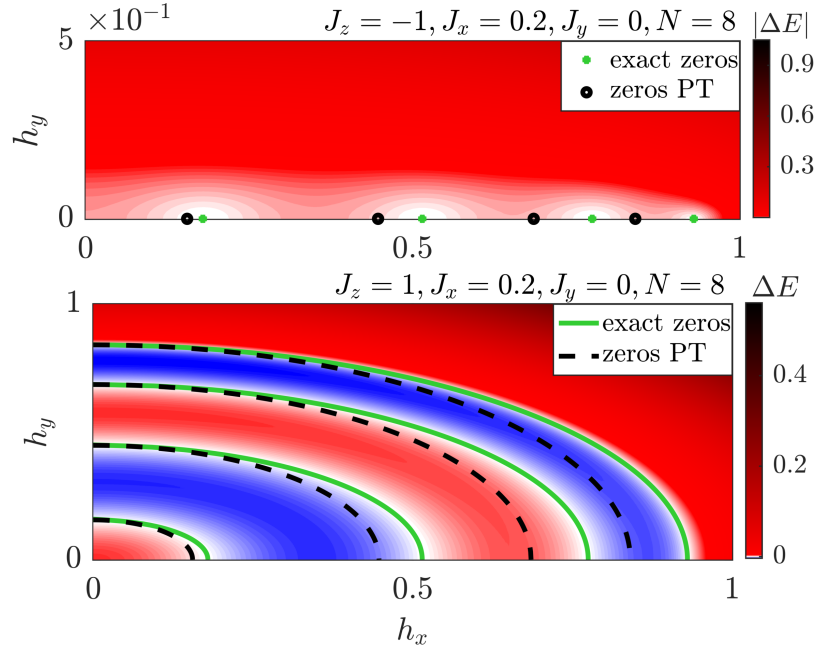


Figure 3.3: Color plot of the exact energy difference between the two lowest energy eigenstates $|\Psi_{\pm}\rangle$ (Eq. (3.6)) of the full Hamiltonian defined in Sec. 3.2.3 on a spin chain of 8 spins, obtained with exact diagonalization. We set $J_y = 0$, $J_x = 0.2$ so we may study the energy splitting in the h_x - h_y plane. The ground state crossings are drastically different depending on the sign of J_z . If the ground state is ferromagnetic (above), there are only degeneracies when $h_y = 0$ (These are the same zeros as in Fig. 3.1 along the $J_x = 0.2$ line). This is predicted by our perturbative calculations, where we obtain the zeros marked in black as given by Eq. (3.39). In the antiferromagnetic case (below), we obtain lines of zeros in the plane which connect the crossings of the model (3.7) (along the x axis) to the exact crossings of the Kitaev chain model given by Eq. (3.11) (along the y axis). These lines are consistent with the perturbative solution (dashed line), where we find that the zeros do not depend on the orientation of the field in the x - y plane (Eq. (3.44)).

der approximation, which is equivalent to a forward scattering approximation for the fermions, becomes exact [114].

3.2.4 Single spin model Instead of studying a cluster of N spins explicitly with all its internal couplings, one may consider the cluster as a big effective spin S and consider the tunneling from the up to the down state of this composite spin. The precise Hamiltonian for this equivalent big spin would in general be very complex. However, qualitative features can be expected to be captured by simple effective interactions which can be written as low powers of the total spin operators $S_{x,y,z}$.

A transverse field on a ferromagnetic cluster of spins naturally translates into a transverse field acting on the big spin. Also, the ferromagnetic Ising configurations are the projections with largest total S_z of the largest spin one can form with N ($S = 1/2$)-spins. Thus, the ground state of a Hamiltonian of the form $-S_z^2$ corresponds to a ferromagnetic Ising ground state of the original cluster. Indeed, we shall see later that this model captures qualitatively the features of a ferromagnetic Ising model ($J_z < 0$) as considered in Sec. 3.2.3. In contrast, it is not clear whether such an approximate mapping is meaningful for antiferromagnetic clusters.

Here we will reconsider quadratic single spin Hamiltonians equivalent to those considered earlier in the literature [84, 100, 102, 83]. In particular, we take the most general quadratic single spin model with anisotropy and a field transverse to the easy axis. Upon choosing axes that bring the quadratic part to a diagonal form, we are left with three quadratic couplings $J_{x,y,z}$. We are free to choose the easy, medium and hard axes to be, respectively, along the z -, y - and x -axes (i.e., $J_z \leq J_y \leq J_x$). We are also free to set one of these couplings to zero, since the ground state splitting will be independent of a constant term $J\vec{S} \cdot \vec{S}$ that one can add to the Hamiltonian. We therefore consider the Hamiltonian

$$\begin{aligned} H_0 &= J_z S_z^2, \\ V_1 &= -(h_x S_x + h_y S_y), \quad V_2 = J_x S_x^2, \end{aligned} \quad (3.12)$$

where we chose $J_y = 0$, implying that $J_z \leq 0$ and $J_x \geq 0$. We could recover the dependence on a J_y coupling with the transformations

$$J_x \rightarrow J_x - J_y, \quad J_z \rightarrow J_z - J_y. \quad (3.13)$$

When performing perturbative calculations, we assume that

$$|J_z| \gg |J_x|, |h_x|, |h_y|. \quad (3.14)$$

This model has $2S = N$ values of the magnetic field where the ground state is doubly degenerate, as demonstrated by A. Garg [84] using path integral and instanton calculations justified at large S , but without restricting to the perturbative regime (3.14). In the considered large S limit, the crossings can be interpreted as the negative interference of two tunneling instantons having different Berry phases. We shall derive a very similar result within perturbation theory, but without relying on the size of the spin (or N) and without taking a saddle point approximation.

We will show in Sec. 3.7 that here again the underlying mechanism behind the zeros is the competition of multiple tunneling paths with oscillating signs. Finally, using a different approach we will derive non-perturbatively the location of the $2S$ equally spaced transverse field zeros without relying on any approximation.

3.3 Perturbation theory for collective tunneling In this section we will present the perturbative method applied to Ising models defined in Sec. 3.2. The method is derived in more detail in Sec. 3.A.

Standard techniques to carry out degenerate perturbation theory at arbitrarily high orders construct a perturbative expansion for an effective Hamiltonian H_{eff} which only acts on the Hilbert space spanned by unperturbed states and yields the exact splitting of the ground state manifold due to perturbations. Let us call the set of unperturbed ground state configurations $g = \{\emptyset, \Sigma\}$. Defining P as the projector onto the subspace g , one constructs H_{eff} which projects out all the excited states, i.e., $PH_{\text{eff}} = H_{\text{eff}}P = H_{\text{eff}}$. However, H_{eff} is not fully specified by these requirements. A first full series expansion for a possible choice of H_{eff} was obtained in [115] for a general Hamiltonian with a discrete spectrum. It leads to a generalized eigenvalue equation that must be solved for the split ground state energies. A variation of [115] was later given in [116], where the eigenvalue equations are simpler, but the operator H_{eff} will in general turn out to be non-Hermitian. Here we use the latter approach. The eigenvalue equations of this effective Hamiltonian are

$$H_{\text{eff}}P|\Psi_{\pm}\rangle = E_{\pm}P|\Psi_{\pm}\rangle, \quad (3.15)$$

where $|\Psi_{\pm}\rangle$ are the lowest energy eigenstates of H . Owing to the anti-linear symmetry R (Eq. (3.4)), which lets us write $|\Psi_{\pm}\rangle$ as in Eq. (3.6), we deduce

that the energy splitting is given by

$$\Delta E = (e^{i\phi_+} + e^{i\phi_-}) \langle \emptyset | H_{\text{eff}} | \Sigma \rangle, \quad (3.16)$$

in terms of the off-diagonal matrix element of the effective Hamiltonian. Our perturbative method allows us calculate the matrix element $\langle \emptyset | H_{\text{eff}} | \Sigma \rangle$ to leading order in λ . Since V_1 and V_2 respectively flip one or two spins when acting on $|m\rangle$, and given that $V = \lambda V_1 + \lambda^2 V_2$, the power of λ of a tunneling path between $|\emptyset\rangle$ and $|\Sigma\rangle$ corresponds to the number of spin flips that occurred. Since the shortest paths have exactly N spin flips (each spin flips once and only once), it follows that λ^N is the lowest order that will occur, and thus

$$\langle \emptyset | H_{\text{eff}} | \Sigma \rangle = t_N \lambda^N + O(\lambda^{N+1}), \quad (3.17)$$

where we have defined t_N as the leading order term.

In the limit $\lambda \rightarrow 0$, the phases in Eq. (3.6) must vanish, $\phi_{\pm} \rightarrow 0$. This follows from the fact that in this limit the ground states approach the two linear combinations

$$|\Psi_{\pm}\rangle \rightarrow |\emptyset\rangle \pm |\Sigma\rangle + O(\lambda). \quad (3.18)$$

One thus finds

$$|\Delta E| = 2|t_N| + O(\lambda^{N+1}). \quad (3.19)$$

As shown in Sec. 3.A, the tunneling amplitude is given by

$$t_N = \sum_{n=\lceil \frac{N}{2} \rceil}^N \sum_{\{l_i\}} \langle \emptyset | V_{l_1} S \dots V_{l_{n-1}} S V_{l_n} | \Sigma \rangle \quad (3.20)$$

where the $l_{i=1,\dots,n} \in \{1, 2\}$ obey $l_1 + l_2 + \dots + l_n = N$, and

$$S \equiv - \sum_{m \notin g} \frac{|m\rangle \langle m|}{\Delta \varepsilon_m}, \quad (3.21)$$

where $\Delta \varepsilon_m \equiv \varepsilon_m - \varepsilon_{\emptyset}$ is the unperturbed excitation energy of the state $|m\rangle$. Let us denote by $|m|$ the cardinality of the set m , that is, the number of spins that are flipped relative to the ground state \emptyset , so that $|\Sigma| = N$. The tunneling t_N can be calculated recursively. To this end we introduce c_m as an intermediate

tunneling coefficient, analogous to t_N in Eq. (3.20),

$$c_m \equiv \sum_{n=\lceil \frac{|m|}{2} \rceil}^{|m|} \sum_{\{l_i\}} \langle \emptyset | V_{l_1} S \dots V_{l_{n-1}} S V_{l_n} S | m \rangle, \quad (3.22)$$

where we impose the condition $l_1 + l_2 + \dots + l_n = |m|$, on the l_i , which restricts the sum to the terms that contribute to leading order ($\lambda^{|m|}$) to the tunneling between $|\emptyset\rangle$ and $|m\rangle$. Finally, by inserting the identity as $\sum_{m'} |m'\rangle \langle m'|$ before the last two factors and expanding $V_{l_n} S |m\rangle$, one obtains a recursion relation that connects c_m to coefficients of smaller clusters $m' \subset m$, yielding the cluster recursion relations

$$c_m = -\frac{1}{\Delta \varepsilon_m} \left(\sum_{i \in m} \langle m \setminus \{i\} | V_1 | m \rangle c_{m \setminus \{i\}} + \sum_{i,j \in m} \langle m \setminus \{i,j\} | V_2 | m \rangle c_{m \setminus \{i,j\}} \right), \quad (3.23)$$

where we sum over flipped spins $i \in m$, or pairs of flipped spins $\{i,j\} \in m$. An analogous expression follows for t_N ,

$$t_N = \sum_{i \in \Sigma} \langle \Sigma \setminus \{i\} | V_1 | \Sigma \rangle c_{\Sigma \setminus \{i\}} + \sum_{i,j \in \Sigma} \langle \Sigma \setminus \{i,j\} | V_2 | \Sigma \rangle c_{\Sigma \setminus \{i,j\}}. \quad (3.24)$$

The recursions (3.23, 3.24) hold for general perturbations $V_{1,2}$ which flip single spin or pairs of spins, respectively. It is straightforward to generalize the recursions (3.23) to include higher order terms of the form $\lambda^k V_k$, which flip k spins.

The iterative procedure can be further simplified due to the independence of disconnected clusters. Let us consider a cluster m that is composed of several mutually disconnected clusters m_i of spins flipped relative to \emptyset . We call a set of clusters disconnected if the excitation energy of the set is the sum of the excitation energies of the individual clusters, i.e. $\Delta \varepsilon_m = \Delta \varepsilon_{m_1} + \Delta \varepsilon_{m_2} + \dots + \Delta \varepsilon_{m_n}$. In Sec. 3.B, we show that for such separable sets, the intermediate tunneling coefficient is the product of tunneling coefficients for their disconnected components,

$$c_m = c_{m_1} c_{m_2} \dots c_{m_n}. \quad (3.25)$$

To calculate t_N for a given cluster one proceeds as follows: One identifies all inequivalent connected subclusters m of the considered spin cluster, associates a coefficient c_m to each of them, and uses Eqs. (3.23, 3.25) to calculate the coefficients recursively for increasing cluster sizes $|m|$. We say that two clusters are equivalent if their coefficients c_m are the same, which is for instance the case if the two clusters are symmetry related.

If the unperturbed Hamiltonian is the Ising model with nearest neighbor couplings, the excitation energy $\Delta\varepsilon_m$ of a cluster is $2|J_z|$ times the number of bonds that connect flipped spins ($\in m$) to unflipped spins ($\in \Sigma \setminus m$). In other words, the excitation energy is proportional to the total length of all domain walls between m and its complement.

In general, the recursions (3.23, 3.24) can be rather complicated to solve, especially if one has to consider a large number of inequivalent clusters. However, we will see in the following subsections that they take a simplified form when applied to some of our models, and even result in recursion relations with closed form solutions in some cases. Applying the method to the first Ising model (3.7), our next step, will be very instructive.

3.3.1 Tunneling in Ising models with transverse field and exchange Let us consider the model (3.7) and let us apply the recursion relations (3.23, 3.24) to it. The first thing to note is that the matrix elements in the recursion relations simplify greatly. They are given by

$$\langle m \setminus \{i\} | V_1 | m \rangle = -h_x \quad (3.26)$$

and

$$\langle m \setminus \{i, j\} | V_2 | m \rangle = J_x \quad (3.27)$$

if i, j are nearest neighbors, and vanish otherwise. Then, the recursion relations become

$$c_m = \frac{1}{\Delta\varepsilon_m} \left(h_x \sum_{i \in m} c_{m \setminus \{i\}} - J_x \sum_{\langle ij \rangle \in m} c_{m \setminus \{i, j\}} \right), \quad (3.28)$$

$$t_N = -h_x \sum_{i \in \Sigma} c_{\Sigma \setminus \{i\}} + J_x \sum_{\langle ij \rangle \in \Sigma} c_{\Sigma \setminus \{i, j\}}. \quad (3.29)$$

In this model, two clusters are equivalent if they are identical including their environment up to their first neighbors. As an example of this, consider a cluster of flipped spins in the bulk of a lattice with open boundary conditions. Any translation by a lattice unit whereby the cluster does not touch the bound-

aries results in an equivalent cluster. When a boundary is reached instead, the first neighbors of the cluster change and we will find a different cluster coefficient.

Since t_N is the sum over all tunnel paths that flip every spin exactly once, it is clear that the resulting expression is a polynomial in h_x and J_x , each term being proportional to a product $J_x^k h_x^{N-2k}$ with $0 \leq k \leq \lfloor N/2 \rfloor$. The general form for the tunneling coefficient of a cluster of N spins, regardless of the lattice, will thus take the form

$$t_N = \sum_{k=0}^{\lfloor \frac{N}{2} \rfloor} a_k \frac{J_x^k h_x^{N-2k}}{|J_z|^{N-k-1}} \quad (3.30)$$

$$\propto \frac{h_x^{\text{mod}(N,2)}}{|J_z|^{2\lfloor \frac{N}{2} \rfloor - 1}} \prod_{n=1}^{\lfloor \frac{N}{2} \rfloor} (J_x |J_z| - \alpha_n h_x^2), \quad (3.31)$$

with some lattice-dependent real coefficients a_k , and (potentially complex) roots α_n . Note that Kramers theorem is satisfied by Eq. (3.30), which yields $t_N \sim h_x$ for odd N : Indeed, the ground state must be doubly degenerate (i.e. $t_N = 0$) if there is time-reversal symmetry ($h_x = 0$) and the total spin is half-integer (N is odd).

Due to the minus sign in the projector S (Eq. (3.21)), the sign of a_k reflects the number of flipping terms $V_{1,2}$ that are applied on the corresponding tunneling paths. The sign thus alternates with k :

$$\text{sgn}(a_k) = (-1)^{k-1}, \quad (3.32)$$

where we have also taken into account the negative sign of the matrix element of V_1 in Eq. (3.26). If $J_x < 0$, all monomials contribute with the same sign, and thus $|t_N|$ grows monotonously with the field h_x , with no zero crossing. However, if $J_x > 0$, there is a negative interference between paths with different numbers of perturbative steps, and t_N may oscillate as a function of the field. In this case, we can have ground state crossings. If the polynomial of Eq. (3.31) has positive real roots α_n , the crossings occur at the fields

$$h_x^{(n)} = \pm \alpha_n^{-1/2} \sqrt{J_x |J_z|}. \quad (3.33)$$

Thus there may be up to N values of the transverse field (or $\lfloor N/2 \rfloor$, if one restricts to $h_x \geq 0$) where $t_N = 0$, depending on the number of real α_n . (Note that real α_n are necessarily positive, since negative α_n would imply zeros for $J_x > 0$, which is excluded).

Later on we will solve the recursion relations for specific spin clusters and lattices, where we do find that in all cases considered the α_n are real and positive. For now, let us assume that indeed all $\alpha_n > 0$, so that we have either N degeneracy points or none (except for the trivial one $h_x = 0$ for odd N), depending on the sign of J_x .

3.3.2 Tunneling in Ising models with a staggered field We consider the model presented in Section 3.2.2 where the field of the model (3.7) is staggered. One could calculate the matrix elements and write down the recursion relations for this model, but this turns out to be unnecessary. Let us first guess the polynomial form of t_N for this model. The tunneling paths due to transverse exchange only contribute with a factor $J_x^{N/2}$. For tunneling paths involving spins flipped by transverse fields, those must come in equal numbers on the two sublattices, and thus t_N must take the form

$$t_N = \frac{J_x^{N/2}}{|J_z|^{N/2-1}} \sum_{k=0}^{N/2} a_k \left(\frac{h_{x,A} h_{x,B}}{J_x |J_z|} \right)^{N/2-k}, \quad (3.34)$$

where the coefficients a_k must be the same as those of the polynomial for a homogeneous field h_x , cf. Eq. (3.30). Thus one simply should substitute $h_x^2 \rightarrow h_{x,A} h_{x,B}$ in that equation. It follows that ground state degeneracy occurs whenever

$$h_{x,A} h_{x,B} = \alpha_n^{-1} J_x |J_z|. \quad (3.35)$$

The condition $h_{x,A} h_{x,B} J_x > 0$ is a general prerequisite for such degeneracies. If all α_n are positive, we recover the behavior observed numerically in Fig. 3.2

3.3.3 Tunneling in Ising models with general transverse couplings In the case of the more general Ising models (3.10), we found the behavior of the ground state crossings to depend on the Ising ground state (Fig. 3.3). In particular, we distinguish whether the dominant Ising interactions are ferromagnetic ($J_z < 0$) or antiferromagnetic ($J_z > 0$), respectively.

Ising ferromagnets Since the ground state is ferromagnetic, and since we only flip each spin once, the matrix element $\langle m \setminus \{i, j\} | V_2 | m \rangle$ appears in the recursion relations only in the form

$$\langle \uparrow\uparrow | V_2 | \downarrow\downarrow \rangle = J_x - J_y, \quad (3.36)$$

for two neighboring spins, while $\langle m \setminus \{i\} | V_1 | m \rangle$ only appears as

$$\langle \uparrow | V_1 | \downarrow \rangle = -h_x + ih_y. \quad (3.37)$$

This implies that the resulting recursion and the tunneling amplitude t_N will be the same as Eqs. (3.28, 3.30), up to the substitution

$$\begin{aligned} J_x &\rightarrow J_x - J_y, \\ h_x &\rightarrow h_x - ih_y, \end{aligned} \quad (\text{Ferro}) \quad (3.38)$$

and it suffices to solve the model (3.7).

Performing the substitution in Eq. (3.33), one finds that the tunneling only vanishes if either $h_y = 0$ and $J_x > J_y$, in which case there are zeros at the fields

$$h_x^{(n)} = \pm \left(\frac{(J_x - J_y)|J_z|}{\alpha_n} \right)^{1/2}, \quad (3.39)$$

or if $h_x = 0$ and $J_y > J_x$, at fields

$$h_y^{(n)} = \pm \left(\frac{(J_y - J_x)|J_z|}{\alpha_n} \right)^{1/2}. \quad (3.40)$$

In other words, the transverse field has to be applied in the spin direction which corresponds to the stronger antiferromagnetic (or weaker ferromagnetic) exchange. This is analogous to the result found in the single spin case by Garg [84], which we will review in Section 3.7 below.

Ising antiferromagnets For antiferromagnetic Ising models case, let us consider a bipartite lattice, so that the ground states have opposite spins on each sublattice. V_2 only acts in the form

$$\langle \uparrow \downarrow | V_2 | \downarrow \uparrow \rangle = J_x + J_y, \quad (3.41)$$

while V_1 flips spins from down to up on one sublattice and from up to down on the other sublattice,

$$\langle \uparrow | V_1 | \downarrow \rangle = -h_x + ih_y, \quad \langle \downarrow | V_1 | \uparrow \rangle = -h_x - ih_y. \quad (3.42)$$

We take each sublattice to have the same number of spins. Since the lattice is bipartite and V_2 flips one spin from each sublattice, there must be an equal number of single flips due to V_1 on either sublattice. This implies that we can

simply substitute

$$\begin{aligned} J_x &\rightarrow J_x + J_y, \\ h_x^2 &\rightarrow h_x^2 + h_y^2, \end{aligned} \quad (\text{Antiferro}) \quad (3.43)$$

in Eqs. (3.28, 3.30) to obtain the result for the generic, bipartite antiferromagnetic Ising models. Interestingly, the direction of the homogeneous transverse field in the $x - y$ plane is irrelevant. That is, zeros of the tunneling amplitude occur in circles in the transverse field plane, provided that the transverse exchange is predominantly antiferromagnetic ($J_x + J_y > 0$). The tunneling vanishes for transverse fields of magnitude

$$h^{(n)} = \left(\frac{(J_x + J_y)|J_z|}{\alpha_n} \right)^{1/2}, \quad (3.44)$$

regardless of its angle in the $x - y$ plane. While there is no angle dependence to leading order, the radial symmetry is broken by higher order corrections as confirmed numerically in Fig. 3.3.

Note that the tunneling matrix element t_N is in general complex, and thus the condition $t_N = 0$ determines a manifold of codimension 2 in the parameter space of transverse couplings. Thus, by fixing the exchange couplings J_x, J_y and looking for zeros in the transverse field plane, one will generically only find isolated points, as it happens in the case of ferromagnetic clusters. A qualitatively different situation arises in antiferromagnetic clusters because there, owing to the substitution (3.43), the tunneling amplitude is always real, such that zeros organize in a manifold of codimension 1, i.e., closed lines in the transverse field plane.

3.4 Tunneling in 1D systems In this section we apply our method to the 1D model (3.7). The recursion relations for 1D systems are rather simple because any connected cluster of flipped spins is uniquely defined by its length and position. We first consider a ring of N spins, where the exact solution of the recursion allows us to extract explicit asymptotic expressions for large N . Then we consider an open chain, where we even obtain a closed analytical expression for t_N for any N .

3.4.1 Closed chain: a ring of spins For a ring of spins, all connected clusters of a given length are equivalent. We denote by c_l the intermediate tunneling coefficient associated with a cluster of length l . The application of Eq. (3.28) is straightforward: By unflipping a single spin from the cluster, we obtain one

of l possible states with $l - 1$ flipped spins. If the unflipped spin is at the edge of the cluster, its contribution to c_l is $h_x c_{l-1} / (4|J_z|)$, since the excitation energy of the cluster is $4|J_z|$ due to the two domain walls at its ends. If the unflipped spin is in the bulk then the state consists of two clusters. We thus use Eq. (3.25) to write the contribution of that state as $h_x c_n c_{l-n-1}$ for some $0 < n < l$. Defining $c_0 \equiv 1$ we can combine the edge and the bulk terms, and using an analogous reasoning for the term related to J_x we finally have

$$c_l = \frac{h_x}{4|J_z|} \sum_{n=0}^{l-1} c_n c_{l-n-1} - \frac{J_x}{4|J_z|} \sum_{n=0}^{l-2} c_n c_{l-n-2}. \quad (3.45)$$

To obtain the polynomial for the full tunneling coefficient t_N , a similar recursion can be used. It slightly differs from the above due to the periodic boundary conditions. Unflipping a pair or a single spin in the ring, we are left with a single cluster of length $N - 2$ or $N - 1$. The unflipped spin(s) can be at N positions, so that we find

$$t_N = N(-h_x c_{N-1} + J_x c_{N-2}). \quad (3.46)$$

In general the location of the field-zeros $h_x^{(n)}$ depends on N . Interestingly, it turns out that the pair of largest zeros, $\pm h_x^{([N/2])}$, is common to chains of any size and takes the value $h_x^{([N/2])} = 2\sqrt{J_x|J_z|}$. To show that this is indeed so, we start from Eq. (3.46). The condition to have $t_{l+1} = 0$ requires $c_l = (J_x/h_x)c_{l-1}$. If this is to hold for all l and given that $c_0 = 1$, we must have $c_l = (J_x/h_x)^l$. Using this in Eq. (3.45) and simplifying we find that this relation is indeed satisfied if $h_x = \pm 2\sqrt{J_x|J_z|}$. For this value of h_x the tunneling t_N thus vanishes for any N . We will retrieve this result from a direct calculation of t_N below.

In order to calculate t_N for any value of h_x , we define the generating functions

$$\begin{aligned} C(z) &= \sum_{l=0}^{\infty} z^l c_l, \\ T(z) &= 2|J_z| + \sum_{l=1}^{\infty} z^l \frac{t_l}{l}, \end{aligned} \quad (3.47)$$

where z is a complex variable. We then multiply Eqs. (3.45, 3.46) by z^l , and sum them from $l = 2$ to $l = \infty$. After summing over l in Eq. (3.45), one obtains terms with double summations of the form $\sum_{l=0}^{\infty} \sum_{n=0}^l$, which are equal to $\sum_{n=0}^{\infty} \sum_{l=n}^{\infty}$. Those lead to a term $C(z)^2$ on the right-hand side. Solving the resulting quadratic equation for $C(z)$, one has to choose the root that satisfies

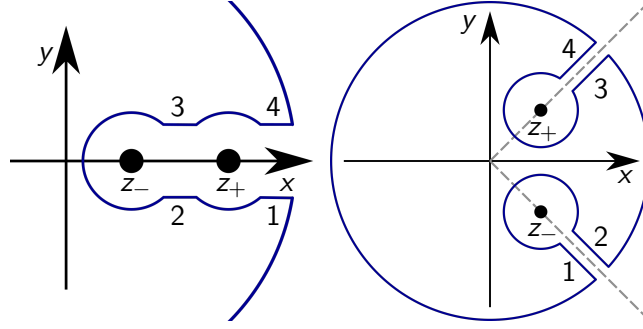


Figure 3.4: Keyhole contours of integration.

$\lim_{z \rightarrow 0} C(z) = c_0 = 1$. Using the same steps in Eq. (3.46) one obtains $T(z)$. Solving for $C(z)$ and eventually for $T(z)$, we obtain the closed expression

$$T(z) = \sqrt{4J_x|J_z|(z - z_+)(z - z_-)}, \quad (3.48)$$

where

$$z_{\pm} = \frac{h_x \pm \sqrt{h_x^2 - 4J_x|J_z|}}{2J_x}. \quad (3.49)$$

The above formula for $T(z)$ represents the power series (3.48) with its domain of convergence at small enough z , but analytically continues it beyond. We can now calculate t_N by contour integration of $T(z)/z^{N+1}$ around its pole at $z = 0$. We have the exact expression

$$\frac{t_N}{N} = \frac{1}{2\pi i} \oint_{z=0} \frac{T(z)}{z^{N+1}} dz. \quad (3.50)$$

We now deform the contour, pushing it to infinity, but avoiding the branch cuts ending at z_{\pm} . This is best done using keyhole contours (Fig. 3.4). The precise contour used depends on whether z_{\pm} are real or a pair of complex conjugate numbers, which we discuss separately. We restrict ourselves to $J_x > 0$, since only in that case t_N exhibits interesting oscillations.

$h_x^2 > 4J_x|J_z|$ - In this case, both z_{\pm} are real and either both positive or both negative, depending on the sign of h_x . Without loss of generality, we take $h_x > 0$. The appropriate contour is shown in Fig. 3.4 on the left. Pushing the radius of the large circle to infinity and letting the radius of the small circles around z_{\pm} shrink to zero, the integrals 1 and 4 cancel, while the integrals 2

and 3 between the branch points add up to

$$t_N = -\frac{2N\sqrt{J_x|J_z|}}{\pi} \int_{z_-}^{z_+} \frac{\sqrt{(z_+ - x)(x - z_-)}}{x^{N+1}} dx. \quad (3.51)$$

Note that upon changing h_x within the domain $h_x^2 > 4J_x|J_z|$, the integrand remains positive, and thus t_N never becomes zero.

$h_x^2 = 4J_x|J_z|$ - At the border of the above domain one has $z_+ = z_-$. From Eq. (3.51) one sees that the tunneling becomes zero at this point, independently of N , as we have already found previously. Since there are no zeros at higher fields, this corresponds to the largest field zero.

$h_x^2 < 4J_x|J_z|$ - Here the branch points become a pair of complex conjugate numbers. We have

$$z_{\pm} = r_0 e^{\pm i\theta_0}, \quad (3.52)$$

where

$$r_0 = \sqrt{\frac{|J_z|}{J_x}}, \quad \cos(\theta_0) = \frac{h_x}{\sqrt{4J_x|J_z|}}. \quad (3.53)$$

We consider the contour shown in Fig. 3.4 on the right, where the branch points z_{\pm} are avoided with keyholes oriented radially along the lines $z = re^{\pm i\theta_0}$. Shrinking the small circles to zero, and expanding the large circle to infinity, the expression for t_N simplifies to the contribution of two line integrals along the radial branch cuts, resulting in the exact expression:

$$t_N = \frac{4N\sqrt{J_x|J_z|}}{\pi} \times \text{Im} \left(e^{i\theta_0(\frac{1}{2}-N)} \int_{r_0}^{\infty} \frac{\sqrt{(r-r_0)(re^{i\theta_0}-r_0e^{-i\theta_0})}}{r^{N+1}} dr \right). \quad (3.54)$$

At large N , we can make progress by replacing $re^{i\theta_0} - r_0e^{-i\theta_0}$ by its value at $r = r_0$ (which is valid as long as $\theta_0 \gg 1/N$). The remaining integral can be written in terms of Gamma functions. To leading order at large N one obtains

$$t_N \approx |J_z| \left(\frac{J_x}{|J_z|} \right)^{N/2} \sqrt{\frac{8 \sin \theta_0}{\pi N}} \sin \left(\theta_0 \left(\frac{1}{2} - N \right) + \frac{\pi}{4} \right). \quad (3.55)$$

Note that this expression has, however, $N + 2$ zeros as a function of h_x : N zeros arise from the vanishing of the high frequency sine at fields given by

$$h_x^{(n)} = \pm 2\sqrt{J_x|J_z|} \cos\left(\frac{\lfloor N/2 \rfloor + \frac{1}{4} - n}{N - \frac{1}{2}}\pi\right), \quad (3.56)$$

with $n = 1, \dots, \lfloor N/2 \rfloor$. Two further zeros are due to the vanishing of $\sin \theta_0$. Those reproduce correctly the pair of largest field zeros, $h_x = \pm 2\sqrt{J_x|J_z|}$, which we have already identified above. The two zeros $h_x^{(n)}$ with $n = \lfloor N/2 \rfloor$ are instead artefacts that are introduced by approximating the numerator in the integrand with its value at $r = r_0$. This approximation is not controlled in that field regime since there one has $\theta_0 = O(1/N)$. These two zeros thus have to be discarded, and we are left with N zeros, as it should be.

In Fig. 3.5 we compare the asymptotic Eq. (3.55) with the exact polynomial for t_N obtained from explicitly solving Eqs. (3.45, 3.46). The agreement is very good even for moderate N , and it further improves with system size.

It is easy to extract from the explicit result of Eq. (3.55) and directly visible from Fig. 3.5 that the tunneling grows linearly with a small deviation of the transverse field from an exact zero (3.56), namely:

$$\begin{aligned} t_N(h_x = h_x^{(n)} + \delta h_x) &\approx \delta h_x \frac{\partial t_N}{\partial h_x} \\ &\approx \delta h_x \frac{N^{-\frac{1}{2}}(J_x/J_z)^{\frac{N-1}{2}}}{\left[1 - \left(\frac{h_x^{(n)}}{2\sqrt{J_x|J_z|}}\right)\right]^{1/4}}. \end{aligned} \quad (3.57)$$

3.4.2 Open Ising spin chains In open chains, connected, flipped clusters that touch an end of the chain create only one domain wall. Accordingly, their excitation energy is only $2|J_z|$, half that of a bulk cluster. We define d_l as the intermediate tunneling coefficient associated to such an edge cluster of size l , while c_l is again that associated to bulk clusters. These coefficients satisfy similar recursion relations as before. The one for c_l is unchanged, while for d_l one finds

$$d_l = \frac{h_x}{2|J_z|} \sum_{n=0}^{l-1} d_n c_{l-n-1} - \frac{J_x}{2|J_z|} \sum_{n=0}^{l-2} d_n c_{l-n-2}, \quad (3.58)$$

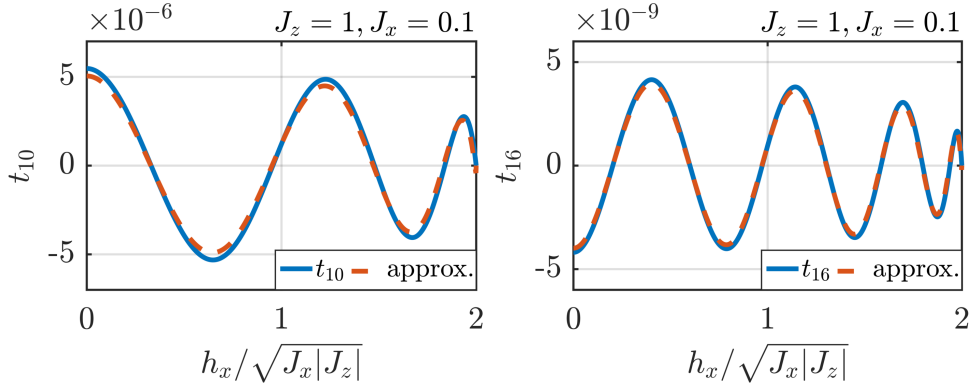


Figure 3.5: Comparison of the exact tunneling polynomial of a ring of spins with the asymptotic expression of Eq. (3.55), for $N = 10$ on the left and $N = 16$ on the right. The exact t_N is obtained by explicitly solving the recursion relations in Eqs. (3.45, 3.46). The asymptotic expression approximates the exact polynomial better and better as the system size increases.

where we again defined $c_0 \equiv 1$ and $d_0 \equiv 1$. The fully flipped state can only be created from edge clusters. We thus have

$$t_N = -h_x \sum_{n=0}^{N-1} d_n d_{l-n-1} + J_x \sum_{n=0}^{N-2} d_n d_{l-n-2}. \quad (3.59)$$

To proceed we again use the previously defined generating function $C(z)$ and define

$$D(z) = \sum_{l=0}^{\infty} z^l d_l, \quad \hat{T}(z) = \sum_{l=1}^{\infty} z^l t_l. \quad (3.60)$$

Again, multiplying the recursion relations by z^l , summing over l , and solving for $\hat{T}(z)$, we obtain

$$\hat{T}(z) = |J_z| \frac{z(z - h_x/J_x)}{(z - z_+)(z - z_-)}, \quad (3.61)$$

where the singularities z_{\pm} are still given by Eq. (3.49). However, here they appear as poles of $\hat{T}(z)$, not as branch points. In this case, the contour integral around $z = 0$ can be transformed into a simple contour around the two poles,

which yields the exact result for t_N as a sum of two residues:

$$\begin{aligned}
 t_N &= \text{Res}_{z=0} \left(\frac{\hat{T}(z)}{z^{N+1}} \right) = -\text{Res}_{z=z_+} \left(\frac{\hat{T}(z)}{z^{N+1}} \right) - \text{Res}_{z=z_-} \left(\frac{\hat{T}(z)}{z^{N+1}} \right) \\
 &= \frac{|J_z|}{(z_+ - z_-)} \left(\frac{z_-}{z_+^N} - \frac{z_+}{z_-^N} \right) \\
 &= \begin{cases} \sim -|J_z| \left(\frac{h_x}{|J_z|} \right)^N, & \frac{h_x^2}{4|J_z|} \gg J_x, \\ -|J_z|(N+1) \left(\frac{h_x}{2|J_z|} \right)^N, & \frac{h_x^2}{4|J_z|} = J_x, \\ -|J_z| \left(\frac{J_x}{|J_z|} \right)^{N/2} \frac{\sin[(N+1)\theta_0]}{\sin(\theta_0)}, & \frac{h_x^2}{4|J_z|} < J_x. \end{cases} \quad (3.62)
 \end{aligned}$$

Like for the closed chain, t_N oscillates when $h_x^2 < 4J_x|J_z|$. The high frequency sine function in the oscillatory regime has $N+2$ zeros, but when $h_x^2 = 4J_x|J_z|$ the denominator vanishes too, and t_N does not vanish. We are thus left with N zeros at the fields

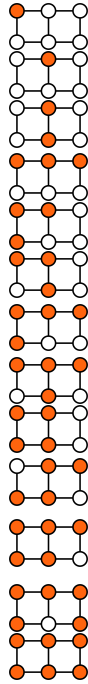
$$h_x^{(n)} = \pm 2\sqrt{J_x|J_z|} \cos \left(\frac{\lfloor N/2 \rfloor + 1 - n}{N+1} \pi \right), \quad (3.63)$$

with $n = 1, \dots, \lfloor N/2 \rfloor$.

Upon comparing the position of the zeros for open boundary conditions, Eq. (3.63), with those for periodic boundary conditions, Eq. (3.56), one finds that closing the chain shifts all fields $h_x^{(n)}$ to higher values. This is expected since a closed chain contains one more bond J_x , so that h_x must slightly increase to compensate the increased exchange contribution to the tunneling.

3.5 2D and 3D clusters While in 1D chains connected clusters only come in one shape (a connected stretch of spins), the length and position (edge or bulk) being their only characteristics, in quasi 1D and in higher dimensions there are many more shapes of clusters we have to consider. Finding a general solution for the tunneling of any N -sized cluster therefore does not seem possible. However, we will calculate the polynomial $t_N(h_x, J_x)$ for small spin clusters to demonstrate the method and to show that the number of zeros still equals the number of spins N .

We first consider the model of Eq. (3.7) on a 3×2 cluster of spins with open boundary conditions, the smallest non-trivial 2D cluster. Besides the fully flipped cluster there are 14 inequivalent connected clusters, cf. Table 3.1 for which we have to compute the intermediate tunneling coefficients. The 3×2 cluster differs from a ring of 6 spins only by one additional bond. By show-



$$\begin{aligned}
 c_{1,1} &= \frac{h_x}{4|J_z|} & c_{2,1} &= \frac{h_x(c_{1,1}+c_{1,2})-J_x}{6|J_z|} \\
 c_{1,2} &= \frac{h_x}{6|J_z|} & c_{2,2} &= \frac{h_x(2c_{1,1})-J_x}{4|J_z|} \\
 c_{2,3} &= \frac{h_x(2c_{1,2})-J_x}{8|J_z|} \\
 c_{3,1} &= \frac{h_x(2c_{2,1}+c_{1,1}^2)-J_x(2c_{1,1})}{6|J_z|} \\
 c_{3,2} &= \frac{h_x(c_{2,1}+c_{2,2}+c_{1,1}c_{1,2})-J_x(c_{1,1}+c_{1,2})}{6|J_z|} \\
 c_{3,3} &= \frac{h_x(c_{2,1}+c_{2,3}+c_{1,1}c_{1,2})-J_x(c_{1,1}+c_{1,2})}{8|J_z|} \\
 c_{4,1} &= \frac{h_x(c_{3,1}+c_{3,2}+c_{2,1}c_{1,1}+c_{2,2}c_{1,1})-J_x(c_{2,1}+c_{1,1}^2+c_{2,2})}{6|J_z|} \\
 c_{4,2} &= \frac{h_x(c_{3,1}+2c_{3,3}+c_{1,1}^2c_{1,2})-J_x(2c_{1,1}c_{1,2}+c_{1,1}^2)}{8|J_z|} \\
 c_{4,3} &= \frac{h_x(2c_{3,2}+2c_{3,3})-J_x(2c_{2,1}+c_{2,2}+c_{2,3})}{4|J_z|} \\
 c_{4,4} &= \frac{h_x(2c_{3,3}+2c_{2,1}c_{1,1})-J_x(2c_{2,1}+c_{1,1}^2)}{8|J_z|} \\
 c_{5,1} &= [h_x(c_{4,1}+c_{4,2}+c_{4,3}+c_{4,4}+c_{3,2}c_{1,1}) \\
 &\quad -J_x(c_{3,1}+c_{3,2}+c_{3,3}+c_{2,2}c_{1,1})]/(4|J_z|) \\
 c_{5,2} &= \frac{h_x(2c_{4,1}+c_{2,2}^2+2c_{3,2}c_{1,1})-J_x(2c_{3,2}+2c_{2,2}c_{1,1})}{6|J_z|} \\
 t_{3 \times 2} &= -h_x(4c_{5,1}+2c_{5,2})+J_x(2c_{4,3}+c_{2,2}^2+4c_{4,1})
 \end{aligned}$$

Table 3.1: Inequivalent connected clusters of a rectangular cluster of 6 spins. Filled orange circles represent flipped spins. The intermediate tunneling coefficients satisfy the indicated recursion relations.

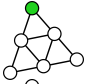
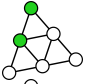
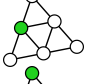
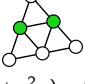
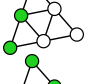
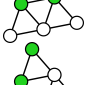
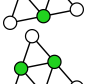
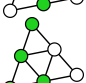
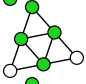
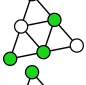
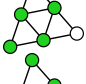
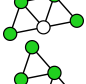
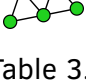
	$c_{1,1} = \frac{h_x}{4 J_z }$		$c_{2,1} = \frac{h_x(c_{1,1}+c_{1,2})-J_x}{8 J_z }$
	$c_{1,2} = \frac{h_x}{8 J_z }$		$c_{2,2} = \frac{h_x(2c_{1,2})-J_x}{12 J_z }$
	$c_{3,1} = \frac{h_x(2c_{2,1}+c_{1,1}^2)-J_x(2c_{1,1})}{8 J_z }$		
	$c_{3,2} = \frac{h_x(2c_{2,1}+c_{2,2})-J_x(c_{1,1}+2c_{1,2})}{8 J_z }$		
	$c_{3,3} = \frac{h_x(c_{2,1}+c_{2,2}+c_{1,1}c_{1,2})-J_x(c_{1,1}+c_{1,2})}{12 J_z }$		
	$c_{3,4} = \frac{h_x(3c_{2,2})-J_x(3c_{1,2})}{12 J_z }$		
	$c_{4,1} = [h_x(c_{3,1} + c_{3,2} + c_{3,3} + c_{2,1}c_{1,1}) - J_x(2c_{2,1} + c_{1,1}c_{1,2} + c_{1,1}c_{1,1})] / (8 J_z)$		
	$c_{4,2} = \frac{h_x(c_{3,2}+2c_{3,3}+c_{3,4})-J_x(2c_{2,1}+2c_{2,2}+c_{1,1}c_{1,2})}{8 J_z }$		
	$c_{4,3} = \frac{h_x(2c_{3,3}+2c_{2,1}c_{1,1})-J_x(2c_{2,1}+c_{1,1}^2)}{12 J_z }$		
	$c_{5,1} = \frac{h_x(2c_{4,1}+2c_{4,2}+c_{4,3})-J_x(2c_{3,2}+2c_{3,3}+c_{3,1}+2c_{2,1}c_{1,1})}{4 J_z }$		
	$c_{5,2} = \frac{h_x(2c_{4,1}+2c_{3,1}c_{1,1}+c_{2,2}^2)-J_x(2c_{3,1}+2c_{2,1}c_{1,1})}{8 J_z }$		
	$t_\Delta = J_x(6c_{4,1} + 3c_{3,1}c_{1,1}) - h_x(3c_{5,1} + 3c_{5,2})$		

Table 3.2: Inequivalent connected clusters of a triangular cluster of 6 spins. Filled green circles represent flipped spins. The intermediate tunneling coefficients satisfy the indicated recursion relations.



$$\begin{aligned}
 c_{1,1} &= \frac{h_x}{6|J_z|} \quad \text{[Diagram: 1 flipped spin]} & c_{2,1} &= \frac{+h_x(2c_{1,1}) - J_x(1)}{8|J_z|} \\
 c_{3,1} &= \frac{h_x(2c_{2,1} + c_{1,1}^2) - J_x(2c_{1,1})}{10|J_z|} \\
 c_{4,1} &= \frac{h_x(4c_{3,1}) - J_x(4c_{2,1})}{8|J_z|} \\
 c_{4,2} &= \frac{h_x(3c_{3,1} + c_{1,1}^3) - J_x(3c_{1,1}^2)}{12|J_z|} \\
 c_{4,3} &= \frac{h_x(2c_{3,1} + 2c_{2,1}c_{1,1}) - J_x(2c_{2,1} + c_{1,1}^2)}{12|J_z|} \\
 c_{5,1} &= \frac{h_x(c_{4,1} + c_{4,2} + 2c_{4,3} + c_{3,1}c_{1,1}) - J_x(3c_{3,1} + 2c_{2,1}c_{1,1})}{10|J_z|} \\
 c_{5,2} &= \frac{h_x(2c_{4,3} + 2c_{3,1}c_{1,1} + c_{2,1}^2) - J_x(2c_{3,1} + 2c_{2,1}c_{1,1})}{14|J_z|} \\
 c_{6,1} &= \frac{h_x(4c_{5,1} + 2c_{5,2}) - J_x(2c_{4,1} + 4c_{4,3} + c_{2,1}^2)}{8|J_z|} \\
 c_{6,2} &= \frac{h_x(2c_{5,1} + 2c_{5,2} + 2c_{4,2}c_{1,1}) - J_x(2c_{4,2} + 4c_{3,1}c_{1,1})}{12|J_z|} \\
 c_{6,3} &= \frac{h_x(6c_{5,2}) - J_x(2c_{4,2} + 4c_{3,1}c_{1,1})}{12|J_z|} \\
 c_{7,1} &= \frac{h_x(3c_{6,1} + 3c_{6,2} + c_{6,3}) - J_x(6c_{5,1} + 3c_{5,2})}{6|J_z|} \\
 t_{2 \times 2 \times 2} &= J_x(12c_{6,1}) - h_x(8c_{7,1})
 \end{aligned}$$

Table 3.3: Inequivalent connected clusters of a cubic cluster of 8 spins. Filled blue circles represent flipped spins. The intermediate tunneling coefficients satisfy the indicated recursion relations.

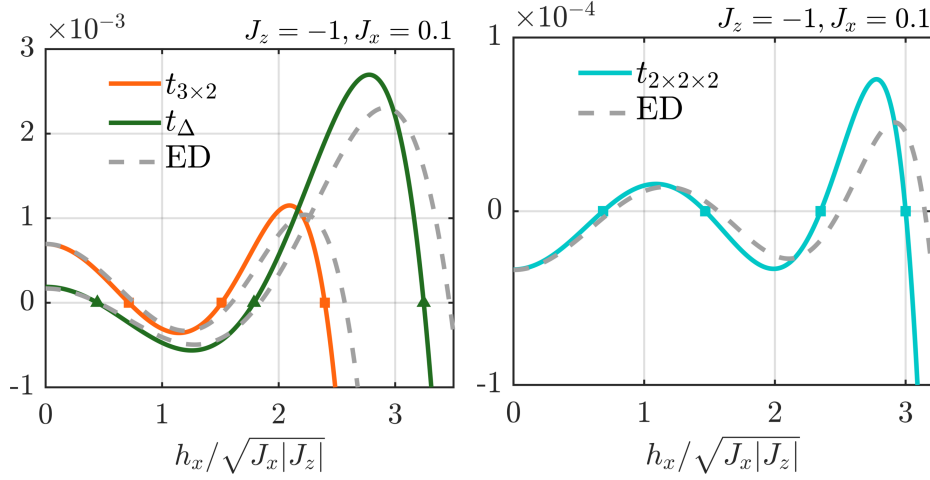


Figure 3.6: The tunneling amplitude t_N for three small, higher-dimensional clusters, as a function of h_x , with the respective zeros marked. All these clusters have N tunneling zeros, and the plot shows the $N/2$ positive ones.

ing that the tunneling polynomial still has N zeros, we thus demonstrate the robustness of the number of zeros to certain perturbations. Upon gradually turning on the bond that transforms the ring into the 3×2 cluster, the zeros move towards higher fields, as one expects. We further derive the tunneling polynomials t_{Δ} for an equilateral triangle made from 6 spins, cf. Table 3.2, and $t_{2 \times 2 \times 2}$ for a cube of 8 spins, cf. Table 3.3.

Solving the resulting recursion relations given in the Tables 3.1, 3.2 and 3.3, we obtain the following polynomials, where we define $x \equiv h_x^2/(J_x |J_z|)$:

$$t_{3 \times 2} = \frac{J_x^3}{|J_z|^2} \left(-\frac{539x^3}{5184} + \frac{511x^2}{576} - \frac{193x}{108} + \frac{25}{36} \right), \quad (3.64)$$

$$t_{\Delta} = \frac{J_x^3}{|J_z|^2} \left(-\frac{65x^3}{2304} + \frac{905x^2}{2304} - \frac{197x}{192} + \frac{3}{16} \right), \quad (3.65)$$

$$t_{2 \times 2 \times 2} = \frac{J_x^4}{|J_z|^3} \left(-\frac{3119x^4}{466560} + \frac{66839x^3}{583200} - \frac{76921x^2}{129600} + \frac{6979x}{7200} - \frac{43}{128} \right), \quad (3.66)$$

which have the expected number of zeros, $N = 6$ or 8 , as one can see in Fig. 3.6.

3.6 Weak Disorder In this section we consider a 1D ring with weak disorder in the transverse fields and in the exchange in the form of

$$h_{x,i} = h_x + \delta h_{x,i}, \quad J_{x,i} = J_x + \delta J_{x,i}, \quad (3.67)$$

where $J_{x,i}$ connects spins i and $i + 1$ and where $J_x > 0$, such that there are zeros in the absence of disorder. We denote the disordered tunneling as \tilde{t}_N , reserving t_N for the tunneling in the disorder free limit. One can in principle determine the recursion relations of such a system and thus study disorder using explicit polynomials \tilde{t}_N . However, we shall rather calculate the relevant average quantities to lowest order in an expansion in $\delta h_{x,i}$ and $\delta J_{x,i}$.

A quantity of particular interest is the typical finite tunneling induced by random fluctuations of the couplings when the average external field is held at one of the tunneling zeros $h_x^{(n)}$. Let us denote the disorder induced tunneling at a zero as

$$T_n \equiv \tilde{t}_N|_{h_x=h_x^{(n)}}. \quad (3.68)$$

We are also interested in how much a ground state crossing shifts due to the presence of randomness:

$$K_n \equiv \tilde{h}_x^{(n)} - h_x^{(n)}, \quad (3.69)$$

where $\tilde{h}_x^{(n)}$ and $h_x^{(n)}$ are respectively the n^{th} zeros of the polynomials \tilde{t}_N and t_N . We can calculate the second moment of these random variables by considering a homogeneous ring where all spins and all bonds are equivalent and where in the absence of disorder all couplings are equal. However, explicit calculations of the second moment of T_n and K_n for open spin chains showed qualitatively very similar behavior as we find below for rings. For a ring, to first order in the perturbations, one has

$$\tilde{t}_N \approx t_N + \frac{1}{N} \frac{\partial t_N}{\partial J_x} \sum_{i=1}^N \delta J_{x,i} + \frac{1}{N} \frac{\partial t_N}{\partial h_x} \sum_{i=1}^N \delta h_{x,i}. \quad (3.70)$$

This follows since perturbations on different sites are equivalent, and thus all partial derivatives are equal:

$$\left. \frac{\partial \tilde{t}_N}{\partial (\delta h_{x,i})} \right|_{\delta J_x = \delta h_x = 0} = \frac{1}{N} \frac{\partial t_N}{\partial h_x}, \quad (3.71)$$

and likewise for the exchange. For identically and independently distributed local disorder, the disorder-induced variance of the tunneling evaluated at a

transverse field zero $h_x^{(n)}$ thus results as

$$\begin{aligned} \langle T_n^2 \rangle &= \frac{\langle \delta J_i^2 \rangle}{N} \left| \frac{\partial t_N}{\partial J_x} \right|_{h_x=h_x^{(n)}}^2 + \frac{\langle \delta h_i^2 \rangle}{N} \left| \frac{\partial t_N}{\partial h_x} \right|_{h_x=h_x^{(n)}}^2 \\ &+ O(\langle \delta J_i^4 \rangle, \langle \delta h_i^4 \rangle). \end{aligned} \quad (3.72)$$

To leading order, the response of the tunneling amplitude T_n to disorder is linear. The shift of the transverse field, K_n , necessary to compensate for this disorder-induced tunneling is then given by the relation

$$T_n + \left. \frac{\partial t_N}{\partial h_x} \right|_{h_x=h_x^{(n)}} K_n = 0. \quad (3.73)$$

From Eqs. (3.72, 3.73), we see that in order to calculate K_n we only need the ratio of the derivatives $\left(\frac{\partial t_N}{\partial J_x} / \frac{\partial t_N}{\partial h_x} \right) \Big|_{h_x=h_x^{(n)}}$. This ratio is easily obtained from the factorized polynomial form of t_N (Eq. (3.31)) as

$$\left(\frac{\partial t_N}{\partial J_x} / \frac{\partial t_N}{\partial h_x} \right) \Big|_{h_x=h_x^{(n)}} = -\frac{h_x^{(n)}}{2J_x}. \quad (3.74)$$

From this we deduce the average mean square of the drift in the zeros to leading order as:

$$\langle K_n^2 \rangle \approx \left(\frac{h_x^{(n)}}{2J_x} \right)^2 \frac{\langle \delta J_{x,i}^2 \rangle}{N} + \frac{\langle \delta h_{x,i}^2 \rangle}{N} \quad (3.75)$$

$$= \frac{1}{N} \left(\frac{h_x^{(n)}}{2} \right)^2 [\langle \mu_i^2 \rangle + 4 \langle \eta_i^2 \rangle], \quad (3.76)$$

where

$$\mu_i \equiv \frac{\delta J_{x,i}}{J_x}, \quad \eta_i \equiv \frac{\delta h_{x,i}}{h_x^{(n)}}, \quad (3.77)$$

quantify the relative fluctuations of the couplings. In many cases these are the most appropriate measures of the disorder strength. We see that the zeros corresponding to larger fields are more strongly affected by disorder. This certainly holds as long as the shifts are smaller than the typical spacing $O(1/N)$ between zeros.

One can obtain the standard deviation of the tunneling amplitude from Eqs. (3.73, 3.76), using the derivative $\frac{\partial t_N}{\partial h_x}$ from Eq. (3.57) for a ring, from

which we get

$$\langle T_n^2 \rangle \approx \frac{1}{2\pi} \left(\frac{J_x}{|J_z|} \right)^{N-1} \frac{\left(h_x^{(n)} \right)^2 [\langle \mu_i^2 \rangle + 4 \langle \eta_i^2 \rangle]}{\left[1 - \left(\frac{h_x^{(n)}}{2\sqrt{J_x|J_z|}} \right)^2 \right]^{1/2}}. \quad (3.78)$$

Again, we see that $T_n \sim h_x^{(n)}$ for small transverse field, while it grows quickly as the largest zero $h_x^{([N/2])} = 2\sqrt{J_x|J_z|}$ is approached.

3.7 Tunneling in single spin models Here we consider the single spin models as presented in Sec. 3.2.4. Similarly to an Ising ferromagnet, the unperturbed ($\lambda = 0$) ground states correspond to the two states with $S_z = \pm S$. Applying our method to this Hamiltonian is rather straightforward: We simply calculate the tunneling matrix element from $-S$ to the $+S$ ground state to lowest order in λ , using intermediate tunneling coefficients c_m , where m refers to the spin projection onto the z -axis, with eigenstates defined by

$$S_z |m\rangle = m |m\rangle. \quad (3.79)$$

If we use the Hamiltonian in the form of Eq. (3.12), the recursion for c_m will involve both c_{m-1} and c_{m-2} , but unlike in the problem treated in Sec. 3.3.1, the matrix elements and the denominators involved in the recursion depend themselves non-trivially on m . The resulting recursion is hard to solve analytically. We can, however, simplify the recursion greatly by first performing a rotation in the $x - z$ plane:

$$\begin{aligned} S_x &= \cos \alpha S'_x + \sin \alpha S'_z, \\ S_z &= \cos \alpha S'_z - \sin \alpha S'_x, \\ S_y &= S'_y, \end{aligned} \quad (3.80)$$

where we choose α to satisfy $\tan^2 \alpha = \lambda^2 J_x / |J_z|$, such as to kill the matrix elements $\langle k | H | k-2 \rangle$ between S'_z -eigenstates, $S'_z |k\rangle = k |k\rangle$. This yields the Hamiltonian in the rotated basis

$$\begin{aligned} H' &= (J_z + \lambda^2 J_x) S_z'^2 + \lambda \sqrt{J_x |J_z|} (S'_z S'_x + S'_x S'_z) \\ &\quad - \lambda h_x \left(\sqrt{\frac{|J_z|}{\lambda^2 J_x + |J_z|}} S'_x + \sqrt{\frac{\lambda^2 J_x}{\lambda^2 J_x + |J_z|}} S'_z \right) - \lambda h_y S'_y. \end{aligned} \quad (3.81)$$

where we consider dominant the ferromagnetic Ising coupling $J_z < 0$. In the perturbative regime, the rotation angle α is small and the ground states of H' still have a large overlap with the two S'_z eigenstates $|\pm S\rangle$. We now deal with the problem of calculating the tunneling

$$\langle S|H'| - S\rangle = t_{2S}\lambda^{2S} + O(\lambda^{2S+1}) \quad (3.82)$$

between these two states up to order λ^{2S} . Since the matrix form of H in the S'_z basis is tridiagonal, only the off-diagonal terms proportional to λ contribute to t_{2S} . Thus we write the Hamiltonian in the form

$$H' = H'_0 + \lambda V'_1 + O(\lambda^2), \quad (3.83)$$

where

$$H'_0 = J_z S_z'^2, \quad (3.84)$$

$$V'_1 = \sqrt{J_x|J_z|}(S'_z S'_x + S'_x S'_z) - h_x S'_x - h_y S'_y. \quad (3.85)$$

The matrix elements of these operators are

$$\langle k|H'_0|k\rangle = J_z k^2, \quad (3.86)$$

$$\frac{\langle k|V'_1|k-1\rangle}{\langle k|S_x|k-1\rangle} = \sqrt{J_x|J_z|}(2k-1) - (h_x - ih_y), \quad (3.87)$$

where we used $\langle k|S_x|k-1\rangle = -i\langle k|S_y|k-1\rangle$, and

$$\langle k|S_x|k-1\rangle = 1/2\sqrt{S(S+1) - k(k-1)}. \quad (3.88)$$

Now that the Hamiltonian is tridiagonal, there is a single tunneling path between $|\pm S\rangle$ of order λ^{2S} . Its contribution to t_{2S} is just the product of all off-diagonal matrix elements $\langle k|V'_1|k-1\rangle$ divided by (minus) the energies of all

intermediate excited states. The total tunneling amplitude is

$$\begin{aligned}
 t_{2S} &= \frac{\prod_{k=-S+1}^S \langle k|V'_1|k-1\rangle}{\prod_{k=-S+1}^{S-1} [\langle S|H'_0|S\rangle - \langle k|H'_0|k\rangle]} \\
 &= \frac{\prod_{k=-S+1}^S \left[\sqrt{J_x|J_z|}(2k-1) - (h_x - ih_y) \right] \langle k|S_x|k-1\rangle}{\prod_{k=-S+1}^{S-1} J_z(S^2 - k^2)}.
 \end{aligned} \tag{3.89}$$

Note that this already takes the form of a factorized polynomial, with zeros given by the equation

$$h_x - ih_y = \sqrt{J_x|J_z|}(2n-1), \tag{3.90}$$

where $n = -S+1, -S+2, \dots, S$. Recall that we took the x -axis to be the hard axis ($J_x > 0$). We find $2S$ equally spaced ground state crossings for $h_y = 0$ and transverse fields

$$h_x^{(n)} = \sqrt{J_x|J_z|}(2n-1). \tag{3.91}$$

This is the same qualitative behavior as in a ferromagnetic Ising cluster as seen in Sec. 3.2.3, cf. Eqs. (3.39, 3.40). This result coincides in lowest order with the zero positions as calculated by A. Garg [84] and as demonstrated experimentally by Wernsdorfer [83]. However, in the rotated frame it becomes quite simple to obtain the exact degeneracies of this model, as we show in the next subsection.

3.7.1 Exact degeneracies of single spin model If we are only interested in the location of the zeros, the rotated Hamiltonian can be used beyond perturbation theory to determine the position of the zeros exactly. Indeed, a zero of the tunneling matrix element $\langle S|H'| - S\rangle$ occurs whenever one of the off-diagonal entries of H' becomes zero. At that point, the Hamiltonian splits into two uncoupled blocks for $S_z \geq k$ and $S_z \leq k-1$, implying that the up-state is strictly decoupled from the down-state to all orders. This entails an exact double degeneracy of the ground state (which map onto each other upon rotation by π around the x -axis). Now, the off-diagonal matrix element is given

by

$$\frac{\langle k|H'|k-1\rangle}{\langle k|S_x|k-1\rangle} = \sqrt{J_x|J_z|}(2k-1) - \left(h_x \sqrt{\frac{|J_z|}{J_x + |J_z|}} - i h_y \right). \quad (3.92)$$

Since $J_x > 0$, we can again have a ground state degeneracy only for a transverse field along x . The critical fields are determined by the exact condition

$$h_x^{(k)} = \sqrt{J_x(J_x + |J_z|)}(2k-1), \quad (3.93)$$

which agrees with the perturbative result of Eq. (3.91) to lowest order in J_x , and reproduces the non-perturbative path integral results by Garg [84]. Here we have shown that this yields the location of the zeros exactly, independently of the size S of the spin. An equivalent but more general and slightly more rigorous proof of this result is given in Sec. 3.C.

The result that the transverse field has to be applied along the hard axis is fully consistent with what we found for FM spin clusters in Sec. 3.2.3. The main difference between the exact cluster calculation and the single spin model consists, however, in the precise location of the zeros. For the single spin model, the zeros are equally spaced, while for clusters they are spaced more and more densely the larger the transverse field, as one can see, e.g. in Fig. 3.5, or read off from the analytical result in Eq. (3.56).

3.8 Other systems with competing tunneling channels The mechanism we have studied here, namely the interference of parallel multi-step tunneling channels between an initial and a final state is very general in nature and appears in various physical contexts.

A famous example is the case of resonant single-particle tunneling via several intermediate sites, a problem introduced by Nguyen, Spivak and Shklovskii [117, 118], with comprehensive reviews given in Refs. [119, 120].

For free particles (non-interacting fermions), different paths from an initial to a final site contribute with an amplitude whose sign alternates with the number of intermediate sites whose energy is above the chemical potential. This leads to negative interference between alternative paths. A magnetic field introduces additional Aharonov-Bohm phases and decreases the likelihood of full negative interference, resulting in increased transmission, that is, negative magnetoresistance [121, 122]. Recently, it was found that the equivalent question for hard core interacting bosons leads to a similar interference problem, where, however, at energies close to the chemical potential all path amplitudes contribute with the same sign, leading to maximally

constructive interference [123, 124]. This situation resembles that of a ferromagnetic cluster with transverse field applied in the direction in which the transverse exchange is more ferromagnetic (i.e., the softer axis). In contrast to the magnetic clusters, however, in these hopping problems it is very hard or even impossible to tune a parameter (e.g., the magnetic field or the chemical potential) to suppress the tunneling completely.

Competing tunneling terms also arise in more general magnetic clusters composed of electronic and nuclear spins, a situation that frequently occurs in rare earth compounds. The magnetic ions are coupled to their nuclear spins, while the electronic spins couple to each other via dipolar and/or exchange couplings. Clusters of such ions often have doubly degenerate ground or excited states, which are only split by higher order tunneling processes that involve the interference of transverse fields, exchange/dipolar interactions and hyperfine couplings, that generically contribute with competing signs. Tuning the transverse field often allows to induce zeros in the corresponding collective tunneling. Similarly, the tunneling of the spin associated with a crystal field doublet of a magnetic ion can under certain circumstances be suppressed by a transverse field applied at specific angles, if different channels involving the magnetic field and transverse crystal field terms compete.

Ground state crossings have also been reported in SU(2) invariant, gapped frustrated spin chains [125, 126]. In that case, the crossings are related to the interaction between the edge states of the chain. This is reminiscent of the explanation of the level crossings in the model of Eq. (3.7) in terms of Majorana edge states [80], and it is natural to ask whether these crossings can also be seen as a consequence of destructive interferences between different channels. For that purpose, let us consider the level crossings in the bilinear-biquadratic spin-1 chain [126], $H = \sum_i J_1(S_i \cdot S_{i+1}) + J_b(S_i \cdot S_{i+2})^2$. If one adds a strong uniaxial anisotropy along z , one may work with respect to an AFM ground state, and the transverse terms with $\Delta S_z = 2$ and 4 have competing signs if $J_b > 0$, presumably leading to level crossings similar to those of the isotropic case. It would be interesting to see if a more direct connection can be established by studying the effective coupling between the edge states starting from the AKLT model $J_b = J_1/3$ for which the edge states are fully decoupled in the ground state [20]. This goes beyond the scope of the present work, however.

3.9 Summary and outlook High order degenerate perturbation theory allows us to understand transverse field zeros in terms of negatively interfering tunneling paths, which in turn is tied to the presence of competing quantum

fluctuations in the Hamiltonian. Our method nicely applies to 1D systems, where the tunneling can be obtained for any system size exactly, in contrast with 2D and 3D clusters where the number of different connected clusters grows exponentially with system size. Overall, the results support the existence of N zeros in some region of the parameter space independently of the geometry.

The original model (Eq. (3.7)) can be further extended by staggering the field or by adding exchange couplings along the y -axis while keeping the crossings. As we saw in Sec. 3.2.3, systems with FM ground states exhibit zeros only when the field is applied along the "hard axis" (the one with the strongest antiferromagnetic or the weakest ferromagnetic coupling). In contrast, AFM clusters on a bipartite lattice exhibit suppressed tunneling on approximate circles in the transverse field plane. This may make AFM cluster ground states more attractive since the tunneling suppression is more resistant to fluctuations in the orientation of the applied field. This ability to control and suppress the quantum fluctuations in small magnetic clusters or single molecule magnets is indeed considered an important goal [127].

As we showed in Eq. (3.57), the tunneling amplitude scales linearly with generic deviations from a zero condition. This linear behavior contrasts with the scaling one often encounters in situations where tunneling is suppressed (at $h_x = 0$) due to a point group symmetry, e.g., in rare earth non-Kramers doublets such as Ho in LiHoF₄. Here the doublets have no splitting at zero transverse field h_x , but a quadratic splitting $\sim h_x^2$ is induced at small transverse field [128, 129]. The power of h_x with which the tunneling grows depends on the structure of the crystal field levels involved in the non-Kramers doublet. These differences have advantages in different contexts: A linear response in tunneling implies that one needs smaller field deviations to manipulate a classical bit or qubit; quadratic or higher order scaling instead imply better protection from dephasing (of a qubit) due to transverse field noise.

Introducing disorder in the exchange couplings and in the transverse fields, the crossings change position but do not disappear. The latter only happens when in ferromagnets $J_x - J_y$, or in antiferromagnets $J_x + J_y$, starts to change sign and turn negative. The relation between a set of J_x , either randomly generated or carefully chosen, and the resulting number of crossings remains to be studied more deeply.

A certain amount of disorder in the exchange is always to be expected from static sources such as lattice imperfections, strain, or dynamically due to slow phonons. Spatial inhomogeneities can also induce g -factor variations that lead to an effective disorder in the transverse field. In an ensemble of

weakly disordered clusters it is thus impossible to suppress the tunneling simultaneously in all clusters, and even in a single cluster, temporal fluctuations of the parameters will destroy the perfect negative interference of competing tunneling channels. The best strategy to suppress the tunneling as much as possible consists then in tuning the transverse field to the first (smallest) zero, $h_x^{(n=1)}$, corresponding to the average exchange coupling in the system. The disorder-induced fluctuations away from vanishing tunneling turn out to be smallest under those conditions. This is closely related with the fact that the location of this smallest transverse field zero moves the least as the parameters of the Hamiltonian are slightly perturbed. Hence this zero seems to be the most interesting one for most applications.

Our recursive calculation of collective tunneling amplitudes generalizes nicely to simpler single spin models, and the ground state crossings in this model can be interpreted with the same tunneling interference argument. Given the $2S$ crossings of a single spin, one may expect that an appropriately chosen spin- S model on a lattice of N spins will exhibit $2SN$ crossings.

It is an interesting question to ask what happens to the zeros as one leaves the perturbative regime. In the ferromagnetic single spin model we can trace them easily, since we can obtain them exactly. If the hard axis is along the x -axis and one tunes J_y up to and beyond J_z for example, the number of $2S$ zeros remains intact, even though the easy axis has undergone a flop from the z - to the y -axis. In lattice models, the zero lines in the h_x - J_x plane do not seem to disappear either. They even may cross quantum phase transition lines, as long as they enter a new phase with a degenerate ground state or a gapless phase. The study of the related phenomena and implications is left for future work.

3.A Deduction of method Following Bloch's recipe [116] we consider the effective Hamiltonian H_{eff} projected onto the unperturbed ground state subspace $g = \{\emptyset, \Sigma\}$ by the projection operator P . It takes the form

$$H_{\text{eff}} = PHP + P \left(\sum_{n=2}^{\infty} \sum_{\{k_i\}} V S_{k_1} \dots V S_{k_{n-1}} \right) V P, \quad (3.94)$$

where n specifies the order in V of the term. For a given n , we sum over all $(n-1)$ -tuples of $k_i = 0, 1, \dots$ that obey

$$k_1 + k_2 + \dots + k_s \geq s, \quad (3.95)$$

for all $s = 1, \dots, n-2$, and

$$k_1 + k_2 + \dots + k_{n-1} = n - 1. \quad (3.96)$$

The operator S_k is defined as

$$S_k = \begin{cases} -P = -\sum_{m \in g} |m\rangle \langle m|, & k = 0, \\ \frac{1-P}{(\varepsilon_0 - H_0)^k} = \sum_{m \notin g} \frac{|m\rangle \langle m|}{(-\Delta\varepsilon_m)^k}, & k \geq 1, \end{cases} \quad (3.97)$$

where $\Delta\varepsilon_m = \varepsilon_m - \varepsilon_0$. The eigenvalue equations read

$$H_{\text{eff}} P |\Psi_{\pm}\rangle = E_{\pm} P |\Psi_{\pm}\rangle, \quad (3.98)$$

where $|\Psi_{\pm}\rangle$ are the lowest energy eigenstates of H . Due to the symmetry R (Eq. (3.4)) we may write the eigenstate projections to leading order as

$$P |\Psi_{\pm}\rangle = |\emptyset\rangle \pm |\Sigma\rangle + O(\lambda). \quad (3.99)$$

The relevant matrix element to calculate is

$$t \equiv \langle \emptyset | H_{\text{eff}} | \Sigma \rangle. \quad (3.100)$$

Upon expanding $V = \lambda V_1 + \lambda^2 V_2$ in Eq. (3.94) and substituting in t , we group terms according to their powers of λ . Taking n_1 (n_2) to be the number of V_1 (V_2) operators present in a term of orders n and u , we have

$$n_1 + n_2 = n, \quad n_1 + 2n_2 = u, \quad (3.101)$$

from which we find what orders of n contribute to u by taking the limiting cases of $n_1 = \text{mod}(u, 2)$ and $n_2 = 0$. Finally, we only need to sum over the permutations of V_1 and V_2 that respect the order u . Applying this to t , we have

$$t = \sum_{u=1}^{\infty} \lambda^u \sum_{n=\lceil \frac{u}{2} \rceil}^u \sum_{\{k_i\}, \{l_i\}} \langle \emptyset | V_{l_1} S_{k_1} \dots V_{l_{n-1}} S_{k_{n-1}} V_{l_n} | \Sigma \rangle, \quad (3.102)$$

where the $l_i = 1, 2$ obey $l_1 + l_2 + \dots + l_n = N$. It helps to look at the calculation of the matrix element in Eq. (3.102) sequentially; that is, starting with the extreme left operator, we apply each operator to the states on its left. While V_1 and V_2 always transform the states $\langle m|$ they act on, S_k mainly acts as a projector onto a subspace of states, either the ground state g (if $k = 0$), or the excited states (if $k > 0$). Now, the treatment of V_2 as a second order perturbation is crucial for our method and physically justified by the fact that

the basic action of V_2 on $|m\rangle$ is to flip pairs of neighboring spins while V_1 flips single spins. In the term of order λ^u , $\langle\emptyset|$ is acted on with enough V_1 's and V_2 's to at most flip u spins. Since we need a minimum of N spin flips to transform \emptyset into Σ , it follows that the lowest order is λ^N . After applying a V_l to the states on its left, the resulting states must have l more spin(s) flipped than before for such terms to yield a non-zero contribution to order λ^N . In particular, this means a projection onto g by $S_0 = -P$ would only give terms that will eventually have zero contribution. This imposes $k_i > 0$ in the leading term $O(\lambda^N)$. However, the constraint (3.96) only allows for one single choice of the k_i , namely, $k_i = 1$ for all i . Using this information in Eq. (3.102), and writing $t = t_N \lambda^N + O(\lambda^{N+1})$, we now have

$$t_N = \sum_{n=\lceil \frac{N}{2} \rceil}^N \sum_{\{l_i\}} \langle\emptyset| V_{l_1} S \dots V_{l_{n-1}} S V_{l_n} |\Sigma\rangle \quad (3.103)$$

where $S \equiv S_1$. This proves Eq. (3.20) in the main text.

Now, we shall prove the recursion relations in Eq. (3.28), starting from the definition of the intermediate tunneling coefficients

$$c_m \equiv \sum_{n=\lceil \frac{|m|}{2} \rceil}^{|m|} \sum_{\{l_i\}} \langle\emptyset| V_{l_1} S \dots V_{l_{n-1}} S V_{l_n} S |m\rangle, \quad (3.104)$$

where

$$l_1 + l_2 + \dots + l_n = |m|, \quad (3.105)$$

and we remind the reader that $|m|$ is the number of spins of $|m\rangle$ that are flipped relative to $|\emptyset\rangle$. Summing over l_n and redefining $n \rightarrow n - 1$, we have

$$\begin{aligned} c_m &= \sum_{n=\lceil \frac{|m|}{2} \rceil - 1}^{|m|-1} \sum_{\{l_i\}} \langle\emptyset| V_{l_1} S \dots V_{l_n} S V_{l_{n+1}} S |m\rangle \\ &+ \sum_{n=\lceil \frac{|m|}{2} \rceil - 1}^{|m|-1} \sum_{\{l'_i\}} \langle\emptyset| V_{l'_1} S \dots V_{l'_n} S V_{l'_{n+1}} S |m\rangle, \end{aligned} \quad (3.106)$$

where

$$l_1 + \dots + l_n = |m| - 1, \quad l'_1 + \dots + l'_n = |m| - 2. \quad (3.107)$$

By expanding $V_{1,2} S |m\rangle$ in Eq. (3.106), we shall see that we recover the cluster

coefficients of smaller clusters. Consider first $V_1 S |m\rangle$. We have that

$$S |m\rangle = \frac{1}{-\Delta\epsilon_m} |m\rangle, \quad (3.108)$$

which follows from the definition of S . Then, applying V_1 to the state $|m\rangle$, we get a sum over states m' which differ by one spin flip from m . However, only m' clusters with $|m'| = |m| - 1$ yield a non-zero contribution to c_m . Thus,

$$\begin{aligned} & \sum_{n=\lceil \frac{|m|}{2} \rceil - 1}^{|m|-1} \sum_{\{l_i\}} \langle \emptyset | V_{l_1} S \dots V_{l_n} S V_1 S |m\rangle \\ &= \sum_{n=\lceil \frac{|m|}{2} \rceil - 1}^{|m|-1} \sum_{\{l_i\}} \langle \emptyset | V_{l_1} S \dots V_{l_n} S \sum_{\substack{m' \\ |m'|=|m|-1}} |m'\rangle \langle m' | V_1 S |m\rangle \\ &= \sum_{\substack{m' \\ |m'|=|m|-1}} c_{m'} \langle m' | V_1 S |m\rangle, \end{aligned} \quad (3.109)$$

With an analogous argument applied to $V_2 S |m\rangle$ we obtain the recursion relations (3.24, 3.23) in the main text. The expression for t_N follows from an analogous derivation, the only difference being that there is no insertion of the operator S at the last step, as one can note from comparing Eq. (3.103) and Eq. (3.104). This eliminates the corresponding energy denominator.

3.B Cluster independence Consider a cluster C which is composed of two (dis)connected clusters of flipped spins A and B , by which we mean that the excitation energy of cluster C is the sum of independent excitation energies,

$$\Delta\epsilon_C = \Delta\epsilon_A + \Delta\epsilon_B, \quad (3.110)$$

Given the definition of the intermediate tunneling coefficient $c_{(m)}$ (Eq. (3.22)), we want to prove that

$$c_{(C)} = c_{(A)} c_{(B)}. \quad (3.111)$$

which one should expect to hold because to leading order we can simply reduce the Hamiltonian to the parts acting on either A or B and drop all other terms, so that the flipping of A and B are independent processes.

First, let us write $c_{(m)}$ in terms of matrix elements of V by expanding all operators S (Eq. (3.21)). In this way, $c_{(m)}$ is given by a sum over many chain

products of matrix elements of $V_{1,2}$:

$$\begin{aligned} c_{(m)} &= \sum_{n, \{l\}, \{k\}} \langle \emptyset | V_{l_1} \frac{|k_1\rangle \langle k_1|}{-\Delta \varepsilon_{k_1}} V_{l_2} \frac{|k_2\rangle \langle k_2|}{-\Delta \varepsilon_{k_2}} \dots V_{l_n} \frac{|m\rangle}{-\Delta \varepsilon_m} \\ &= \sum_{n, \{l\}, \{k\}} \prod_{i=1}^n \frac{\langle k_{i-1} | V_{l_i} | k_i \rangle}{-\Delta \varepsilon_{k_i}}, \end{aligned} \quad (3.112)$$

with $k_0 \equiv \emptyset$ and $k_n \equiv m$. When summing over the full space of $n, \{l\}, \{k\}$ indices, many combinations will give a zero contribution. Let us consider only the combinations that have a non-zero contribution, and let us denote those by a single index μ . Each μ corresponds to a unique choice of $n, \{l\}, \{k\}$ indices, which we denote as $n_\mu, \{l_\mu\}, \{k_\mu\}$. We may now write

$$c_{(m)} = \sum_{\mu} \prod_{i=1}^{n_\mu} \frac{v_{\mu,i}}{-\Delta \varepsilon_{\mu,i}}, \quad (3.113)$$

where $v_{\mu,i} \equiv \langle k_{\mu,i-1} | V_{l_{\mu,i}} | k_{\mu,i} \rangle$. Each μ corresponds to a unique way or path of flipping the m cluster starting from \emptyset . We can apply this to our clusters of interest, giving

$$c_{(A)} = \sum_{\alpha} \prod_{i=1}^{n_\alpha} \frac{v_{\alpha,i}}{-\Delta \varepsilon_{\alpha,i}}, \quad c_{(B)} = \sum_{\beta} \prod_{j=1}^{n_\beta} \frac{v_{\beta,j}}{-\Delta \varepsilon_{\beta,j}}, \quad (3.114)$$

$$c_{(C)} = \sum_{\gamma} \prod_{k=1}^{n_\gamma} \frac{v_{\gamma,k}}{-\Delta \varepsilon_{\gamma,k}}, \quad (3.115)$$

The important thing to realize here is that each γ , that is, each path from \emptyset to the C cluster, is some combination of a path α and a path β . Vice-versa, if one takes two paths α and β from \emptyset to A and B respectively, then each combination of α and β is a different path from \emptyset to C and will contribute to $c_{(C)}$. It is obvious that any such combination has the same product of V matrix elements, but the energy denominators will not combine so easily. Still, we see already that we can write

$$c_{(C)} = \sum_{\alpha, \beta} \Omega(n_\alpha, n_\beta) \prod_{i=1}^{n_\alpha} v_{\alpha,i} \prod_{j=1}^{n_\beta} v_{\beta,j}, \quad (3.116)$$

where $\Omega(n_\alpha, n_\beta)$ involves calculating the chain product of energy denominators for each combination of α and β and summing over all combinations. To be more clear, let us define $\Omega(n_\alpha, n_\beta)$ analytically. Creating the combinations

of α and β can be seen as the problem of choosing n_α out of $n_\alpha + n_\beta$ objects, with a total of $(n_\alpha + n_\beta)!/n_\alpha!/n_\beta!$ possible combinations. We specify a combination in terms of variables $\sigma_i = 0, 1$ with $i = 1, 2, \dots, n_\alpha + n_\beta$, where σ_i indicates if the object i has been chosen or not. To have a valid combination, we must limit ourselves to sequences of σ_i where n_α objects have been chosen. Then, we write

$$\Omega(n_\alpha, n_\beta) = \sum_{\sigma_1=0}^1 \sum_{\sigma_2=0}^1 \cdots \sum_{\sigma_{n_\alpha+n_\beta}=0}^1 \delta \left(n_\alpha, \sum_{i=1}^{n_\alpha+n_\beta} \sigma_i \right) \times \prod_{k=1}^{n_\alpha+n_\beta} \frac{-1}{\Delta \varepsilon_{\alpha, \sum_{i=1}^k \sigma_i} + \Delta \varepsilon_{\beta, \sum_{i=1}^k (1-\sigma_i)}}, \quad (3.117)$$

where $\delta(a, b)$ is the Kronecker delta and we define $\Delta \varepsilon_{\alpha,0} = 0$ and $\Delta \varepsilon_{\beta,0} = 0$. Here we have used the independence between clusters to write the excitation energy as the sum of the excitation energies at A and B . Ω is to be seen more generally as a function of two integers, $\Omega(u, v)$, obeying $0 \leq u \leq n_\alpha$ and $0 \leq v \leq n_\beta$. Expanding the sum over σ_{u+v} in $\Omega(u, v)$, one can show that

$$\Omega(u, v) = \frac{-1}{\Delta \varepsilon_{\alpha,u} + \Delta \varepsilon_{\beta,v}} [\Omega(u, v-1) + \Omega(u-1, v)], \quad (3.118)$$

very much related to how one can calculate combinations recursively which gives rise to Pascal's triangle. With these new definitions, we set ourselves to prove Eq. (3.111), which is now equivalent to

$$\Omega(n_\alpha, n_\beta) = \prod_{i=1}^{n_\alpha} \frac{-1}{\Delta \varepsilon_{\alpha,i}} \prod_{j=1}^{n_\beta} \frac{-1}{\Delta \varepsilon_{\beta,j}} = \Omega(n_\alpha, 0) \Omega(0, n_\beta). \quad (3.119)$$

We shall prove the more general statement

$$\Omega(u, v) = \Omega(u, 0) \Omega(0, v) \quad (3.120)$$

recursively. First, let us assume that

$$\Omega(u-1, v) = \Omega(u-1, 0) \Omega(0, v), \quad (3.121)$$

$$\Omega(u, v-1) = \Omega(u, 0) \Omega(0, v-1). \quad (3.122)$$

Using these assumptions on Eq. (3.119), we easily obtain Eq. (3.120). The initial equations of the recursion are straightforwardly true, if one just defines $\Omega(0, 0) \equiv 1$, thus the cluster independence is proven.

3.C General derivation of zeros in single spin model We consider the most general quadratic single spin model with anisotropy and a transverse field. Upon choosing axes that bring the quadratic part to a diagonal form and choosing the easy axis to be along z ($J_x, J_y \geq J_z$), we have the most general form

$$H = +J_z S_z^2 + J_x S_x^2 + J_y S_y^2 - h_x S_x - h_y S_y. \quad (3.123)$$

Here we changed the sign of J_z with respect to previous Hamiltonians for ease of notation. Also note that one can further simplify the Hamiltonian by subtracting a constant $J\vec{S}\cdot\vec{S} = JS(S+1)I$ term and choosing $J = J_i$ so that we remove one of the second order couplings, showing that we only need 2 second order couplings to have the most general Hamiltonian. We also choose $J_x \geq J_y \geq J_z$, which can always be accomplished by an exchange of the x and y axes. We will see that we obtain zeros only if the transverse field is parallel to the hard axis, i.e. $h_y = 0$. Let us choose then $h_y = 0$. In that case the Hamiltonian has the symmetry

$$R \equiv \exp(i\pi S_x), \quad [H, R] = 0, \quad (3.124)$$

or in other words, H is invariant under $S_{y,z} \rightarrow -S_{y,z}$. Let us now analyze the Hamiltonian as a matrix in the S_z basis: It is pentadiagonal with non-zero $\langle m|S_z|m'\rangle$ matrix elements when $|m - m'| \leq 2$. However, we can reduce the Hamiltonian to a tridiagonal form by rotating the quantization axis around the y axis by an angle α (Eq. (3.80)). The part of the rotated Hamiltonian that potentially has matrix elements between S'_z eigenstates with $m' = m \pm 2$ results as

$$H'_2 = [J_x - (J_x + J_z) \sin^2(\alpha)](S'_x)^2 + J_y(S'_y)^2 \quad (3.125)$$

If we impose $\langle m|H'_2|m-2\rangle$ and solve for α , we obtain

$$\sin^2(\alpha) = \frac{J_x - J_y}{J_x - J_z}, \quad (3.126)$$

and the condition that $1 \geq \sin^2(\alpha) \geq 0$ gives exactly $J_x \geq J_y \geq J_z$, which is what we assumed to begin with. With the above choice of the rotation angle α , we reduce H' to be tridiagonal. If in addition, it happens that one of the off-diagonal elements vanishes,

$$\langle m|H'|m-1\rangle = 0, \quad (3.127)$$

H' takes a block diagonal form, and the projector on $S'_z \geq m^*$,

$$P_{m^*} = \sum_{m=m^*}^S |m\rangle \langle m|, \quad (3.128)$$

commutes with H' , $[H', P_{m^*}] = 0$. Since, however, P_{m^*} does not commute with the symmetry R , the condition (3.127) necessarily implies the presence of degeneracies in the spectrum. Let us now argue that the ground state is exactly degenerate. The ground state $|\Psi_0\rangle$ can be chosen to be an eigenstate of P_{m^*} . It certainly has a non-zero overlap with one of the low energy states $S'_z = \pm S$ or more generally, with some of the states $S'_z = m$ with $|m| \geq |m^*|$. Upon acting with the unitary R on this state one obtains a new ground state, that has a significant overlap with the opposite low energy states $S'_z = \mp S$ (or more generally, $S'_z = -m$) that lies outside the eigenspace of P_{m^*} to which $|\Psi_0\rangle$ belongs. Thus, $R|\Psi_0\rangle$ is linearly independent of $|\Psi_0\rangle$, implying the exact degeneracy of the ground state, and thus vanishing of the tunneling.

Let us now analyze when the condition (3.127) is satisfied. After the rotation by an angle given by Eq. (3.126), the off-diagonal part of the rotated Hamiltonian H' reads

$$H'_1 = (J_x - J_z) \cos(\alpha) \sin(\alpha) (S'_z S'_x + S'_x S'_z) - h_x \cos(\alpha) S'_x. \quad (3.129)$$

Its matrix element between m^* and $m^* - 1$ vanishes if and only if

$$h_x = \pm \sqrt{(J_x - J_y)(J_z + J_x)(2m^* - 1)}. \quad (3.130)$$

There are thus exactly $2S$ equidistant zeros of the tunnel splitting. This statement is entirely independent of the size of the spin, or the couplings, as long as they satisfy $J_x \geq J_y \geq J_z$.

Chapter 4

Conformal and chiral phase transitions in Rydberg chains

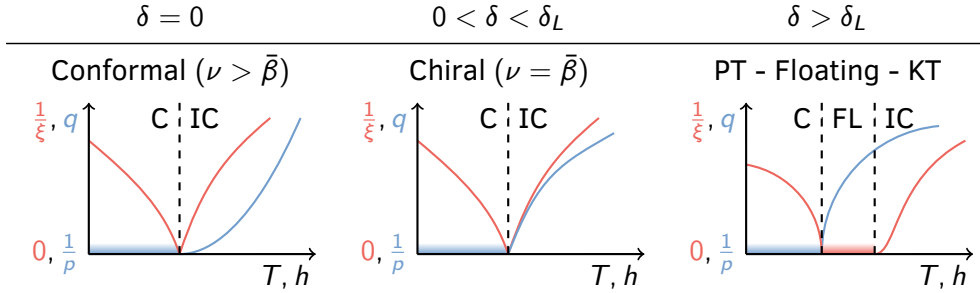
The work in this chapter was done in collaboration with Natalia Chepiga and my supervisor Frédéric Mila. It was published in pre-print in 2022 [3] and is under peer review for publication in PRL. The same results are presented here but the discussion is restructured to fit with the long format of the thesis. The chapter is structured as follows: In the introductory section, we discuss the problem of incommensurate-commensurate phase transitions in the context of the Rydberg experiments, and we overview some of our results on the Rydberg model in the phase diagram shown in Fig. 4.1. A complementary section describing the DMRG algorithm was added, followed by implementation details specific to our problem. We then present our DMRG results. Finally, we discuss these results in the context of previous numerical and experimental work.

4.1 Commensurate-Incommensurate transitions

4.1.1 Chiral clock models In recent experiments on chains of Rydberg atoms with programmable interactions [75, 76], quantum phase transitions between commensurate (C) ordered phases of periods $p = 2, 3, 4$ and an incommensurate (IC) disordered phase were probed dynamically using the quantum Kibble-Zurek mechanism [130, 131, 132]. These experiments have renewed the interest in the problem of IC-C transitions first studied in the 80's and 90's in the context of adsorbed monolayers [133, 134]. The IC-C critical behavior of a minimal model introduced to describe such transitions, the p -state chiral clock model [135, 136] (CCM), contains most of the relevant physics. The IC-C transition of CCMs with $p \geq 5$ happens through an intermediate gapless phase of central charge $c = 1$ characterized by incommensurate correlations. The dominant wave-vector q is not frozen to any specific value but changes continuously (floats) through the phase, therefore referred to as a *floating* phase [137, 138, 135]. The disorder to floating (FL) transition is in

the Kosterlitz-Thouless (KT) universality class [17], with exponentially diverging correlation length ξ . One reaches the ordered phase through a Pokrovsky-Talapov [139] (PT) transition where the wave-vector q (which we define in units of 2π) goes to $1/p$ as a power-law with the exponent $\bar{\beta} = 1/2 = \nu'$.

The $p = 2$ CCM does not allow chirality and is instead an Ising-like Hamiltonian, thus one expects such an universality class ($\nu = 1$) if the transition is continuous. The most interesting cases are $p = 3$ and 4, where the IC-C transition may be direct. In particular, if the chiral perturbation δ is relevant, it was suggested [77] that the IC-C transition may still be direct but in a new non-conformal (*chiral*) universality class characterized by $\nu = \bar{\beta}$, at least up to a Lifshitz point δ_L beyond which the chiral perturbation becomes large enough for an intermediate floating phase to appear. The direct transition can in any case only be conformal at a single point, the point where the chiral perturbation vanishes, as long as the perturbation remains relevant. Discarding possible first-order transitions, as we increase the chiral coupling starting from zero, we might see the following sequence of transitions:



The middle case might not happen, in which case there is no Lifshitz point ($\delta_L = 0$) and we transition directly to an intermediate floating phase. The parameter driving the transition could be the temperature T for classical 2D systems [140] or some coupling h for quantum 1D.

The case of $p = 3$ has been extensively studied [141, 136, 77, 142, 143, 144, 145, 146, 140, 147, 148]. It is known that in this case the chiral perturbation is relevant [143], and the existence of a transition line in the chiral universality class has been well established, with both experiments [133, 134] and recent numerical work [149, 150, 151, 152, 153] supporting it. When $\delta = 0$, the model reduces to the exactly solvable three-state clock (Potts) model [154, 155] with exponents $\nu = 5/6$ and $\bar{\beta} = 5/3$.

On the other hand, the four-state chiral clock model has not received the same level of attention, but it is known that the chiral perturbation is relevant and evidence points to a floating phase appearing immediately when δ

is turned on [135, 144, 156].

4.1.2 The Rydberg model The model which will mostly occupy us until the end of this chapter is the experimentally relevant model of Rydberg atoms [75, 76] on a chain of length L . Each Rydberg atom can be excited to a Rydberg state by an applied laser with Rabi frequency Ω and detuning Δ . Excited Rydberg atoms have long-range interactions between them, while they don't interact in the ground state. We can model the system with a hard-core boson Hamiltonian as such

$$\mathcal{H} = \sum_i -\Delta \hat{n}_i + \Omega \hat{\sigma}_i^x + \sum_{r>0} \frac{\hat{n}_i \hat{n}_{i+r}}{r^6}, \quad (4.1)$$

where $\hat{\sigma}_i^x \equiv \hat{b}_i^\dagger + \hat{b}_i$ and $\hat{n}_i \equiv \hat{b}_i^\dagger \hat{b}_i$. We will use more frequently the units Δ/Ω and $\mathcal{R}_b \equiv \Omega^{-1/6}$ as introduced in Ref. [75]. In the classical limit $\Omega = 0$ of the Rydberg model (Eq. (4.1)), the repulsive interaction and a positive bias Δ will compete to reduce/increase the number of bosons. By adjusting their ratio, a devil's staircase [157, 158] of classical ground states of many different ratios of occupation per unit cell size is generated, with the largest phases having one boson every p sites. One finds such phases of period p when the potential Δ is tuned such that the occupation of sites at distance $p-1$ is prohibited by strong interactions, while bosons at distance p are weakly interacting: $(p-1)^{-6} \gg \Delta \gg p^{-6}$, which is a significant interval because of the rapidly decaying van der Waals potential energy. The p phases are stable when Ω is turned on, up to values of $\Omega \sim \Delta$, beyond which the system becomes disordered and the q-vector incommensurate. However, the q-vector varies continuously throughout the disordered phase, so that $q = 1/p$ equal-q lines exist. These lines intersect their respective ordered phases at a single point (Fig. 4.1), the exception being $p = 2$, where instead the ordered phase is surrounded by a commensurate disordered phase. For $p = 3, 4$, the transition along the equal-q lines seems to be of a conformal nature, as we will try to justify with our results. The same does not seem to be true for $p = 5$, as it is thought that ordered phases of $p \geq 5$ first go through a floating phase before reaching disorder, while floating phases cover only partially the $p = 3, 4$ phases. While the connection with the CCMs suggests itself, it can be made explicit with the introduction of the blockade models.

4.1.3 Blockade models The relation between the $p = 3$ CCM and the Rydberg model is well established through the $r = 2$ *blockade* model [149, 160]. In these models, configurations with bosons at a distance less than r are forbid-

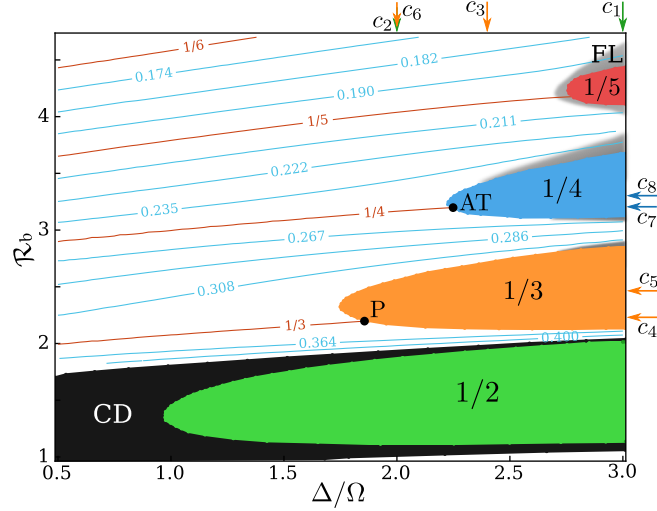


Figure 4.1: Phase diagram of the Rydberg model obtained with DMRG simulations on 121 sites, where $\mathcal{R}_b \equiv \Omega^{-1/6}$. The ordered lobes are found in the intervals $p - 1 \ll \mathcal{R}_b \ll p$. The black region is a commensurate disordered (CD) phase with wave-vector $q = 1/2$ in units of 2π . The grey region is a sketch of the floating phase based on a previous iDMRG work [159] (See Sec. 4.4.9 for details). Note the very narrow floating phases between the $1/3$ and $1/4$ phases. Equal- q lines are shown in the disordered and floating phases. A floating phase is also expected to exist in the lower part of the $1/3$ lobe, however, it will be much thinner than above the lobe [152, 159], and in fact, it is pushed to much larger values of Δ/Ω . The points P and AT are respectively our estimates of the Potts and Ashkin-Teller critical points. Apart from the cuts that go through these points, either horizontally/vertically, or along the associated commensurate lines (P/AT cuts), the other cuts discussed throughout the chapter are horizontal or vertical and are labeled c_n . They are represented by arrows colored according to the ordered phase they cross (c_1 and c_3 cross their respective lobes from below). The following table defines the cuts:

Δ/Ω		Δ/Ω		\mathcal{R}_b		\mathcal{R}_b	
c_1	3	c_3	2.4	c_4	2.225	c_7	3.22
c_2	2	c_6	2	c_5	2.45	c_8	2.32

den, and only the interaction at distance r is kept. We can define such models as

$$\begin{aligned} \frac{\mathcal{H}_r}{\Omega} &= \sum_i -Q \hat{n}_i + \hat{\sigma}_i^x + \left(\frac{\mathcal{R}_b}{r}\right)^6 \hat{n}_i \hat{n}_{i+r}, \\ \hat{n}_i(1 - \hat{n}_i) &= 0, \quad \hat{n}_i \hat{n}_{i+j} = 0 \quad \forall i, \forall j \in \{1, \dots, r-1\}, \end{aligned} \quad (4.2)$$

where we defined $Q \equiv \Delta/\Omega$. We could generate the r blockade model from the Rydberg model by setting $\mathcal{R}_b \approx r$, with $Q \sim 1$, so that the two local terms are of the same order as the interaction term of distance r . Then, considering the power-law exponent ($= 6$) to be very large, interaction terms at distance smaller than r become energetically prohibitive while longer range terms become negligible. Thus the r blockade model is expected to be qualitatively accurate with respect to the Rydberg model in some interval around $\mathcal{R}_b = r$, which is between two consecutive ordered phases of periods $p = r, r + 1$.

The $r = 1$ blockade model is simply an Ising-like Hamiltonian, just like the two-state clock model. The IC-C transition of the $r = 2$ blockade model is in the three-state CCM universality class [149, 150, 152]. In this model, there is an integrable line that crosses the period-3 boundary at a single point where the transition is conformal, a three-state Potts point corresponding to $\delta = 0$. As we move away from this point along the phase boundary, we are necessarily increasing δ . Chiral lines seem to surround the point [149, 150, 152], and further away intermediate floating phases appear. We can expect the same critical behavior in the Rydberg model. While the location of the three-state Potts point on the blockade model is known since it lies on an integrable line, it is not known in the Rydberg model, but we may locate it by following the $q = 1/3$ line since it should intersect the period-3 phase at exactly the conformal point as demonstrated in the blockade model [152].

In the context of Rydberg atoms, the $r = 3$ blockade model has only been introduced very recently [160]. Here, the commensurate line was found to intersect the $p = 4$ phase boundary at a conformal point where the correlation length critical exponent is $\nu \simeq 0.78$ [160]. In contrast to the $r = 2$ case, the transition along this line is expected to be in the Ashkin-Teller (AT) universality class [161], which is actually a family of universality classes parametrized by a coupling λ . At $\lambda = 0$, the Ashkin-Teller model corresponds to two decoupled Ising chains, while at $\lambda = 1$ it realizes a symmetric 4-state Potts model. The exponent $\nu \simeq 0.78$ would correspond to an AT universality class with $\lambda \simeq 0.57$ [162, 163]. Recent work on the chiral AT model has shown [156] that a direct chiral transition occurs immediately upon turning on δ for $\lambda \gtrsim 0.42$, at least up to $\lambda \simeq 0.978$, after which the chiral perturbation is irrelevant [144]. Thus the

value of $\lambda \simeq 0.57$ is inside the predicted range where a direct chiral transition would exist [156].

Similar theoretical work studying the possible conformal and chiral transitions on the period-3 and 4 phases has not been carried out. Both the Potts and Ashkin-Teller points have not been located, and there is no direct confirmation of their existence. A proper analysis of the IC-C transition of the Rydberg model is due, given the now very real possibility of accessing these transitions experimentally.

4.2 The DMRG Algorithm This section aims to describe succinctly the Density Matrix Renormalization Group (DMRG) algorithm [164] as it was implemented to obtain the results presented in this chapter. There will be some disregard towards the chronological development of the method and its roots. The original formulation based on reduced density matrices will be avoided. Readers familiar with the method may skip this section entirely.

It is common to use a matrix-based notation when discussing the Matrix Product State (MPS) representation of the algorithm [165, 166, 20], but I found a pure tensor-based notation using the Einstein summation convention to be much more convenient, and the tensor expressions translate naturally to simple diagrams in the style of tensor networks. An arbitrary tensor $M_{a_1 \dots a_l}$ can be represented in graph form as a node (or shape) with l edges coming out of it, each edge corresponding to an index. This representation suits us because the only operation between two tensors we are concerned with is index contraction (a generalization of matrix multiplication), which we indicate by connecting edges appropriately. With context and some conventions, it will be apparent from the diagrams which node/edge is which so that labeling them won't be necessary.

4.2.1 Singular value decomposition of tensors The singular value decomposition (SVD) of a matrix is a linear algebra operation that is central to the MPS representation and to the DMRG algorithm. One form of this decomposition states that any $M \times N$ matrix can be factorized as USV , where S is a square diagonal matrix with dimension $a = \min(M, N)$ and non-negative diagonal entries $s_i \equiv S_{ii}$, and where $U^\dagger U = VV^\dagger = I_a$. We won't go into how to perform this operation since very efficient SVD algorithms are most likely implemented in a linear algebra library of your favorite programming language. Rather, we will abstract this notion and generalize it to tensors: First of all, note that we can always transform any high degree tensor into a matrix by grouping its indices into two sets. For example, we can separate the list of

indices somewhere in the middle, like so: $M_{a_1 \dots a_l} \rightarrow M_{(a_1 \dots a_k)(a_{k+1} \dots a_l)}$, where we denote the sets with parentheses. More general sets with reordering of indices are of course also possible, but because we will only look at 1D systems, this will be the only type of grouping we need. We can then apply an SVD to the resulting matrix, so that the matrix splits into three matrices, USV , with U carrying the left set of the indices and V the right set. If the singular values are not of interest, we can matrix multiply S into one of the other matrices, or instead of an SVD we could have applied the related QR or RQ decompositions, all resulting in a two-matrix decomposition. We can summarize these transformations as such:

$$\text{---} \bullet \text{---} = \text{---} \bullet \text{---} \text{---} = \text{---} \blacklozenge \text{---} = \text{---} \blacktriangle \text{---} , \quad (4.3)$$

where we decomposed a tensor with two arbitrary sets of indices (separated by the dotted line) with RQ, SVD, and QR from left to right. The diamond-shaped tensor is diagonal, while the triangle tensors are "semi-unitary", in the sense that the contraction of the tensor with its complex conjugate (mirrored in the horizontal axis) on all its indices except the newly-formed index at the tip of the triangle gives us an identity tensor:

$$\text{---} \text{---} \text{---} = \text{---} . \quad (4.4)$$

To be clear, this equation is equivalent to $U_{(s)i}^* U_{(s)j} = \delta_{ij}$, where (s) is a set of indices and where we naturally represent a Kronecker delta by a single edge since $u_i v_i = u_i \delta_{ij} v_j$. Note that this property means that the "vectors" $(U_{(s)})_i$ form an orthonormal basis. We will refer to the indices formed during the decomposition, which thus are always contracted, as *virtual*, and their dimension will be denoted by D_l . In contrast, the original indices shown uncontracted in Eq. (4.3) will have some physical interpretation in a physical context, and thus we refer to them as *physical*, and their dimension will be denoted by d_l .

4.2.2 Full tensor decomposition We can apply the SVD and/or QR decompositions in Eq. (4.3) sequentially in many different ways on a tensor to decompose it as a contraction of individual tensors, each carrying one of the original indices. A possible decomposition is to use QR sequentially on a tensor and

separate all its indices, one by one, from left to right:

$$\text{Diagram 1} = \text{Diagram 2} = \text{Diagram 3} = \text{Diagram 4} . \quad (4.5)$$

We can reach other decompositions by using Eq. (4.3) to move the *center of decomposition* (CD), that is, the tensor represented by a circle or the singular value tensor. For example:

$$\text{Diagram 5} = \text{Diagram 6} = \text{Diagram 7} = \dots = \text{Diagram 8} . \quad (4.6)$$

Assuming we start from a tensor with L indices of dimensions $d_{l=1\dots L}$, what are the dimensions $D_{l=1\dots L-1}$ of the virtual indices in a full tensor decomposition? Each virtual index originates from and also delimits a partition of the physical indices into two sets, left and right. If we don't eliminate null vectors or null singular values that may arise in the sequence of decompositions, then the dimension of any virtual index is the same whether or not the left and right sets have been further decomposed or not. Given that the dimension of a virtual index created with any decomposition is the smallest of the dimensions of the two sets of indices, it follows that

$$D_l = \min \left(\prod_{k \leq l} d_k, \prod_{k > l} d_k \right). \quad (4.7)$$

4.2.3 Tensor representation of quantum objects An arbitrary state $|\Psi\rangle$ in a Hilbert space of states $|\sigma_1 \dots \sigma_L\rangle$ of L variables σ_i each taking d values can be written as $|\Psi\rangle = M^{\sigma_1 \dots \sigma_L} |\sigma_1 \dots \sigma_L\rangle$. As should be apparent now, the tensor M can be sequentially decomposed as in Eq. (4.5), each tensor carrying a single physical variable σ_i . Quantum operators on this space can go through the same decomposition. Local operators are particularly simple to represent since they are already in a local tensor representation. They can also show us the usefulness of the semi-unitarity on the state representation. By representing the complex conjugate of a tensor as its mirror image in the horizontal axis, we can write a local expectation value $\langle \Psi | \hat{O} | \Psi \rangle$ as

$$\text{Diagram 9} = \text{Diagram 10} = \text{Diagram 11} , \quad (4.8)$$

where we progressively applied the semi-unitary property of Eq. (4.4). We can see here how we can measure directly in the CD tensor any local quantities we

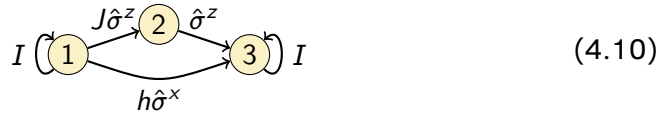
want. Moreover, replacing the operator \hat{O} by an identity, we see that the CD tensor also contains in it the norm of the state. If the CD tensor is a singular value matrix, we have that the norm of the state is the sum of the squares of the singular values, meaning any SVD we do will give us implicitly the norm of the state, and also that we have $0 \leq s_i \leq 1$ for normalized states. In fact, if two states have CDs on equal positions and differ only on the CD tensor, then the dot product of both states is given by a contraction of the CD tensors. If the CD tensors are singular value matrices, then we have $\langle \Psi | \Psi' \rangle = s_i s'_i$. Removing null singular values would of course come at no cost in the representation of a state and there is no reason not to, but note that removing small singular values has an equally small cost. We will come back to this later...

Calculating correlations of the form $\langle \Psi | \hat{O}_i \hat{O}_j | \Psi \rangle$ cannot be reduced as much in terms of operations needed, but we can minimize the cost by having the CD tensor in-between sites i and j and using again Eq. (4.4).

While a general operator of the form $M_{\sigma'_1 \dots \sigma'_L}^{\sigma_1 \dots \sigma_L} |\sigma_1 \dots \sigma_L\rangle \langle \sigma'_1 \dots \sigma'_L|$ can be decomposed through SVD/QR into local tensors, most physically relevant operators are written in terms of regular arithmetic expressions on local operators which we can exploit to build analytically a set of local tensors. For example, a TFI Hamiltonian with open boundary conditions can be decomposed with the local tensor

$$H_{ab}^{\sigma\sigma'} \equiv \begin{pmatrix} I^{\sigma\sigma'} & J(\hat{\sigma}^z)^{\sigma\sigma'} & h(\hat{\sigma}^x)^{\sigma\sigma'} \\ 0 & 0 & (\hat{\sigma}^z)^{\sigma\sigma'} \\ 0 & 0 & I^{\sigma\sigma'} \end{pmatrix}_{ab}, \quad (4.9)$$

shown as a matrix on the virtual indices $a, b = 1, 2, 3$. At the edges, the tensors only have one virtual index and are given by $H_{1b}^{\sigma\sigma'}$ and $H_{a3}^{\sigma\sigma'}$. This tensor generates the tensor product chains of operators $(I \otimes I \otimes \hat{\sigma}^x \otimes \dots)$ that compose the Hamiltonian. It has encoded in it a set of rules on what operator(s) can come next in a chain, given a partial chain. These rules can be represented as a directed graph on the virtual indices, as such:



The three virtual indices represent three possible states of a partial chain of operators: in state 1, the chain consists only of identities, while in state 3 we have already added the Pauli matrix segment so only identities can follow. In state 2, the partial chain ends with a $\hat{\sigma}^z$ so another must follow necessarily. A

fully decomposed operator is called a Matrix Product Operator (MPO).

4.2.4 The one-site DMRG algorithm We can write the eigenvalue equation $\mathcal{H}|\Psi\rangle = E|\Psi\rangle$ in tensor decomposition as

$$\begin{array}{c} \square \square \square \square \square \\ | \quad | \quad | \quad | \quad | \\ \hline \blacktriangleleft \blacktriangleleft \blacktriangleleft \bullet \blacktriangleright \blacktriangleright \blacktriangleright \blacktriangleright \end{array} = E \times \begin{array}{c} \blacktriangleleft \blacktriangleleft \blacktriangleleft \bullet \blacktriangleright \blacktriangleright \blacktriangleright \blacktriangleright \\ | \quad | \quad | \quad | \quad | \quad | \quad | \quad | \end{array} . \quad (4.11)$$

Contracting on the left and on the right with the complex conjugated semi-unitary tensors,

$$\begin{array}{c} \blacktriangleleft \blacktriangleleft \blacktriangleleft \blacktriangleleft \blacktriangleleft \blacktriangleleft \blacktriangleleft \blacktriangleleft \\ | \quad | \quad | \quad | \quad | \quad | \quad | \quad | \\ \hline \square \square \square \square \square \\ | \quad | \quad | \quad | \quad | \\ \hline \blacktriangleleft \blacktriangleleft \blacktriangleleft \bullet \blacktriangleright \blacktriangleright \blacktriangleright \blacktriangleright \end{array} = E \times \begin{array}{c} \blacktriangleleft \blacktriangleleft \blacktriangleleft \blacktriangleleft \blacktriangleleft \blacktriangleleft \blacktriangleleft \blacktriangleleft \\ | \quad | \quad | \quad | \quad | \quad | \quad | \quad | \\ \hline \square \square \square \square \square \\ | \quad | \quad | \quad | \quad | \\ \hline \blacktriangleleft \blacktriangleleft \blacktriangleleft \bullet \blacktriangleright \blacktriangleright \blacktriangleright \blacktriangleright \end{array} = E \times \begin{array}{c} \bullet \\ | \quad | \quad | \quad | \quad | \quad | \quad | \quad | \end{array} . \quad (4.12)$$

This last expression can be seen as an eigenvalue equation on the orange CD tensor and is the basic equation to solve in a one-site DMRG algorithm. Solving it for the lowest energy tensor with some eigensolver method like the Lanczos algorithm would only give us the appropriate ground state tensor if all other tensors already formed an exact decomposition of the ground state, but the resulting CD tensor will still minimize energy in some local sense and so the overall state will be closer to the ground state, no matter what the surrounding tensors are. We can further minimize energy by shifting the CD by one site as we did in Eq. (4.3) and solving the eigenvalue equation at the new CD site. Repeating this step and turning back when reaching the edge, we progressively decrease the energy, hopefully converging to the ground state. The DMRG algorithm proceeds in back and forth sweeps of local updates until some convergence criteria like the energy difference between steps is deemed small enough. We could also use the overlap $\langle \Psi | \Psi' \rangle$ between the state before and after the update, which is simply given by a contraction of the original and updated CD tensor. Another convergence criteria to consider is the energy variance $\langle \Psi | H^2 | \Psi \rangle - \langle \Psi | H | \Psi \rangle^2$, which is a better measure of the distance to a true eigenstate but as a trade-off is expensive to compute.

4.2.5 Optimal contraction order Since each update is local, it may seem at a glance that the DMRG algorithm is computationally less complex than conventional exact diagonalization (ED). Let's check explicitly the computational complexity (number of arithmetic operations) of the tensor contraction and see if this is true. In principle, when solving for the CD tensor in Eq. (4.12) we have to calculate the full tensor contraction in the first expression, and using the Lanczos algorithm one will have to repeat this contraction to generate as

many Lanczos vectors as we need. However, on each Lanczos step only the CD tensor gets updated, so that we do not need to repeat the full contraction every time. Considering the gray part as already contracted, we are left with



$$(4.13)$$

where to simplify we assume that the left and right virtual indices have the same dimension D . Tensor contraction scales as the dimension of the contracted indices times the dimension of the resulting tensor, which means Eq. (4.13) is of order $D^4 d^2$. However, since this is the most costly operation of the whole algorithm, we should make sure it is done in an optimal way. The question is, in what order should we contract the tensors in the first expression of Eq. (4.12)? Finding the optimal order of contraction on a general tensor contraction is non-trivial and a major problem in tensor network methods in larger dimensions[167], but a 1D case like this one is simple enough that finding the optimal way is manageable. The optimal order can depend on which index dimension is the largest, which in this case will be D , as we shall see. Then the best way to do this contraction is column by column, edges to middle of the chain. Again, we can exploit the fact that only the CD tensor is updated. Having already contracted all columns except the CD column, we have



$$(4.14)$$

where we define χ as the virtual index dimension of the Hamiltonian tensor, and where we label tensors in the order they should be contracted (1 and 4 could of course be swapped). The leading order contractions are 2 and 4, of order $D^3 \chi d$. For better time efficiency in DMRG, we can additionally save all the partial contractions from the edges up to each column, and update these contractions as necessary as we move the CD.

All that is left now to get the full complexity of DMRG is to determine the order of D . Since all the physical indices have the same dimension d , it follows from Eq. (4.7) that

$$D_l = \min(d^l, d^{L-l}). \quad (4.15)$$

4.2.6 Why DMRG works If this was all there was to DMRG, then it would be no more than a curiosity and no better than ED. But focusing on the scaling would be missing the point. In practice, one rarely uses DMRG to find an exact ground state, if ever. Instead we limit the virtual index dimension, if necessary by discarding the smallest singular values up to some number D of our choice:

and we take the truncated MPS as a variational state on which we do DMRG sweeps. The claim is that even for extremely large system sizes, we can always find a limit D such that the variational state is effectively equal to the ground state up to our intended precision. How can this be?

$$\begin{array}{c} \text{---} \end{array} \xrightarrow{D=1} \begin{array}{c} \text{---} \end{array} \quad (4.17)$$
$$\text{Diagram 1} \quad , \quad (4.18)$$

where the thicker vertical edges are supposed to represent all the physical indices on each side. Let us say the partition resulted in D singular values, which will be the dimension of the virtual index. We can see the side tensors as sets of D vectors, one for each singular value. Then, given the semi-unitary property (Eq. (4.4)), each set forms an (incomplete) orthonormal basis. We could write the decomposition as such:

$$|\Psi\rangle = \sum_{i=1}^D s_i |u_i\rangle \otimes |v_i\rangle, \quad (4.19)$$

where $\langle u_i | u_j \rangle = \langle v_i | v_j \rangle = \delta_{ij}$. This is called the *Schmidt decomposition*. This decomposition is useful because it helps us see that the i -th singular value squared is the probability of observing the state $|u_i\rangle \otimes |v_i\rangle$. An observation on one side will give a unique outcome on the other side, so the distribution of singular values squared represents exactly the entanglement between both sides. A proper way of quantifying the amount of entanglement is with the von Neumann entropy of this distribution, also called the *entanglement entropy*:

$$S \equiv - \sum_{i=1}^D s_i^2 \log s_i^2. \quad (4.20)$$

For an infinite system, an SVD partition of a non-trivial state will give an infinite number of positive singular values in the range of 0 to 1, which we can sort from largest to smallest. What makes DMRG work is that even when $L \rightarrow \infty$, the entanglement entropy of typical 1D ground states will saturate to a finite value, or equivalently, the distribution of the singular values has an exponentially decaying tail, so a truncation of the singular values somewhere in the exponential regime gives us a great approximation of the state.

By typical ground states we mean in particular the ground states of gapped, local, unfrustrated Hamiltonians. For such Hamiltonians, the correlations between local operators decay exponentially at large enough distance with a characteristic length ξ ,¹ which in natural units we can expect to behave as the inverse of the energy gap. The correlation length is therefore finite at infinite length, so partitions of the state which are at a distance significantly larger than ξ are effectively independent. The contributions to the entanglement at a partition boundary come mainly from the entanglement between sites in a neighborhood of the boundary of size determined by ξ . Increasing the length

¹While different correlation functions don't have necessarily the same correlation length, we can take ξ to stand here for the largest one.

of the chain won't increase significantly the entanglement, and therefore S is finite at any length.

The entanglement entropy is still an "extensive" quantity, but this quantity lives in the bond separating subsystems, so it will grow roughly proportionally to the area of the partition boundary between subsystems, or in discrete terms, proportionally to the number of bonds that cross the boundary. We can summarize this property as $S \sim L^{d_s-1}$, where d_s is the spatial dimension. This property is known as the *area law* of the entanglement entropy [169].

In turn, gapless Hamiltonians have power-law decaying correlation functions, and we can expect the same heavy-tail behavior in the singular values, so any truncation we do will be significant. In this case, it is known from CFT that in 1+1D the entanglement entropy scales as the logarithm of the subsystem length [170]. This scaling is not so bad, and in practice DMRG is still very useful for such systems.

In summary, the MPS representation of a state is a natural way of representing quantum entanglement, as first demonstrated with the exact solution of the AKLT model [20]. The area law states that for gapped ground states the quantity of information on a partition of the state is proportional to the area of the partition boundary, implying it is a bounded quantity in 1D systems. This allows us to truncate the virtual index dimension with little cost and obtain ground states at system lengths much larger than what is possible with conventional ED methods.

4.2.7 Convergence of DMRG While each DMRG update of a local tensor is guaranteed to reduce the energy, nothing guarantees that we will converge to the ground state. In our descent of the energy landscape, we might be attracted towards a local minimum and never be able to escape. Since the local update is based on ED methods like Lanczos that preserve well-defined conserved quantities of our initial guess, we cannot reach the ground state if we start in the wrong symmetry sector. However, the problem of DMRG is more severe in that we might get stuck even if we start in the symmetry sector of the ground state.

The problem is particularly clear in the one-site DMRG algorithm in the presence of a conserved quantity like the magnetization $\sum_i \langle \hat{\sigma}_i^z \rangle$. Once our state reaches a well-defined magnetization, the Lanczos algorithm will not allow us to change it anymore, which also means the magnetization at any single site $\langle \hat{\sigma}_i^z \rangle$ cannot change alone, it has to swap or mix with the rest of the chain, but since the update is local and each local tensor carries in it the local magnetization $\langle \hat{\sigma}_i^z \rangle$ as we saw with Eq. (4.8), we effectively have local

magnetization conservation which imposes a severe restriction on how the local tensor can be updated, so that we might never reach the ground state even while being in the same symmetry sector.

Even if we are not exactly at a defined magnetization but only close, the energetic cost of locally changing the magnetization to reach other plateaus can still be too high and so we are at risk of quickly falling into the energetically closest magnetization plateau and therefore the magnetization freezing locally.

4.2.8 Two-site DMRG There are modifications of the one-site algorithm that can prevent the state from getting stuck and even speed-up convergence [171]. However, the most common approach to attenuate this problem is to instead update two consecutive sites on each DMRG step. This means that in Eq. (4.12) we leave two sites uncontracted, one of them being the CD tensor:

$$\text{Diagram of two-site contraction} = E \times \text{Diagram of one-site contraction} \quad (4.21)$$

The complexity of the contraction becomes $D^3 \chi d^2$, just d times larger than for one-site. We can start the Lanczos algorithm with the contraction of the two tensors to be updated. After converging with Lanczos to some tensor with two physical indices, we perform an SVD or QR/RQ to separate again the indices and at the same time move the CD tensor to the next site to carry on with the next update.

In the context of the freezing magnetization discussed above, the two-site update would allow the mixing of local magnetization between the sites and thus allow a much larger subspace in which to update the tensors.

The two-site modification carries an additional advantage: After the two-site tensor update and subsequent SVD, the index that connects the two sites can be up to d times larger than before. We could again truncate the singular values up to the previous dimension D , or we could let the index dimension grow. Instead of setting a hard limit D , we could instead look at the singular value distribution and decide more carefully where to truncate. For example, it is common to discard singular values smaller than 10^{-8} since these carry a statistical weight smaller than machine double-precision. Being able to dynamically change D throughout the simulation is also useful if we have a good guess MPS of small virtual index dimension to start DMRG with.

4.2.9 The starting MPS As a starting point for the algorithm, we could generate random tensors with the appropriate dimensions, taking already into account a limit D to the virtual index dimensions, then left/right-orthogonalize them and finally normalize the CD tensor. A better approach is to grow a small MPS up to the size L we wish. This is commonly called *infinite-system* DMRG, in contrast with *finite-system* DMRG (the one- and two-site algorithms we described) where the size remains the same. The chain growth can be formulated as follows (the tensor color is for guidance only):

- Start with a small MPS of length $X \ll L$. We could obtain this MPS from random tensors or, even better, from the decomposition of an exact ground state obtained from ED. Let's say the length is even, for simplicity, and that the CD is a singular value tensor in the middle of the chain:

[illegible]

- We substitute the CD singular value tensor by a random normalized tensor with two physical indices and two virtual indices with equal virtual dimensions as the singular value tensor:

$$\dots \quad \text{---} \left(\begin{array}{c} | \\ \text{triangle} \\ | \end{array} \right) \left(\begin{array}{c} | \\ \text{triangle} \\ | \end{array} \right) \left(\begin{array}{c} | \\ \text{oval} \\ | \end{array} \right) \left(\begin{array}{c} | \\ \text{triangle} \\ | \end{array} \right) \left(\begin{array}{c} | \\ \text{triangle} \\ | \end{array} \right) \text{---} \quad \dots \quad (4.23)$$

- We then solve the two-site DMRG equation for this tensor we introduced and update it accordingly.
- Finally, an SVD on this tensor leaves us with a chain similar to the starting chain but with two more sites:

[illegible]

- We repeat these steps until we reach the intended length L . If L is odd, at the last step we can substitute a tensor with a single physical index instead.

Note that we have to grow the chain by at least two sites to allow the virtual index dimension to grow if necessary. However, to speed up the growth we can set a limit D_g during the growth which is significantly smaller than the finite-system D , in the hope that the few states $|u_i\rangle \otimes |v_i\rangle$ generated during the infinite-system DMRG are representative of the subspace of states of largest singular values of the target ground state, making this state an excellent starting point to optimize from.

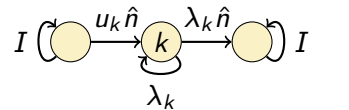
4.2.10 Implementation The basic code implementation of DMRG used in this chapter is made available on Github². Some work is still needed documenting its structure so it can be used by others, and further functions were written around this code which are not yet made available, but the published code can already be run on the Rydberg model.

4.3 DMRG implementation of the Rydberg model In this section we will discuss details of the DMRG simulation specific to the Rydberg model, which include the MPO implementation of the model, our choice of convergence parameter, and how we measured the correlation length and wave-vector from our results.

4.3.1 MPO form of the Hamiltonian The long-range interaction term of the model requires some care in its implementation in the MPO representation of the Hamiltonian. We could treat each term at a unit distance r separately, each term being implemented with its own virtual state (Eq. (4.10)), and to avoid having the virtual MPO dimension χ grow with the system size, we can truncate the power-law somewhere, which does not imply such a large error due to the large exponent of the interaction. However, there is a better approximation we can do which preserves the power-law at all length scales. While it is not obvious why, a power-law decay can be well approximated by a sum of exponentials of different weights and length scales [172]. The approximated interaction term looks like this:

$$\sum_i \sum_{r>0} \hat{n}_i \hat{n}_{i+r} \sum_{k=1}^m u_k \lambda_k^r. \quad (4.25)$$

Exponential interactions are much more straightforward to implement in an MPO representation [173, 166]. Each of the m exponential terms can be included with no approximation in the local Hamiltonian tensor as such:



$$I \left(\text{circle} \right) \xrightarrow{u_k \hat{n}} \left(\text{circle} \right) \xrightarrow{\lambda_k \hat{n}} I, \quad (4.26)$$

λ_k

where we follow the conventions of Eq. 4.10. In this work we have used twelve exponentials ($m = 12$). Together with the Δ and Ω terms, this results in $\chi = 14$. A good set of parameters for the approximation can be found with a regular

²www.github.com/ivomac/DMRG_code

u_n	λ_n	u_n	λ_n
$-4.375\,780 \times 10^{-2}$	0.325\,988	$1.936\,228 \times 10^{-5}$	0.634\,314
$-3.707\,815 \times 10^{-2}$	0.326\,220	$1.244\,534 \times 10^{-3}$	0.429\,284
$-1.216\,618 \times 10^{-6}$	0.787\,502	$6.849\,186 \times 10^{-2}$	-0.017\,733
$2.120\,790 \times 10^{-18}$	1.013\,796	$7.054\,547 \times 10^{-2}$	0.103\,117
$4.620\,461 \times 10^{-7}$	0.830\,014	$8.547\,828 \times 10^{-2}$	0.322\,411
$4.587\,174 \times 10^{-6}$	0.730\,021	$8.550\,526 \times 10^{-1}$	0.009\,142

Table 4.1: Power-law fitting coefficients used for 601 sites, rounded to 6 decimal places. The closeness of some λ_n suggest that the fit could be improved even further. However, it is not clear how to properly approach the search for a global minimum to the problem given the large number of parameters.

gradient descent minimization of the cost function:

$$F \equiv \sum_{r=1}^L \left(r^{-6} - \sum_{k=1}^m u_k \lambda_k^r \right)^2. \quad (4.27)$$

For all sizes considered in our simulations, the minimized cost function was smaller than 10^{-16} . Specifically, our simulations on chains of length $L = 601$ used the parameters shown in Table 4.1, with a resulting cost function $F = 3.8 \times 10^{-19}$. As a comparison, a truncation of the power-law preserving the first 12 terms results in an equivalent squared differences error of $\sim 7.5 \times 10^{-14}$.

4.3.2 Correlations and q-vector After meeting our convergence criteria towards a ground state estimate, we measure the correlation function between the middle site j and site $j + r$,

$$C_r \equiv \langle \hat{n}_j \hat{n}_{j+r} \rangle - \langle \hat{n}_j \rangle \langle \hat{n}_{j+r} \rangle. \quad (4.28)$$

We obtain the correlation length ξ and q by fitting the correlation function with the expected Ornstein-Zernike (OZ) form [174]:

$$C_r \sim A_r \cos(2\pi q r + \phi_0), \quad (4.29)$$

where

$$A_r \equiv A_0 \frac{e^{-r/\xi}}{\sqrt{r}}. \quad (4.30)$$

What we want to observe and fit for is the dominant exponentially-decaying term of the correlation, which might only clearly appear for some finite r . At

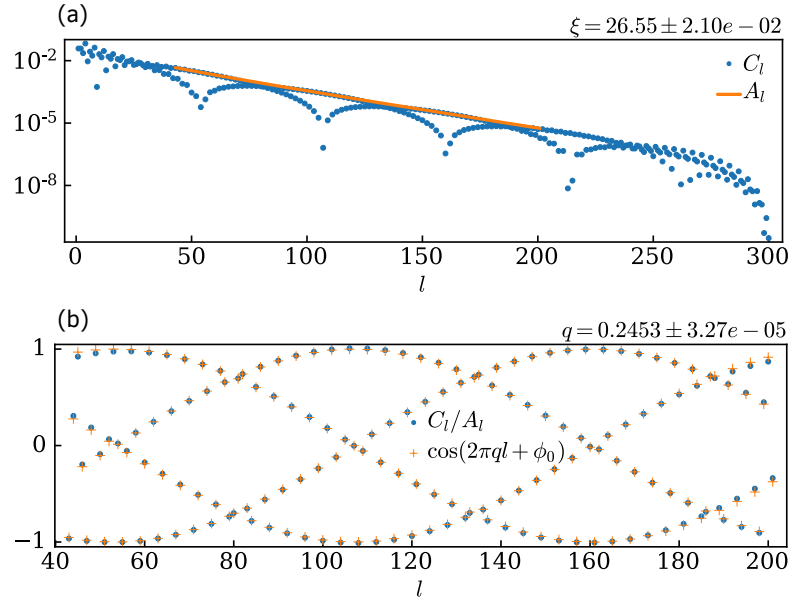


Figure 4.2: Demonstration of a successful fit using the two-step fitting scheme for a 601 site simulation along the c_8 cut (Fig. 4.1), at $(\Delta/\Omega, \mathcal{R}_b) = (2.23, 3.32)$.

the same time, when r is closer to L , boundary effects will be prevalent, so we discard points from the head and the tail-end of the correlation function until an OZ regime is thought to be reached, then we fit the remaining points. One should also pay attention to possible machine-precision errors when the correlation length is very low. In practice, we removed all points where the correlation was smaller than 10^{-12} . We implemented a two-step fitting scheme (Fig. 4.2) that has been described before [160], where first we obtain ξ and A_0 by performing a linear fit on $C_r\sqrt{r}$ in a semi-log scale. Then, q is obtained by a least-squares cosine fit on C_r/A_r , where one minimizes the cost function $F(q)$ defined as the sum of squared differences.

In general, we find the limit of reliable correlation lengths to be $\xi \sim L/6$, beyond which ξ is noticeably affected by the finite size. Still, we find that the q -vector suffers less from finite size effects than ξ , thus a cosine fit beyond this ξ limit can still give an accurate estimate of q .

Error bars The confidence intervals (error bars) of q are an estimate of the fitting error. They are calculated by assuming that the error δq is proportional to the cost function. It then follows that $\delta q = F(dF/dq)^{-1}$ in lowest order, which can be explicitly calculated. The main contributions to this error are

not precision errors in the fitting algorithm, but are instead errors in the determination of ξ and A_0 , or deviations from an OZ regime. The error bars of ξ were deemed too small to be represented. The error on $\xi\bar{q}$ is derived from these errors by the differential chain rule.

Fitting problems on close-to-commensurate q values The automatic two-step fitting algorithm described above does have some pitfalls, and some manual intervention was required in some cases. A common problem that appeared were unnatural "kinks" when looking at q and/or ξ along some cuts. The following explanation was found for this problem, which turns out to be a general fitting problem that is certain to happen in close-to-commensurate systems. When q takes a value commensurate with the lattice, say q_0 , the fit to obtain ξ is quite simple and very accurate, since the correlation function has an exact period of $1/q_0 = p$. In this case, if one only takes the points that are local maxima of the correlation, they will form a perfect line (in semi-log scale, correcting for the \sqrt{l} factor). In fact, the semi-log plot will show a sequence of p possibly overlapping lines, all with the same slope, each associated with the p values that $\cos(2\pi q_0 l)$ can take (we set $\phi_0 = 0$ for simplicity). However, a small shift away from the commensurate value will cause these lines to move. Taking $q = q_0 + \varepsilon$, the oscillating part of C_r can be written as:

$$\frac{C_r}{A_r} = \cos(2\pi q_0 l + 2\pi \varepsilon l). \quad (4.31)$$

The deviation ε will act as a phase shift on $\cos(2\pi q_0 l)$. Since we fit the absolute value of C_l , each line returns to its initial value after $1/(2\varepsilon)$ points. A maxima is reached every $1/(2p\varepsilon)$ points. This means that, if the number of points X we use to fit A_l is smaller than $1/(2p\varepsilon)$, there is a single maximum of the oscillation in our interval, thus we are not able to see the enveloping function A_l . This sets a limiting frequency shift $\varepsilon_c \equiv \frac{1}{2Xp}$ below which the fitting error of q and ξ should increase. The error again goes to zero when $\varepsilon \rightarrow 0$, so we could expect our error will be maximum at $\varepsilon = \varepsilon_c/2$, that is, when we only see half a period of the phase shift. In this case, we can expect the fitted value of ξ to be smaller than what it should. This was observed in several of the cuts we consider below: when q was close to $\varepsilon_c/2$ in the disordered side of our cuts, we often saw a kink in q or ξ . While some small algorithm modifications did help with this problem, it was hard to properly solve all the kinks, so some kinks were dealt with by manually finding pairs of q and ξ values which resulted in a reasonable cosine behavior of C_r/A_r , and then using those parameters as starting points for the fitting optimization.

4.3.3 Convergence As a convergence criteria for our simulations, we required the relative energy variance

$$\frac{\langle \Psi | H^2 | \Psi \rangle}{\langle \Psi | H | \Psi \rangle^2} - 1, \quad (4.32)$$

where $|\Psi\rangle$ is the variational MPS state, to be smaller than 10^{-11} when estimating the boundaries of phases and 10^{-12} when determining critical exponents and equal- q lines. A limit of $D = 350$ was typically enough to reach such precision for 601 sites, while index dimensions up to 500 were used to reach convergence close to or inside the gapless floating phases.

4.4 Results Our objective in the following sections is to use DMRG to study the IC-C transitions of the long-range interacting Rydberg model. We map the q -vector on the incommensurate disordered phase and accurately determine where the $q = 1/3, 1/4$ equal- q lines intersect their respective ordered phases. We discuss our approach in tackling the IC-C transitions and present our results along many cuts (all shown in Fig. 4.1), for chains of 301 and 601 sites. We also look at the finite-size scaling of the conformal points at experimentally relevant sizes. Finally, we discuss our attempts and failure at reproducing the floating phase boundary of Ref. [159].

To avoid stability problems in DMRG, we chose system sizes of the form $L = 12I + 1$ with I integer, which split the ground state degeneracy in the ordered phases by guaranteeing a single ground state with occupied edges for $p = 3, 4$. For the full phase diagram (Fig. 4.1) we chose $L = 121$ which stabilizes all relevant orders. This phase diagram gave us a first estimate of the q -line intersection points. In particular, it already showed that only the commensurate lines intersect the ordered lobes, while all the other lines avoid them and continue in-between lobes. The same behavior is observed at all parameter scales we consider, as shown below. However, there are ordered phases of other rational periods in the regions between the $1/p$ phases, but these phases only appear at larger Δ/Ω [159], beyond the scale we looked at. It is natural to expect the appropriate equal- q vectors to also intersect these phases. All these phases seem to be covered by a floating phase [159], although there is some chance that the prominent $q = 2/5$ phase between $1/2$ and $1/3$ is not completely covered. Still, the focus for now is in the dominant ordered phases $1/p$ which are experimentally more accessible and pose the major open questions regarding the IC-C critical nature.

In all our plots of ξ and q along some cut in the phase diagram, points which are filled (fully colored) are considered in the power-law fits, while hol-

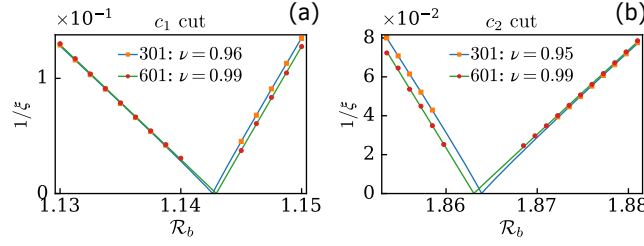


Figure 4.3: Correlation length along the $\Delta/\Omega = 3$ cut (left) that crosses the commensurate transition line below the period-2 lobe, and the $\Delta/\Omega = 2$ cut (right) that crosses it above. All points shown in the disordered sides are inside the commensurate phase. The minimal finite-size effects observed let us conclude from the exponent obtained that the transition is continuous and in the Ising universality class.

low points are not. For clarity, we do not show data points close to the transitions if they were not included in the fit. These points were removed in the first place mainly because they were clearly affected by finite-size effects. We also only show error bars on the filled points.

4.4.1 Period-2 cuts We start by looking at the order-disorder transition on the period-2 phase. This was the easiest case to tackle, with bond dimensions of less than 150 being required to get the accuracy of 10^{-12} in our criteria, and minimal finite-size effects already for 301 and 601 sites. In general, as we increase R_b , the complexity increases and larger bond dimensions are required to achieve the same precision.

In contrast to the $p \geq 3$ cases, the $1/2$ lobe is surrounded by a commensurate disordered (CD) phase. The q -vector changes sharply close the CD border and becomes practically flat inside, with a minimal variation of magnitude smaller than 10^{-3} . This criteria was used to set the CD border shown in the phase diagram. We have checked that this phase extends at least up to $\Delta = 0$. The CD to ordered phase transition was found to be continuous and in the Ising universality class. We confirmed this by taking several cuts along the phase boundary and verifying that upon approaching the transition the correlation length diverges with the critical exponent $\nu \simeq 1$. We confirm this at least up to the deepest cuts we considered at $\Delta/\Omega = 3$, as seen in Fig. 4.3. Above the lobe (on the side closer to the $1/3$ phase), we looked at cuts up to $\Delta/\Omega = 2$, with similar results. We did not look at cuts beyond $\Delta/\Omega = 2$ above since it was expected already from the effective $r = 2$ blockade model that the transition would be Ising on this side [149, 152]. However, as we move

away from the $1/3$ phase, the Ising critical line of the blockade model eventually ends at a tricritical Ising point, below which the transition is first order. We did not find any evidence of a first order transition in the Rydberg model. It is not very surprising though because the tricritical point of the blockade model is located at negative (attractive) next-to-blockade interactions, which naturally does not occur in the Rydberg model. A more appropriate effective model of the lower part of the $1/2$ lobe is the $r = 1$ blockade model, where a change of variables to a spin system results in an Ising model with transverse and longitudinal fields where the transition is always Ising [175].

4.4.2 The product criteria The product $\xi\bar{q}$, where we define $\bar{q} \equiv |q - 1/p|$, can let us differentiate between a conformal, chiral, and intermediate floating phase without relying on accurate estimates of exponents. This quantity will diverge at the KT transition of a floating phase ($\xi = \infty, q \neq 1/p$), approach a constant for a chiral transition ($\bar{\beta} = \nu$), and go to zero for a conformal transition ($\bar{\beta} > \nu$) [77]. Thus we also show this quantity for each of our cuts, when applicable.

When drawing conclusions from $\xi\bar{q}$, one should be aware of how the inevitable finite-size effects will affect it, in particular when we are very close to a transition. On one hand, ξ is limited to some maximum value determined by the chain length, so we could expect a bias towards lower values of $\xi\bar{q}$ than expected as we approach the transition. This is in part compensated by both fitting errors or actual biases of the q -vector value with respect to the expected, which keep \bar{q} from being zero at the transition and thus push $\xi\bar{q}$ to be bigger.

In practice, points where the correlation length was noticeably limited were easy to identify and were removed. The error in \bar{q} was more problematic: a slight shift across the whole cut was commonly observed, in particular for 301 sites. The resulting error is more prominent on cuts where $\xi\bar{q}$ is mainly flat (chiral): one commonly sees a slow but smooth increase in $\xi\bar{q}$ as we approach the transition, for example in panel (n) of Fig. 4.5. Still, the effect is visibly reduced for 601 sites in all affected cuts.

4.4.3 Procedure for period-3 and 4 phases A very similar approach was conducted for both the $1/3$ and $1/4$ cases that we now describe: First, the region close to the tip of the ordered lobes were mapped with $L = 301$ data (Figs. 4.5(d) and 4.6(d)). From these regions, we get a first estimate of where the conformal points occur. Next, we improve our estimate of the $q = 1/3$ and $1/4$ lines by going even closer to the conformal points and mapping this

region with $L = 601$ data (Fig. 4.4). At this scale, the equal- q lines are effectively linear. We fit these lines and then determine ν along these cuts (P and AT cuts in Figs. 4.5(a) and 4.6(a) respectively). The point where ξ diverges, or equivalently where $1/\xi$ vanishes, is our estimate of the location of the conformal points, and the exponent with which it diverges is our numerical estimate of ν .

To further characterize the conformal transitions, we considered vertical and horizontal cuts that go through the estimated P and AT points respectively. These are labeled "P/AT cut (vertical/horizontal)" in Figs. 4.5 and 4.6. Along these cuts, q varies, and accordingly one can estimate the exponent $\bar{\beta}$ and follow the behavior of $\xi\bar{q}$. The two vertical lines on the \bar{q} and $\xi\bar{q}$ plots are the 301 and 601 site estimates of the critical points obtained from the correlation length fit. To fit the \bar{q} power-laws, we fix the critical points to these estimates.

Having accurate estimates on the conformal transitions, we move away from these points along the transition lines in the hope of targeting direct chiral transitions and also indirect transitions beyond the chiral lines. Most of our results on IC-C transitions for $q = 1/3, 1/4$ are shown in Figs. 4.5 and 4.6 respectively.

4.4.4 Determining the P and AT cuts We obtain the equal- q lines in our phase diagrams by interpolation of the q -vector on a finite grid. We use this same method to accurately determine where the $q = 1/3$ and $1/4$ lines intersect their respective ordered phases, using data from simulations on 601 sites very close to the phase boundary, as shown in Fig. 4.4. The resolution in q that we reach is of the order of 10^{-4} . The grid data in these figures show the order parameter O (Eq. (4.35)). We can see in these figures the start of the ordered phases in the top right. Linear fits of the interpolated lines give us the following:

$$\mathcal{R}_b \simeq 0.1284\Delta/\Omega + 1.9527, \quad (q = 1/3, \text{P cut}), \quad (4.33)$$

$$\mathcal{R}_b \simeq 0.1441\Delta/\Omega + 2.8747, \quad (q = 1/4, \text{AT cut}). \quad (4.34)$$

Simulations along these linear fits then lead to estimates of the conformal critical points. To note that a slight drift of the equal- q lines is noticeable when comparing these results with the equal- q lines obtained for 301 sites shown in Figs. 4.5(a) and 4.6(a). In these plots, the black lines are given by Eq. (4.34). A proper finite-size scaling of the equal- q lines was not done.

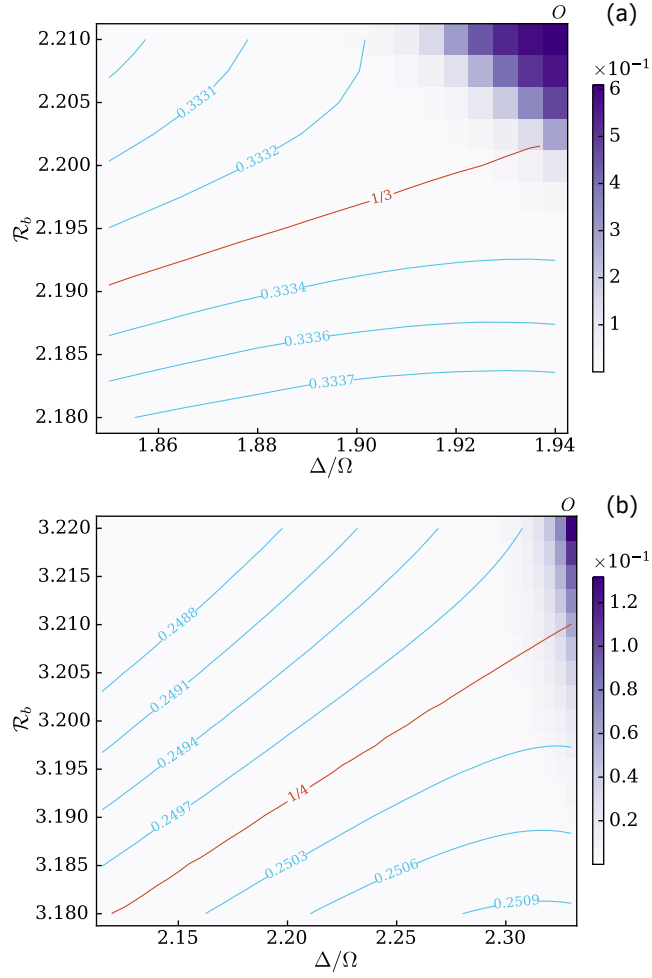


Figure 4.4: Regions where the $q = 1/3, 1/4$ lines intersect the ordered phases. The colored grid data shows the order parameter O (Eq. (4.35)). A linear fit of the $1/3$ line gives $\mathcal{R}_b = 0.1284\Delta/\Omega + 1.9527$ (P cut), while for $1/4$ we have $\mathcal{R}_b = 0.1441\Delta/\Omega + 2.8747$ (AT cut). All other equal- q lines are repelled when approaching the ordered phases.

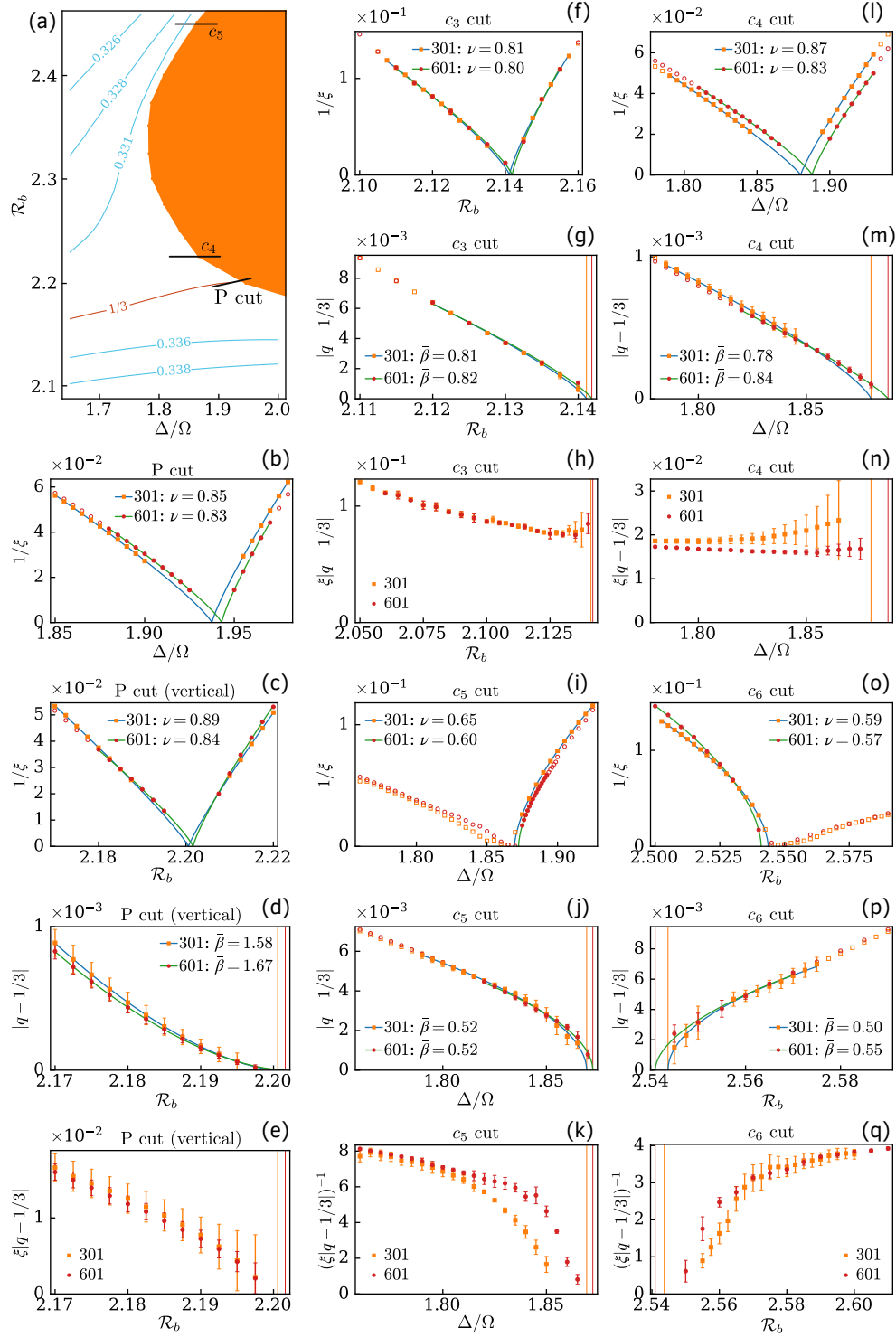


Figure 4.5: Scaling across the boundary of the period-3 phase along P, P vertical, $c_{3,4,5,6}$ cuts. (a): Tip of the $1/3$ lobe, mapped with $L = 301$ data. Note the inverted y-axis in panels (p) and (q).

4.4.5 Period-3 cuts Along the P cut, we expect to find a phase transition in the three-state Potts universality class, with exponents $\nu = 5/6 \simeq 0.833$, $\bar{\beta} = 5/3 \simeq 1.66$ and $\beta = 1/9$ [154, 155]. Our results for 601 sites agree within 1% with the theory predictions (Fig. 4.5(a, b, e)). The location of the critical point P is $(\Delta/\Omega, \mathcal{R}_b) \simeq (1.942, 2.202)$. The discrepancy in the 301 site exponents could be due to finite-size effects displacing the $q = 1/3$ line, so that along this cut we slightly missed the 301 site equal- q line. As expected, the concavities of q and ξ are opposite, and $\xi\bar{q}$ converges to zero (Fig. 4.5(g)). Overall, our results provide strong evidence in favor of a three-state Potts universality class at the point P.

Let us now discuss the results we have obtained away from this point. Both above the $1/3$ line (c_4 cut, horizontal, $\mathcal{R}_b = 2.225$) and below it (c_3 cut, vertical, $\Delta/\Omega = 2.4$) we find evidence of a chiral transition: $\xi\bar{q}$ is nearly flat upon approaching the transition (Fig. 4.5(h, n)). Note that cut c_3 (f, g, h) shows very little difference between the 301 and 601 data: The data are pretty much overlapping. This is due in part to the comparatively small correlation length values at the chosen scale of \mathcal{R}_b , but this only proves that one can draw stronger conclusions at just 601 sites. With both the ν and $\bar{\beta}$ exponents being so far from the expected $1/2$ for a PT transition, this limits a possible intermediate floating to be extremely narrow in this scale. Even if such a phase exists, on most length scales the transition will still look chiral from the standpoint of the correlation length and q -vector.

Along the cut c_5 at $\mathcal{R}_b = 2.45$, further above, the IC-C transition is more consistent with Pokrovsky-Talapov. Our finite-size $\nu' \simeq 0.6$ is slightly larger than the expected value $\nu' = 1/2$, but $\bar{\beta} \simeq 0.52$ is in very good agreement with the PT value $\bar{\beta} = 1/2$. It does make sense that $\bar{\beta}$ is more accurate since in DMRG, q converges faster than ξ . On the disordered side of the transition, we find a rapidly growing correlation length which later levels off before the PT transition at a very large value. The plateau is slightly smaller in Δ/Ω for 601 sites. This can be understood as a KT transition into a floating phase, with the ξ plateau being limited by the finite size. The $\xi\bar{q}$ product shows more clearly a divergence in the correlation length before q becomes commensurate. Extrapolating to infinity this divergence, we would find a floating phase of width in Δ/Ω of approximately 0.01 for 301 sites and 0.004 for 601 sites. This result might indicate that the floating phase reaches closer to the top of the lobe than what is shown in the phase diagram. Alternatively, the shrinking width of the floating phase with system size could suggest that there will be a crossover to a chiral regime at larger system sizes. One should note that the correlation length of the plateau on the IC side of the transition, while it

is certainly very large, it is also comparable to system size, thus substantially above what we would consider reliable. Simulations at larger system sizes would make the transition along this cut clearer. Still, while it may not be completely convincing, the observed behavior still contrasts with respect to the chiral/conformal situations.

Cut c_6 , located further above in \mathcal{R}_b is qualitatively equivalent to cut c_5 , but shows a narrower difference between system sizes, especially comparing $\xi\bar{q}$ between both cuts (k, q). Still, it may not be sufficient to completely discriminate between chiral and floating in the infinite length limit.

4.4.6 Period-4 cuts Turning now to the IC-C transition of the $1/4$ phase, much of the discussion of the $1/3$ case will repeat. We will discuss all the cuts in Fig. 4.6. Along the commensurate line and for 601 sites, we find a phase transition at a point denoted AT in Fig. 4.1 at $(\Delta/\Omega, \mathcal{R}_b) \simeq (2.346, 3.213)$ with exponent $\nu \simeq 0.80$, which is consistently replicated with a horizontal cut that crosses this critical point. The $\bar{\beta}$ exponent, unknown analytically for the AT universality class, is nevertheless larger than one and so the $\xi\bar{q}$ product decays to zero at the transition.

The situation around the AT point and around the P point are very similar. The c_7 cut ($\mathcal{R}_b = 3.22$) is in agreement with a direct chiral transition of exponent $\nu (\simeq \bar{\beta})$ slightly larger than at the AT point, suggesting that this exponent increases as we initially move away from the AT point.

Cut c_8 ($\mathcal{R}_b = 3.32$) shows the clearest indication of an intermediate floating phase out of all the c_n cuts, which makes sense since it is also the closest to the expected floating region shown in Fig. 4.1. The $L = 601$ exponents $\nu' \simeq 0.52$ and $\bar{\beta} \simeq 0.47$ are in good agreement with the PT universality class, and the correlation length shows different behaviors on both sides of the transition. The $\xi\bar{q}$ product diverges as expected, similarly to cuts c_5 and c_6 , with the exception that in the c_8 cut the 301 site data are mainly above the 601 line, meaning $(\xi\bar{q})_{301} \lesssim (\xi\bar{q})_{601}$, while the opposite is observed in cuts c_5 and c_6 .

4.4.7 Order parameter scaling To further confirm the conformal nature of the transitions along the commensurate lines, we looked at the scaling of the order parameter O defined as the maximal local difference in the occupation $\langle \hat{n}_l \rangle$. To be sensitive to all relevant periods of the occupation oscillation ($p = 2 \cdots 5$), we consider the maximal oscillation in the middle 10 sites, leading to the following definition of O :

$$O \equiv \max_{l \in J} \langle \hat{n}_l \rangle - \min_{l \in J} \langle \hat{n}_l \rangle, \quad (4.35)$$

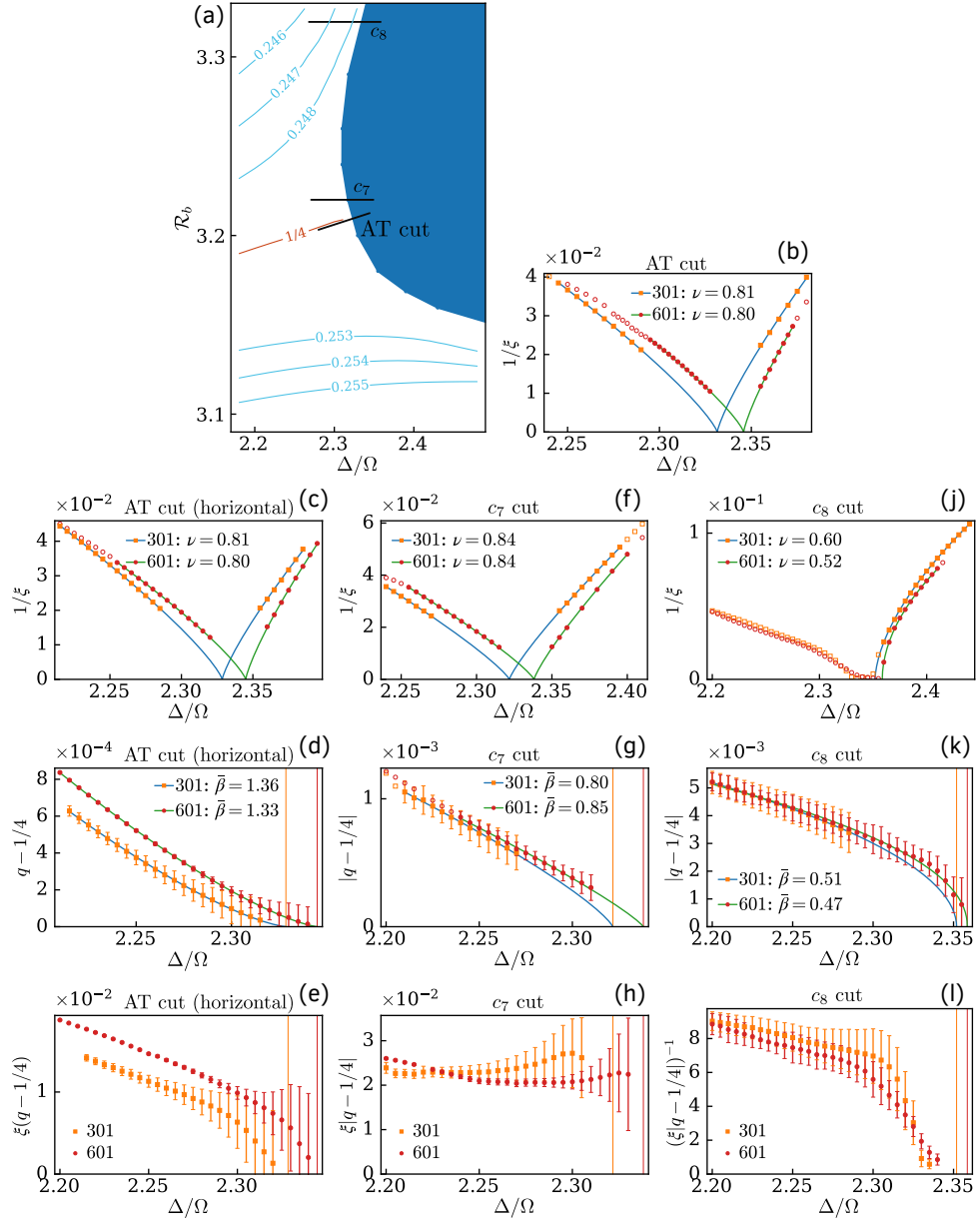


Figure 4.6: Scaling across the boundary of the period-4 phase along AT, AT horizontal, c_7 and c_8 cuts. (d): Tip of the $1/4$ lobe, mapped with $L = 301$ data. Note the inverted y-axis in panel (k).

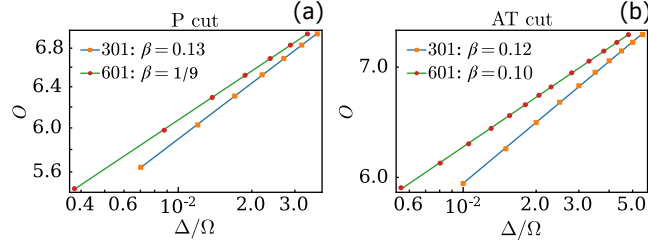


Figure 4.7: Order parameter scaling along (a) the P and (b) the AT cuts (note the log-log scale). The data was fitted with the expected power-law behavior: $O \sim \|\Delta/\Omega - (\Delta/\Omega)_c\|^\beta$. For 301 sites both the exponent and the critical points are fitting parameters, while for 601 sites β is fixed to the expected values to show the good agreement with our estimated ν along these cuts. The horizontal coordinates were shifted by the estimated critical point values.

where $J \equiv \{\frac{L-1}{2} - 4, \dots, \frac{L-1}{2} + 5\}$ for odd L . The results are shown in Fig. 4.7. Along the P cut, and for 601 sites, the scaling is in excellent agreement with the exact result $\beta = 1/9$. While β is not known exactly in the AT universality class, it will be related to ν by the scaling relation $\beta = \nu\Delta_\phi$, where Δ_ϕ is the lowest CFT scaling dimension of the AT model, which has been measured as $\Delta_\phi = 1/8$ in MERA simulations on the chiral AT model, independently of the coupling λ [176]. Given Δ_ϕ and ν , we can produce estimates of all the other critical exponents:

$$\begin{array}{cccccc} \alpha & \beta & \gamma & \delta & \eta & \nu \\ \frac{4}{10} & \frac{1}{10} & \frac{7}{5} & 15 & \frac{1}{4} & \frac{4}{5} \end{array} \quad (4.36)$$

For 601 sites, the scaling is in good agreement with the expected $\beta \simeq 0.10$.

4.4.8 Finite-size scaling It is already apparent from the results shown for 301 and 601 sites that a significant drift of the equal- q lines and of the phase boundaries happens at small system sizes. Indeed, as shown in Fig. 4.8, the P and AT points show a significant drift between 601 sites down to experimentally relevant sizes like 61 sites. Extrapolating from these results, our $L \rightarrow \infty$ estimate of the P point is $(\Delta/\Omega, \mathcal{R}_b) \simeq (1.951, 2.203)$ and of the AT point is $(\Delta/\Omega, \mathcal{R}_b) \simeq (2.357, 3.214)$. Consistently, we observe that the ordered lobes start at larger Δ/Ω with increasing size. The finite-size drift of the ordered lobes posed a problem when trying to overlap the floating phase boundaries from Ref. [159] (an infinite-size result) with our $L = 121$ ordered lobes. The floating phase had to be slightly shifted towards lower Δ/Ω by matching the tips of the ordered lobes on both phase diagrams, otherwise the $1/5$ lobe would not have been fully covered by the floating phase.

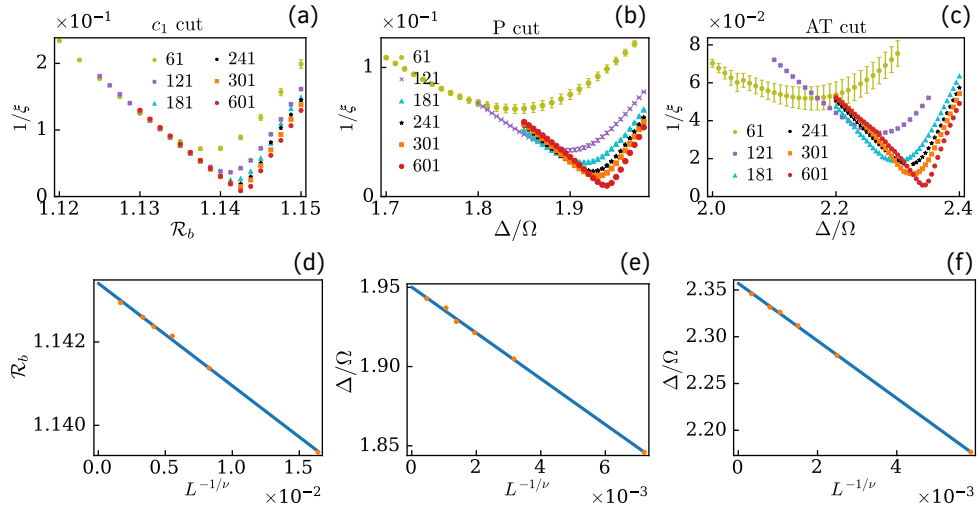


Figure 4.8: Finite size scaling analysis along the c_1 (Ising), P, and AT cuts. Top panels: inverse correlation length for several system sizes along the cuts. Bottom panels: finite-size scaling of the size-dependent critical points, where $\nu = 1, 3/5, 0.80$, for c_1 , P, and AT respectively. The $L \rightarrow \infty$ limits lead to $\mathcal{R}_b = 1.1434$ for c_1 , $\Delta/\Omega = 1.951$ for P, $\Delta/\Omega = 2.357$ for AT.

4.4.9 Floating phase boundary Our attempts of replicating the infinite DMRG floating phase boundaries [159] with the $L = 121$ data used in the rest of the phase diagram (Fig. 4.1) failed dramatically, which is why we decided to instead sketch this phase based on those results, which for that matter were more accurate. According to that study, there is no floating phase around the tips of the period-4 and period-3 phase, and a floating phase was only observed beyond $\Delta/\Omega \simeq 24$ below the period-3 phase.

Note that the "Lifshitz" points in the phase diagrams, that is, the points where we connect floating, ordered and disordered phases, are just a necessity of representing smooth phase transition lines, they are not an accurate physical estimate. While our results suggest the existence of such points, they have not been determined accurately.

Central charge In a first attempt, we tried to determine the boundary through the central charge: The floating phase is in the Luttinger liquid [177, 178] universality class with central charge $c = 1$. We obtained the central charge numerically by fitting the entanglement entropy S_l arising from the Schmidt decomposition of the state at a bond l . We fit S_l in a small interval in the middle of the chain with the Calabrese-Cardy formula for the entanglement

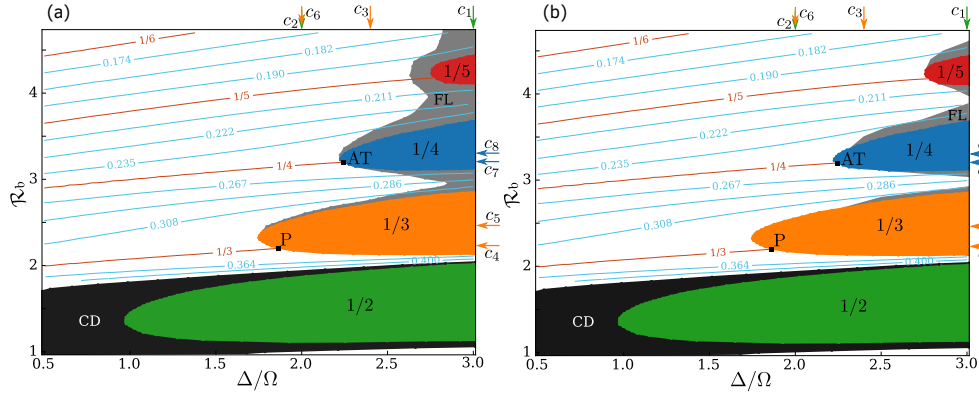


Figure 4.9: Phase diagrams where the floating phase boundary was determined (a) by a central charge criteria: along several cuts, we interpolate to find the point where c reaches the value of 1. (b) from the correlation length.

entropy with open boundary conditions [170]:

$$S_I = \frac{c}{6} \log \left(\frac{L}{2\pi} \sin \frac{\pi l}{L} \right) + g, \quad (4.37)$$

where g is a system-dependent constant. The resulting phase diagram is shown in Fig. 4.9(a). As we can see, the resulting floating phase is significantly overestimated. The ID to floating transition lines were obtained by interpolation of the central charge on a finite grid to determine where it reaches the value of 1. The line was then smoothed to remove nonphysical oscillations. This criteria was used because simulations which were beyond this limit (so supposedly inside the floating phase) often reached values of c much bigger than 1. While the entanglement entropy had properly converged in terms of D , the profile of S_I seemed unphysical: Such large values of c would always come paired with negative values of the constant g such that the fit of S_I becomes negative at some point inside the chain. Fitting S_I properly was also a challenge: On one side, the presence of Friedel oscillations in the entanglement entropy encourages us to widen the interval of points used in the fit so as to average out the oscillations, but the interval where the proper scaling is observed is very small so c will artificially grow as we include more points, so it was not possible to determine the floating phase boundary with these data.

As an aside, there were also attempts to determine the central charge of the critical P and AT points. Along these cuts, it was observed that the fitted central charge decreased monotonically across the phase boundary, being the largest on the disordered side and missing the expected values at the

critical point estimates derived from the correlation length. There were some efforts to justify reaching the expected value somewhere inside the ordered phases, by checking if the scaling dimension of the local order parameter also reached the expected value at that point, but this was found not to be true. Instead of the inconclusive central charge results, we presented the order parameter scaling as further proof of the claimed critical nature.

Correlation length In a second attempt, we estimated the floating phase boundary through the correlation length. As can be noted with cuts c_5 , c_6 , and c_8 , ξ tends to increase quickly and then plateau at some value. We considered several horizontal cuts and qualitatively estimated the beginning of a floating when a sharp increase in ξ was found. This resulted in the boundaries shown in Fig. 4.9(b). While still overestimating the size of the floating phase, these boundaries are much closer to what is shown in Fig. 4.1. However, a floating phase covering the $1/5$ lobe could not be differentiated using the $L = 121$ data, so this approach was also scrapped.

4.5 Comparing with previous work Finally, we discuss our results in the context of the Rydberg experiments which motivated this work and of other recent numerical work.

Our $q = 1/3$ results are in qualitative agreement with the $r = 2$ blockade model results [152] up to one point: we have not found evidence of a floating phase below the P point, although we expect a floating phase of significant width to appear at large Δ/Ω . If cut c_3 is indeed chiral, then the lower part of the $1/3$ lobe would prove to be the most numerically accessible chiral region of the phase diagram, and ideal to further explore the chiral universality class. Moreover, cut c_3 is remarkably far from the Potts point on the scale of the phase diagram of Fig. 4.1, leaving a significant parameter range to probe the chiral universality class experimentally.

On its own, the detection of a 3-state Potts universality class along the P cut is already an indication that the P point should be flanked by chiral transitions: If the P point is Potts, then the period-3 to IC transition should be in the $p = 3$ CCM universality class, and as we have seen already, existing evidence supports chiral transitions surrounding the Potts point of the $p = 3$ CCM.

A similar argument applies for the AT point: Assuming an AT universality class, a critical exponent $\nu \simeq 0.80$ corresponds to a λ coupling of the AT model of 0.5. This represents a slight shift with respect to the exponent $\nu \simeq 0.78$ ($\lambda \simeq 0.57$) found in the $p = 4$ blockade model at larger system sizes [160],

although it is still unclear whether this shift is within our error bars or if there is a discrepancy between the models. Nevertheless, $\lambda \simeq 0.5$ is still inside the range $0.42 \lesssim \lambda \lesssim 0.978$ where the chiral perturbation is relevant and where we might expect chiral lines to surround the conformal point [156].

4.5.1 The Kibble-Zurek exponent In the Rydberg atom experiments on chains of 51 atoms [76], the experimentally accessible quantity related to the IC-C transitions is the Kibble-Zurek (KZ) exponent μ [130, 131, 132], which was probed dynamically by ramping through the transition along specific cuts, in a range of \mathcal{R}_b which includes the P and AT points. For infinite systems, the KZ exponent is related to the correlation length exponent ν by $\mu = \nu/(1 + z\nu)$, where z is the dynamical critical exponent relating the time and spatial characteristic lengths ($\tau \sim \xi^z$). The experimental value of the KZ exponent, which controls the power-law increase of the domain size with the sweeping rate, was measured at around $\mu \simeq 0.38$ across the period-3 phase and $\mu \simeq 0.25$ for the period-4 phase. TEBD simulations complementing the experiments reported values of around $\mu \simeq 0.45$ for period-3 and $\mu \simeq 0.3 - 0.4$ for period-4 [76]. The exponent μ remained fairly independent from \mathcal{R}_b across the phase boundary close to the tips of the lobes.

The exponent $\mu \simeq 0.25$, found for the period-4 phase experimentally, can be regarded as a lower bound on the KZ exponent since it coincides with the exponent of a dynamical driving across a PT transition ($\nu' = 0.5$, $z = 2$), although the system, coming from smaller Δ/Ω , would cross first a floating phase.

On our side, we can determine the KZ exponent at the conformal points P and AT where the dynamical exponent z is fixed to 1, but along the chiral lines this exponent is not known, and an accurate estimate of its value along those lines is beyond what we could achieve numerically. To fully determine the chiral universality class, one will also need an estimate of the exponent z , along with another static critical exponent like, for example, the specific heat exponent α , which could be determined from the second derivative of the ground state energy with respect to the coupling driving the transition.

To determine z along the chiral line, one can complement the dynamical approaches which return μ with accurate numerical measurements of ν , but the current dynamical results are not sufficient for this purpose: The KZ exponent of the Potts point can be determined exactly, $\mu = 5/11 \simeq 0.4545$, while for the AT point we have found an exponent $\nu \simeq 0.80$ leading to $\mu \simeq 0.444$. While the TEBD values are comparatively close [76], the experimental values are significantly smaller.

Attributing this discrepancy to finite-size limitations on the experimental side, we suggest that new KZ experiments should be carried out, using the conformal cuts P and AT determined here as benchmarks along which one should find the predicted KZ exponents for sufficiently large system sizes. Then, a comparison between experimental values away from the conformal points and theoretical estimates of ν should allow one to reach precise estimates regarding the dynamical critical exponent.

Overall, we believe the picture on the IC-C transitions of the Rydberg model is much clearer now, even though it is still incomplete regarding the chiral universality class. It is also unclear how the exponent ν varies along the chiral line, or if it converges or not to the expected PT value of 0.5 as we get closer to the Lifshitz point, the location of which is also unknown. The numerical work on the $r = 2$ blockade model [152] suggests that there is a discontinuity or at least a sharp decrease of ν close to the Lifshitz point, in which case the Lifshitz point might be easier to locate. Work is in progress to refine our estimates of the exponent ν all along the boundary of the period-3 and period-4 phases where the transition is believed to be chiral, and possibly a first estimate of the location of the Lifshitz points could be achieved.

Chapter 5

Future work

Apart from what has already been mentioned throughout this thesis, some other work developed during this time was left unfinished and some ideas are still to be explored. We recap here some of these ideas and make some initial observations, when applicable.

Level crossings and edge Majoranas Given the interpretation of the level crossings in the Majorana picture, it was our initial intention to explore other systems with topologically protected edge modes which could show similar behavior in the oscillations of its energy. Topologically protected phases are not limited to a single edge mode: Adding next-neighbor couplings to the Kitaev chain already generates a phase with two Majoranas at the edge [179, 180, 181], for example. It would be interesting to note if these edge Majoranas also show oscillations for a finite-size in certain regions of the two-Majorana phase, and it is not clear a priori whether or not the oscillations of the Majoranas would be correlated between them, or if an effective interaction between them turns the level crossings into avoided crossings, thus removing all finite-size exact zeros. If the Majoranas are instead independent of each other, then it is possible that they could be described by the two-level degenerate perturbation theory developed in Chapter 3.

Level crossings and Floquet Majoranas The same type of questions were under investigation on a related Floquet system: a driven Kitaev chain where the chemical potential spikes periodically as a Dirac-delta [182, 183]. Floquet systems are typically characterized by the periodic eigenspectrum of its evolution operator (quasienergies), and this system in particular features topological phases of increasing number of zero-quasienergy Majoranas as one increases the period and the area of the spike. It was shown how the heat transfer to a thermal bath through the edges of the chain is sensitive to the different topological phases [184]. It was not clear how having many Majoranas could influence the autocorrelation time, which was of special interest to us at the time. We found that it was not simple to find parameter regimes on

which to study these questions properly, as some edge Majoranas only seem to appear for very large system sizes – since one is only guaranteed to have the expected number of zero quasienergies in the thermodynamic limit – while the quasienergy of the Majorana adiabatically connected to the static zero energy Majorana decays exponentially with system size. Moreover, it seems that not all Majoranas are exponentially located at the edge, with some showing a maxima of their wavefunction away from the edge, which could be interpreted as a repulsion between the edge Majoranas, although it could also be a size-dependent result.

Interestingly, a symmetry property of the model was noted that could explain the emergence of the edge Majoranas in the Brillouin zone boundaries of the quasienergies, the so-called π -Majoranas [182], which we believe is not known in the literature as it was new to our collaborators. Otherwise, a relation seems to exist between the Majorana fermions of zero quasienergy in driven Kitaev models and in Kitaev models with longer range-interactions, both models having phases with more than one Majorana at each edge, and a BCH series expansion of the Floquet Hamiltonian suggests that the driving induces effective long-range interactions, so it might be more feasible to instead focus on long-range Kitaev models in the future.

Extensions of the tunneling amplitude method The study of the effects of disorder on the tunneling amplitude could be expanded beyond drift effects on the level crossings, as one could numerically simulate stochasticity on the perturbative couplings entering the recursion relations. More generally, the method could become a framework on which to study a variety of spatially-dependant systems: In our focus on demonstrating the method on models where one can extract exact results, one might miss the point that the recursion relations at the basis of the method are simple enough that one can easily implement them numerically, in particular in 1D, so that more general models with, for example, more complicated spatial anisotropy, spatially modulated magnetic fields, or random couplings, are very much accessible. Otherwise, some other possible fields of application of the method have already been mentioned (Sec. 3.8).

Rydberg atoms As we have already discussed, the next steps in the investigation of the Rydberg incommensurate-commensurate transitions is clear, as the chiral universality class is left to be completely studied, followed by the location and characterization of the Lifshitz points. We have pointed out especially to the lower part of the $1/3$ ordered lobe which has proved to be the

most accessible chiral region, both experimentally due to its length, and numerically due to the lower computational complexity that is apparent in this region.

The numerical determination of other critical exponents along the chiral lines but also across the conformal points would be a useful self-consistent check of our results. There is still a big room for improvement in our simulations as our attempts at determining the central charge or other critical exponents were unsuccessful, except for the determination of β at the conformal points. Time-evolving MPS methods could be used to more closely simulate the experimental setup and directly probe the dynamical and Kibble-Zurek exponents, with some similar numerics having been done recently [185], in this case using ED.

It could also prove interesting to carry out the same numerical study done here in the case of other Rydberg-Rydberg power-law interactions, in particular r^{-3} which can be relevant experimentally as it is accessible with Rydberg atoms, but one could also look at other exponents in order to understand the change of the critical exponents (or lack of it) as one approaches the limit cases of the blockade models ($\sim r^{-\infty}$) and the Coulomb potential. While in general one could expect no significant change with respect to what we observed, the tendency in the case of the $p = 4$ conformal universality class seems to be an increase of the Ashkin-Teller coupling λ as we move towards the blockade model, given the estimates $\lambda \simeq 0.5$ for r^{-6} and $\lambda \simeq 0.57$ for the blockade model [160], so it is a possibility that the chiral regime of the $p = 4$ case disappears at a smaller power-law exponent, linked to a decrease of the λ coupling beyond the limit $\lambda \lesssim 0.42$ ($\nu \gtrsim 0.82$) where a chiral regime is expected to exist [156]. A change in the $p = 3$ universality class, however, seems highly unlikely.

Bibliography

- [1] I. A. Maceira and F. Mila, “Infinite coherence time of edge spins in finite-length chains,” *Phys. Rev. B*, vol. 97, p. 064424, Feb 2018.
- [2] I. A. Maceira, F. Mila, and M. Müller, “Perturbative approach to tunneling and quantum interferences in spin clusters,” *Phys. Rev. B*, vol. 101, p. 104416, Mar 2020.
- [3] I. A. Maceira, N. Chepiga, and F. Mila, “Conformal and chiral phase transitions in rydberg chains,” *arXiv*, 2022.
- [4] E. Ising, “Beitrag zur theorie des ferromagnetismus,” *Zeitschrift für Physik*, vol. 31, pp. 253–258, Feb 1925.
- [5] L. Onsager, “Crystal statistics. i. a two-dimensional model with an order-disorder transition,” *Phys. Rev.*, vol. 65, pp. 117–149, Feb 1944.
- [6] L. P. Kadanoff, “Scaling laws for ising models near T_c ,” *Physics Physique Fizika*, vol. 2, pp. 263–272, Jun 1966.
- [7] K. G. Wilson, “Renormalization group and critical phenomena. i. renormalization group and the kadanoff scaling picture,” *Phys. Rev. B*, vol. 4, pp. 3174–3183, Nov 1971.
- [8] J. M. Yeomans, *Statistical mechanics of phase transitions / J.M. Yeomans*. Oxford science publications, Oxford [England: Clarendon Press, 1992.
- [9] M. E. Fisher, “Renormalization group theory: Its basis and formulation in statistical physics,” *Rev. Mod. Phys.*, vol. 70, pp. 653–681, Apr 1998.
- [10] A. M. Polyakov, “Conformal symmetry of critical fluctuations,” *JETP Lett.*, vol. 12, pp. 381–383, 1970.

- [11] A. Belavin, A. Polyakov, and A. Zamolodchikov, "Infinite conformal symmetry in two-dimensional quantum field theory," *Nuclear Physics B*, vol. 241, no. 2, pp. 333–380, 1984.
- [12] V. Dotsenko and V. Fateev, "Operator algebra of two-dimensional conformal theories with central charge $c = 1$," *Physics Letters B*, vol. 154, no. 4, pp. 291–295, 1985.
- [13] D. Friedan, Z. Qiu, and S. Shenker, "Conformal invariance, unitarity, and critical exponents in two dimensions," *Phys. Rev. Lett.*, vol. 52, pp. 1575–1578, Apr 1984.
- [14] V. S. Dotsenko, "Critical behavior and associated conformal algebra of the z_3 potts model," *Journal of Statistical Physics*, vol. 34, pp. 781–791, Mar 1984.
- [15] S. El-Showk, M. F. Paulos, D. Poland, S. Rychkov, D. Simmons-Duffin, and A. Vichi, "Solving the 3d ising model with the conformal bootstrap," *Phys. Rev. D*, vol. 86, p. 025022, Jul 2012.
- [16] S. El-Showk, M. F. Paulos, D. Poland, S. Rychkov, D. Simmons-Duffin, and A. Vichi, "Solving the 3d ising model with the conformal bootstrap ii. c-minimization and precise critical exponents," *Journal of Statistical Physics*, vol. 157, pp. 869–914, Dec 2014.
- [17] J. M. Kosterlitz and D. J. Thouless, "Ordering, metastability and phase transitions in two-dimensional systems," *Journal of Physics C: Solid State Physics*, vol. 6, p. 1181–1203, Apr 1973.
- [18] J. M. Kosterlitz, "The critical properties of the two-dimensional xy model," *Journal of Physics C: Solid State Physics*, vol. 7, p. 1046–1060, Mar 1974.
- [19] F. Haldane, "Continuum dynamics of the 1-d heisenberg antiferromagnet: Identification with the $o(3)$ nonlinear sigma model," *Physics Letters A*, vol. 93, p. 464–468, Feb 1983.
- [20] I. Affleck, T. Kennedy, E. H. Lieb, and H. Tasaki, "Rigorous results on valence-bond ground states in antiferromagnets," *Physical Review Letters*, vol. 59, p. 799–802, Aug 1987.
- [21] T. Kennedy and H. Tasaki, "Hidden symmetry breaking and the haldane phase in $s = 1$ quantum spin chains," *Communications in Mathematical Physics*, vol. 147, pp. 431–484, Jul 1992.

- [22] M. den Nijs and K. Rommelse, “Preroughening transitions in crystal surfaces and valence-bond phases in quantum spin chains,” *Phys. Rev. B*, vol. 40, pp. 4709–4734, Sep 1989.
- [23] F. Pollmann, E. Berg, A. M. Turner, and M. Oshikawa, “Symmetry protection of topological phases in one-dimensional quantum spin systems,” *Phys. Rev. B*, vol. 85, p. 075125, Feb 2012.
- [24] J. Zak, “Berry’s phase for energy bands in solids,” *Phys. Rev. Lett.*, vol. 62, pp. 2747–2750, Jun 1989.
- [25] F. D. M. Haldane, “Berry curvature on the fermi surface: Anomalous hall effect as a topological fermi-liquid property,” *Phys. Rev. Lett.*, vol. 93, p. 206602, Nov 2004.
- [26] L. Li, C. Yang, and S. Chen, “Winding numbers of phase transition points for one-dimensional topological systems,” *EPL (Europhysics Letters)*, vol. 112, p. 10004, oct 2015.
- [27] R. S. K. Mong and V. Shivamoggi, “Edge states and the bulk-boundary correspondence in dirac hamiltonians,” *Phys. Rev. B*, vol. 83, p. 125109, Mar 2011.
- [28] J. K. Asbóth, L. Oroszlány, and A. Pályi, “A short course on topological insulators,” *Lecture Notes in Physics*, 2016.
- [29] P. Pfeuty, “The one-dimensional ising model with a transverse field,” *Annals of Physics*, vol. 57, p. 79–90, Mar 1970.
- [30] S. L. Sondhi, S. M. Girvin, J. P. Carini, and D. Shahar, “Continuous quantum phase transitions,” *Rev. Mod. Phys.*, vol. 69, pp. 315–333, Jan 1997.
- [31] S. Sachdev, *Quantum Phase Transitions*. Cambridge University Press, 2 ed., 2011.
- [32] A. Y. Kitaev, “Unpaired majorana fermions in quantum wires,” *Physics-Uspekhi*, vol. 44, p. 131–136, Oct 2001.
- [33] G. Binnig, H. Rohrer, C. Gerber, and E. Weibel, “Tunneling through a controllable vacuum gap,” *Applied Physics Letters*, vol. 40, no. 2, pp. 178–180, 1982.

- [34] G. Binnig, H. Rohrer, C. Gerber, and E. Weibel, "Surface studies by scanning tunneling microscopy," *Phys. Rev. Lett.*, vol. 49, pp. 57–61, Jul 1982.
- [35] H.-W. Fink, "Mono-atomic tips for scanning tunneling microscopy," *IBM J. Res. Dev.*, vol. 30, pp. 460–465, 1986.
- [36] D. M. Eigler and E. K. Schweizer, "Positioning single atoms with a scanning tunnelling microscope," *Nature*, vol. 344, pp. 524–526, Apr 1990.
- [37] M. F. Crommie, C. P. Lutz, and D. M. Eigler, "Confinement of electrons to quantum corrals on a metal surface," *Science*, vol. 262, no. 5131, pp. 218–220, 1993.
- [38] A. A. Khajetoorians, D. Wegner, A. F. Otte, and I. Swart, "Creating designer quantum states of matter atom-by-atom," *Nature Reviews Physics*, vol. 1, p. 703–715, Sep 2019.
- [39] R. Wiesendanger, H.-J. Güntherodt, G. Güntherodt, R. J. Gambino, and R. Ruf, "Observation of vacuum tunneling of spin-polarized electrons with the scanning tunneling microscope," *Phys. Rev. Lett.*, vol. 65, pp. 247–250, Jul 1990.
- [40] S. Heinze, M. Bode, A. Kubetzka, O. Pietzsch, X. Nie, S. Blügel, and R. Wiesendanger, "Real-space imaging of two-dimensional anti-ferromagnetism on the atomic scale," *Science*, vol. 288, no. 5472, pp. 1805–1808, 2000.
- [41] A. J. Heinrich, J. A. Gupta, C. P. Lutz, and D. M. Eigler, "Single-atom spin-flip spectroscopy," *Science*, vol. 306, no. 5695, pp. 466–469, 2004.
- [42] R. Toskovic, R. van den Berg, A. Spinelli, I. S. Eliens, B. van den Toorn, B. Bryant, J.-S. Caux, and A. F. Otte, "Atomic spin-chain realization of a model for quantum criticality," *Nature Physics*, vol. 12, p. 656–660, Apr 2016.
- [43] J. Tersoff and D. R. Hamann, "Theory and application for the scanning tunneling microscope," *Phys. Rev. Lett.*, vol. 50, pp. 1998–2001, Jun 1983.
- [44] G. Binnig, C. F. Quate, and C. Gerber, "Atomic force microscope," *Phys. Rev. Lett.*, vol. 56, pp. 930–933, Mar 1986.

- [45] F. Ohnesorge and G. Binnig, "True atomic resolution by atomic force microscopy through repulsive and attractive forces," *Science*, vol. 260, no. 5113, pp. 1451–1456, 1993.
- [46] P. K. Hansma, V. B. Elings, O. Marti, and C. E. Bracker, "Scanning tunneling microscopy and atomic force microscopy: Application to biology and technology," *Science*, vol. 242, no. 4876, pp. 209–216, 1988.
- [47] S.-W. Hla, "Scanning tunneling microscopy single atom/molecule manipulation and its application to nanoscience and technology," *Journal of Vacuum Science & Technology B: Microelectronics and Nanometer Structures Processing, Measurement, and Phenomena*, vol. 23, no. 4, pp. 1351–1360, 2005.
- [48] R. Garcia, A. W. Knoll, and E. Riedo, "Advanced scanning probe lithography," *Nature Nanotechnology*, vol. 9, pp. 577–587, Aug 2014.
- [49] E. Meyer, H. J. Hug, R. Bennewitz, *et al.*, *Scanning probe microscopy*, vol. 4. Springer, 2003.
- [50] C. Chen, *Introduction to scanning tunneling microscopy*. Oxford: Oxford University Press, 2021.
- [51] A. A. Khajetoorians, J. Wiebe, B. Chilian, and R. Wiesendanger, "Realizing all-spin-based logic operations atom by atom," *Science*, vol. 332, p. 1062–1064, May 2011.
- [52] A. Ashkin, "Acceleration and trapping of particles by radiation pressure," *Phys. Rev. Lett.*, vol. 24, pp. 156–159, Jan 1970.
- [53] A. Ashkin, J. M. Dziedzic, J. E. Bjorkholm, and S. Chu, "Observation of a single-beam gradient force optical trap for dielectric particles," *Opt. Lett.*, vol. 11, pp. 288–290, May 1986.
- [54] M. Dienerowitz, M. Mazilu, and K. Dholakia, "Optical manipulation of nanoparticles: a review," *Journal of Nanophotonics*, vol. 2, no. 1, pp. 1 – 32, 2008.
- [55] S. Chu, L. Hollberg, J. E. Bjorkholm, A. Cable, and A. Ashkin, "Three-dimensional viscous confinement and cooling of atoms by resonance radiation pressure," *Phys. Rev. Lett.*, vol. 55, pp. 48–51, Jul 1985.
- [56] S. Chu, J. E. Bjorkholm, A. Ashkin, and A. Cable, "Experimental observation of optically trapped atoms," *Phys. Rev. Lett.*, vol. 57, pp. 314–317, Jul 1986.

- [57] P. D. Lett, R. N. Watts, C. I. Westbrook, W. D. Phillips, P. L. Gould, and H. J. Metcalf, "Observation of atoms laser cooled below the doppler limit," *Phys. Rev. Lett.*, vol. 61, pp. 169–172, Jul 1988.
- [58] E. L. Raab, M. Prentiss, A. Cable, S. Chu, and D. E. Pritchard, "Trapping of neutral sodium atoms with radiation pressure," *Phys. Rev. Lett.*, vol. 59, pp. 2631–2634, Dec 1987.
- [59] V. I. Balykin, V. G. Minogin, and V. S. Letokhov, "Electromagnetic trapping of cold atoms," *Reports on Progress in Physics*, vol. 63, pp. 1429–1510, aug 2000.
- [60] M. H. Anderson, J. R. Ensher, M. R. Matthews, C. E. Wieman, and E. A. Cornell, "Observation of bose-einstein condensation in a dilute atomic vapor," *Science*, vol. 269, no. 5221, pp. 198–201, 1995.
- [61] K. B. Davis, M. O. Mewes, M. R. Andrews, N. J. van Druten, D. S. Durfee, D. M. Kurn, and W. Ketterle, "Bose-einstein condensation in a gas of sodium atoms," *Phys. Rev. Lett.*, vol. 75, pp. 3969–3973, Nov 1995.
- [62] N. Schlosser, G. Reymond, and P. Grangier, "Collisional blockade in microscopic optical dipole traps," *Phys. Rev. Lett.*, vol. 89, p. 023005, Jun 2002.
- [63] T. F. Gallagher, *Rydberg Atoms*. Cambridge Monographs on Atomic, Molecular and Chemical Physics, Cambridge University Press, 1994.
- [64] E. Urban, T. A. Johnson, T. Henage, L. Isenhower, D. D. Yavuz, T. G. Walker, and M. Saffman, "Observation of rydberg blockade between two atoms," *Nature Physics*, vol. 5, pp. 110–114, Feb 2009.
- [65] A. Gaëtan, Y. Miroshnychenko, T. Wilk, A. Chotia, M. Viteau, D. Comparat, P. Pillet, A. Browaeys, and P. Grangier, "Observation of collective excitation of two individual atoms in the rydberg blockade regime," *Nature Physics*, vol. 5, pp. 115–118, Feb 2009.
- [66] D. Jaksch, J. I. Cirac, P. Zoller, S. L. Rolston, R. Côté, and M. D. Lukin, "Fast quantum gates for neutral atoms," *Phys. Rev. Lett.*, vol. 85, pp. 2208–2211, Sep 2000.
- [67] M. D. Lukin, M. Fleischhauer, R. Cote, L. M. Duan, D. Jaksch, J. I. Cirac, and P. Zoller, "Dipole blockade and quantum information processing in mesoscopic atomic ensembles," *Phys. Rev. Lett.*, vol. 87, p. 037901, Jun 2001.

- [68] M. Saffman, T. G. Walker, and K. Mølmer, “Quantum information with rydberg atoms,” *Rev. Mod. Phys.*, vol. 82, pp. 2313–2363, Aug 2010.
- [69] A. Browaeys and T. Lahaye, “Many-body physics with individually controlled rydberg atoms,” *Nature Physics*, vol. 16, p. 132–142, Jan 2020.
- [70] J. M. Raimond, G. Vitrant, and S. Haroche, “Spectral line broadening due to the interaction between very excited atoms: ‘the dense rydberg gas’,” *Journal of Physics B: Atomic and Molecular Physics*, vol. 14, pp. L655–L660, nov 1981.
- [71] M. Endres, H. Bernien, A. Keesling, H. Levine, E. R. Anschuetz, A. Krajenbrink, C. Senko, V. Vuletic, M. Greiner, and M. D. Lukin, “Atom-by-atom assembly of defect-free one-dimensional cold atom arrays,” *Science*, vol. 354, no. 6315, pp. 1024–1027, 2016.
- [72] F. Nogrette, H. Labuhn, S. Ravets, D. Barredo, L. Béguin, A. Vernier, T. Lahaye, and A. Browaeys, “Single-atom trapping in holographic 2d arrays of microtraps with arbitrary geometries,” *Phys. Rev. X*, vol. 4, p. 021034, May 2014.
- [73] D. Barredo, S. de Léséleuc, V. Lienhard, T. Lahaye, and A. Browaeys, “An atom-by-atom assembler of defect-free arbitrary two-dimensional atomic arrays,” *Science*, vol. 354, no. 6315, pp. 1021–1023, 2016.
- [74] H. Weimer, M. Müller, I. Lesanovsky, P. Zoller, and H. P. Büchler, “A rydberg quantum simulator,” *Nature Physics*, vol. 6, pp. 382–388, May 2010.
- [75] H. Bernien, S. Schwartz, A. Keesling, H. Levine, A. Omran, H. Pichler, S. Choi, A. S. Zibrov, M. Endres, M. Greiner, and et al., “Probing many-body dynamics on a 51-atom quantum simulator,” *Nature*, vol. 551, p. 579–584, Nov 2017.
- [76] A. Keesling, A. Omran, H. Levine, H. Bernien, H. Pichler, S. Choi, R. Samajdar, S. Schwartz, P. Silvi, S. Sachdev, and et al., “Quantum kibble–zurek mechanism and critical dynamics on a programmable rydberg simulator,” *Nature*, vol. 568, p. 207–211, Apr 2019.
- [77] D. A. Huse and M. E. Fisher, “Domain walls and the melting of commensurate surface phases,” *Physical Review Letters*, vol. 49, p. 793–796, Sep 1982.

- [78] P. Scholl, M. Schuler, H. J. Williams, A. A. Eberharter, D. Barredo, K.-N. Schymik, V. Lienhard, L.-P. Henry, T. C. Lang, T. Lahaye, A. M. Läuchli, and A. Browaeys, “Quantum simulation of 2d antiferromagnets with hundreds of rydberg atoms,” *Nature*, vol. 595, pp. 233–238, Jul 2021.
- [79] S. Ebadi, T. T. Wang, H. Levine, A. Keesling, G. Semeghini, A. Omran, D. Bluvstein, R. Samajdar, H. Pichler, W. W. Ho, S. Choi, S. Sachdev, M. Greiner, V. Vuletić, and M. D. Lukin, “Quantum phases of matter on a 256-atom programmable quantum simulator,” *Nature*, vol. 595, pp. 227–232, Jul 2021.
- [80] G. Vionnet, B. Kumar, and F. Mila, “Level crossings induced by a longitudinal coupling in the transverse field ising chain,” *Physical Review B*, vol. 95, May 2017.
- [81] J. Kemp, N. Y. Yao, C. R. Laumann, and P. Fendley, “Long coherence times for edge spins,” *Journal of Statistical Mechanics: Theory and Experiment*, vol. 2017, p. 063105, Jun 2017.
- [82] D. Gatteschi and R. Sessoli, “Quantum tunneling of magnetization and related phenomena in molecular materials,” *Angewandte Chemie International Edition*, vol. 42, p. 268–297, Jan 2003.
- [83] W. Wernsdorfer and R. Sessoli, “Quantum phase interference and parity effects in magnetic molecular clusters,” *Science*, vol. 284, no. 5411, pp. 133–135, 1999.
- [84] A. Garg, “Topologically quenched tunnel splitting in spin systems without kramers’ degeneracy,” *Europhysics Letters (EPL)*, vol. 22, p. 205–210, Apr 1993.
- [85] D. V. Dmitriev, V. Y. Krivnov, and A. A. Ovchinnikov, “Gap generation in the xxz model in a transverse magnetic field,” *Physical Review B*, vol. 65, Apr 2002.
- [86] S. D. Sarma, M. Freedman, and C. Nayak, “Majorana zero modes and topological quantum computation,” *npj Quantum Information*, vol. 1, Oct 2015.
- [87] E. Barouch, B. M. McCoy, and M. Dresden, “Statistical mechanics of the xy model. i,” *Physical Review A*, vol. 2, p. 1075–1092, Sep 1970.

- [88] E. Barouch and B. M. McCoy, “Statistical mechanics of the xy model. ii. spin-correlation functions,” *Physical Review A*, vol. 3, p. 786–804, Feb 1971.
- [89] E. Barouch and B. M. McCoy, “Statistical mechanics of the xy model. iii,” *Physical Review A*, vol. 3, p. 2137–2140, Jun 1971.
- [90] B. M. McCoy, E. Barouch, and D. B. Abraham, “Statistical mechanics of the xy model. iv. time-dependent spin-correlation functions,” *Physical Review A*, vol. 4, p. 2331–2341, Dec 1971.
- [91] S. Katsura, “Statistical mechanics of the anisotropic linear heisenberg model,” *Physical Review*, vol. 127, p. 1508–1518, Sep 1962.
- [92] P. Ruján, “Critical behavior of two-dimensional models with spatially modulated phases: Analytic results,” *Physical Review B*, vol. 24, p. 6620–6631, Dec 1981.
- [93] A. Dutta, G. Aeppli, B. K. Chakrabarti, U. Divakaran, T. F. Rosenbaum, and D. Sen, *Quantum Phase Transitions in Transverse Field Spin Models: From Statistical Physics to Quantum Information*. Cambridge University Press, 2015.
- [94] P. Fendley, “Strong zero modes and eigenstate phase transitions in the xyz/interacting majorana chain,” *Journal of Physics A: Mathematical and Theoretical*, vol. 49, p. 30LT01, Jun 2016.
- [95] D. V. Else, P. Fendley, J. Kemp, and C. Nayak, “Prethermal strong zero modes and topological qubits,” *Physical Review X*, vol. 7, Dec 2017.
- [96] D. A. Abanin, W. De Roeck, W. W. Ho, and F. Huveneers, “Effective hamiltonians, prethermalization, and slow energy absorption in periodically driven many-body systems,” *Physical Review B*, vol. 95, Jan 2017.
- [97] D. Abanin, W. De Roeck, W. W. Ho, and F. Huveneers, “A rigorous theory of many-body prethermalization for periodically driven and closed quantum systems,” *Communications in Mathematical Physics*, vol. 354, p. 809–827, Jun 2017.
- [98] E. Lieb, T. Schultz, and D. Mattis, “Two soluble models of an antiferromagnetic chain,” *Annals of Physics*, vol. 16, no. 3, pp. 407–466, 1961.
- [99] A. J. Leggett, S. Chakravarty, A. T. Dorsey, M. P. A. Fisher, A. Garg, and W. Zwerger, “Dynamics of the dissipative two-state system,” *Reviews of Modern Physics*, vol. 59, p. 1–85, Jan 1987.

- [100] P. Politi, A. Rettori, F. Hartmann-Boutron, and J. Villain, "Tunneling in mesoscopic magnetic molecules," *Physical Review Letters*, vol. 75, p. 537–540, Jul 1995.
- [101] J. Van Hemmen and A. Sütö, "Tunneling of quantum spins," *Physica B+C*, vol. 141, no. 1, pp. 37–75, 1986.
- [102] J. L. v. Hemmen and A. Sütö, "Semiclassical quantization and resonance in spin tunnelling," *Journal of Physics A: Mathematical and General*, vol. 31, p. 10029–10043, Dec 1998.
- [103] M.ENZ and R. Schilling, "Magnetic field dependence of the tunnelling splitting of quantum spins," *Journal of Physics C: Solid State Physics*, vol. 19, p. L711–L715, Oct 1986.
- [104] E. M. Chudnovsky and L. Gunther, "Quantum tunneling of magnetization in small ferromagnetic particles," *Physical Review Letters*, vol. 60, p. 661–664, Feb 1988.
- [105] D. Loss, D. P. DiVincenzo, and G. Grinstein, "Suppression of tunneling by interference in half-integer-spin particles," *Physical Review Letters*, vol. 69, p. 3232–3235, Nov 1992.
- [106] J. von Delft and C. L. Henley, "Destructive quantum interference in spin tunneling problems," *Physical Review Letters*, vol. 69, p. 3236–3239, Nov 1992.
- [107] E. M. Chudnovsky, "Conservation of angular momentum in the problem of tunneling of the magnetic moment," *Physical Review Letters*, vol. 72, p. 3433–3436, May 1994.
- [108] D. Gatteschi, R. Sessoli, and J. Villain, *Molecular nanomagnets*. Oxford New York: Oxford University Press, 2006.
- [109] S. Loth, S. Baumann, C. P. Lutz, D. M. Eigler, and A. J. Heinrich, "Bistability in atomic-scale antiferromagnets," *Science*, vol. 335, p. 196–199, Jan 2012.
- [110] A. A. Khajetoorians, J. Wiebe, B. Chilian, S. Lounis, S. Blügel, and R. Wiesendanger, "Atom-by-atom engineering and magnetometry of tailored nanomagnets," *Nature Physics*, vol. 8, p. 497–503, Apr 2012.
- [111] O. O. Brovko, P. A. Ignatiev, V. S. Stepanyuk, and P. Bruno, "Tailoring exchange interactions in engineered nanostructures: An ab initio study," *Physical Review Letters*, vol. 101, Jul 2008.

- [112] I. Peschel and V. J. Emery, "Calculation of spin correlations in two-dimensional ising systems from one-dimensional kinetic models," *Zeitschrift für Physik B Condensed Matter*, vol. 43, p. 241–249, Sep 1981.
- [113] F. Hassler and D. Schuricht, "Strongly interacting majorana modes in an array of josephson junctions," *New Journal of Physics*, vol. 14, p. 125018, Dec 2012.
- [114] D. S. Fisher, "Critical behavior of random transverse-field ising spin chains," *Physical Review B*, vol. 51, p. 6411–6461, Mar 1995.
- [115] T. Kato, "On the convergence of the perturbation method. i," *Progress of Theoretical Physics*, vol. 4, p. 514–523, Dec 1949.
- [116] C. Bloch, "Sur la théorie des perturbations des états liés," *Nuclear Physics*, vol. 6, p. 329–347, Mar 1958.
- [117] V. L. Nguen, B. Z. Spivak, and B. I. Shklovskii, "Tunnel hopping in a disordered system," *Zhurnal Eksperimentalnoi i Teoreticheskoi Fiziki*, vol. 89, pp. 1770–1784, Nov. 1985.
- [118] V. L. Nguyen, B. Z. Spivak, and B. I. Shklovskii, "Aaronov-Bohm oscillations with normal and superconducting flux quanta in hopping conductivity," *ZhETF Pisma Redaktsiiu*, vol. 41, p. 35, Jan. 1985.
- [119] B. Shklovskii and B. Spivak, "Chapter 9 - scattering and interference effects in variable range hopping conduction," in *Hopping Transport in Solids* (M. Pollak and B. Shklovskii, eds.), vol. 28 of *Modern Problems in Condensed Matter Sciences*, pp. 271–348, Elsevier, 1991.
- [120] M. Kardar, *Statistical physics of fields*. Cambridge New York: Cambridge University Press, 2007.
- [121] U. Sivan, O. Entin-Wohlman, and Y. Imry, "Orbital magnetoconductance in the variable-range-hopping regime," *Physical Review Letters*, vol. 60, p. 1566–1569, Apr 1988.
- [122] H. L. Zhao, B. Z. Spivak, M. P. Gelfand, and S. Feng, "Negative magnetoresistance in variable-range-hopping conduction," *Physical Review B*, vol. 44, p. 10760–10767, Nov 1991.
- [123] S. V. Syzranov, A. Moor, and K. B. Efetov, "Strong quantum interference in strongly disordered bosonic insulators," *Physical Review Letters*, vol. 108, Jun 2012.

-
- [124] M. Müller, “Magnetoresistance and localization in bosonic insulators,” *EPL (Europhysics Letters)*, vol. 102, p. 67008, Jun 2013.
- [125] N. Chepiga and F. Mila, “Exact zero modes in frustrated haldane chains,” *Physical Review B*, vol. 96, Aug 2017.
- [126] N. Chepiga and F. Mila, “Rigorous decoupling between edge states in frustrated spin chains and ladders,” *Physical Review B*, vol. 97, May 2018.
- [127] M. A. Sørensen, U. B. Hansen, M. Perfetti, K. S. Pedersen, E. Bartolomé, G. G. Simeoni, H. Mutka, S. Rols, M. Jeong, I. Zivkovic, and et al., “Chemical tunnel-splitting-engineering in a dysprosium-based molecular nanomagnet,” *Nature Communications*, vol. 9, p. 1292, Mar 2018.
- [128] P. B. Chakraborty, P. Henelius, H. Kjønsberg, A. W. Sandvik, and S. M. Girvin, “Theory of the magnetic phase diagram of LiHoF_4 ,” *Physical Review B*, vol. 70, Oct 2004.
- [129] S. M. A. Tabei, M. J. P. Gingras, Y.-J. Kao, and T. Yavors’kii, “Perturbative quantum monte carlo study of LiHoF_4 in a transverse magnetic field,” *Physical Review B*, vol. 78, Nov 2008.
- [130] T. W. B. Kibble, “Topology of cosmic domains and strings,” *Journal of Physics A: Mathematical and General*, vol. 9, pp. 1387–1398, aug 1976.
- [131] W. H. Zurek, “Cosmological experiments in superfluid helium?,” *Nature*, vol. 317, pp. 505–508, Oct 1985.
- [132] W. H. Zurek, U. Dorner, and P. Zoller, “Dynamics of a quantum phase transition,” *Phys. Rev. Lett.*, vol. 95, p. 105701, Sep 2005.
- [133] D. L. Abernathy, S. Song, K. I. Blum, R. J. Birgeneau, and S. G. J. Mochrie, “Chiral melting of the $\text{Si}(113) (3 \times 1)$ reconstruction,” *Physical Review B*, vol. 49, p. 2691–2705, Jan 1994.
- [134] J. Schreiner, K. Jacobi, and W. Selke, “Experimental evidence for chiral melting of the $\text{Ge}(113)$ and $\text{Si}(113) 3 \times 1$ surface phases,” *Physical Review B*, vol. 49, p. 2706–2714, Jan 1994.
- [135] S. Ostlund, “Incommensurate and commensurate phases in asymmetric clock models,” *Physical Review B*, vol. 24, p. 398–405, Jul 1981.

- [136] D. A. Huse, "Simple three-state model with infinitely many phases," *Physical Review B*, vol. 24, p. 5180–5194, Nov 1981.
- [137] S. Elitzur, R. B. Pearson, and J. Shigemitsu, "Phase structure of discrete abelian spin and gauge systems," *Physical Review D*, vol. 19, p. 3698–3714, Jun 1979.
- [138] J. L. Cardy, "General discrete planar models in two dimensions: Duality properties and phase diagrams," *Journal of Physics A: Mathematical and General*, vol. 13, p. 1507–1515, Apr 1980.
- [139] V. L. Pokrovsky and A. L. Talapov, "Ground state, spectrum, and phase diagram of two-dimensional incommensurate crystals," *Physical Review Letters*, vol. 42, p. 65–67, Jan 1979.
- [140] D. A. Huse and M. E. Fisher, "Commensurate melting, domain walls, and dislocations," *Physical Review B*, vol. 29, p. 239–270, Jan 1984.
- [141] S. Ostlund, "Relation between lattice and continuum theories of two-dimensional solids," *Physical Review B*, vol. 23, p. 2235–2246, Mar 1981.
- [142] W. Selke and J. M. Yeomans, "A monte carlo study of the asymmetric clock or chiral potts model in two dimensions," *Zeitschrift fur Physik B Condensed Matter*, vol. 46, p. 311–318, Dec 1982.
- [143] D. A. Huse, A. M. Szpilka, and M. E. Fisher, "Melting and wetting transitions in the three-state chiral clock model," *Physica A: Statistical Mechanics and its Applications*, vol. 121, p. 363–398, Sep 1983.
- [144] H. J. Schulz, "Phase transitions in monolayers adsorbed on uniaxial substrates," *Physical Review B*, vol. 28, p. 2746–2749, Sep 1983.
- [145] S. Howes, L. P. Kadanoff, and M. Den Nijs, "Quantum model for commensurate-incommensurate transitions," *Nuclear Physics B*, vol. 215, p. 169–208, Jan 1983.
- [146] S. F. Howes, "Commensurate-incommensurate transitions and the lifshitz point in the quantum asymmetric clock model," *Physical Review B*, vol. 27, p. 1762–1768, Feb 1983.
- [147] W. Selke, "Monte carlo studies of interfacial adsorption in multi-state models," *Surface Science*, vol. 144, p. 176–181, Aug 1984.

- [148] G. Albertini, B. M. McCoy, and J. H. Perk, “Commensurate-incommensurate transition in the ground state of the superintegrable chiral potts model,” *Physics Letters A*, vol. 135, p. 159–166, Feb 1989.
- [149] P. Fendley, K. Sengupta, and S. Sachdev, “Competing density-wave orders in a one-dimensional hard-boson model,” *Physical Review B*, vol. 69, Feb 2004.
- [150] R. Samajdar, S. Choi, H. Pichler, M. D. Lukin, and S. Sachdev, “Numerical study of the chiral z_3 quantum phase transition in one spatial dimension,” *Physical Review A*, vol. 98, Aug 2018.
- [151] S. Whitsitt, R. Samajdar, and S. Sachdev, “Quantum field theory for the chiral clock transition in one spatial dimension,” *Physical Review B*, vol. 98, Nov 2018.
- [152] N. Chepiga and F. Mila, “Floating phase versus chiral transition in a 1d hard-boson model,” *Physical Review Letters*, vol. 122, Jan 2019.
- [153] S. Nyckees, J. Colbois, and F. Mila, “Identifying the huse-fisher universality class of the three-state chiral potts model,” *Nuclear Physics B*, vol. 965, p. 115365, Apr 2021.
- [154] R. J. Baxter, “Hard hexagons: exact solution,” *Journal of Physics A: Mathematical and General*, vol. 13, p. L61–L70, Mar 1980.
- [155] S. Alexander, “Lattice gas transition of the on a triangular lattice. a continuous transition with cubic terms,” *Physics Letters A*, vol. 54, p. 353–354, Oct 1975.
- [156] S. Nyckees and F. Mila, “Commensurate-incommensurate transition in the chiral ashkin-teller model,” *Phys. Rev. Research*, vol. 4, p. 013093, Feb 2022.
- [157] P. Bak, “Commensurate phases, incommensurate phases and the devil’s staircase,” *Reports on Progress in Physics*, vol. 45, p. 587–629, Jun 1982.
- [158] V. Nebendahl and W. Dür, “Improved numerical methods for infinite spin chains with long-range interactions,” *Physical Review B*, vol. 87, Feb 2013.
- [159] M. Rader and A. M. Läuchli, “Floating phases in one-dimensional rydberg ising chains,” *arXiv*, 2019.

- [160] N. Chepiga and F. Mila, “Kibble-zurek exponent and chiral transition of the period-4 phase of rydberg chains,” *Nature Communications*, vol. 12, Jan 2021.
- [161] J. Ashkin and E. Teller, “Statistics of two-dimensional lattices with four components,” *Physical Review*, vol. 64, p. 178–184, Sep 1943.
- [162] M. Kohmoto, M. den Nijs, and L. P. Kadanoff, “Hamiltonian studies of the $d=2$ ashkin-teller model,” *Phys. Rev. B*, vol. 24, pp. 5229–5241, Nov 1981.
- [163] A. O’Brien, S. D. Bartlett, A. C. Doherty, and S. T. Flammia, “Symmetry-respecting real-space renormalization for the quantum ashkin-teller model,” *Phys. Rev. E*, vol. 92, p. 042163, Oct 2015.
- [164] S. R. White, “Density matrix formulation for quantum renormalization groups,” *Physical Review Letters*, vol. 69, p. 2863–2866, Nov 1992.
- [165] J. Dukelsky, M. A. Martín-Delgado, T. Nishino, and G. Sierra, “Equivalence of the variational matrix product method and the density matrix renormalization group applied to spin chains,” *Europhysics Letters (EPL)*, vol. 43, p. 457–462, Aug 1998.
- [166] U. Schollwöck, “The density-matrix renormalization group in the age of matrix product states,” *Annals of Physics*, vol. 326, p. 96–192, Jan 2011.
- [167] R. N. C. Pfeifer, J. Haegeman, and F. Verstraete, “Faster identification of optimal contraction sequences for tensor networks,” *Phys. Rev. E*, vol. 90, p. 033315, Sep 2014.
- [168] I. P. McCulloch, “From density-matrix renormalization group to matrix product states,” *Journal of Statistical Mechanics: Theory and Experiment*, vol. 2007, pp. P10014–P10014, oct 2007.
- [169] J. Eisert, M. Cramer, and M. B. Plenio, “Colloquium: Area laws for the entanglement entropy,” *Rev. Mod. Phys.*, vol. 82, pp. 277–306, Feb 2010.
- [170] P. Calabrese and J. Cardy, “Entanglement entropy and conformal field theory,” *Journal of Physics A: Mathematical and Theoretical*, vol. 42, p. 504005, Dec 2009.

-
- [171] C. Hubig, I. P. McCulloch, U. Schollwöck, and F. A. Wolf, “Strictly single-site dmrg algorithm with subspace expansion,” *Phys. Rev. B*, vol. 91, p. 155115, Apr 2015.
- [172] G. M. Crosswhite, A. C. Doherty, and G. Vidal, “Applying matrix product operators to model systems with long-range interactions,” *Physical Review B*, vol. 78, Jul 2008.
- [173] B. Pirvu, V. Murg, J. I. Cirac, and F. Verstraete, “Matrix product operator representations,” *New Journal of Physics*, vol. 12, p. 025012, Feb 2010.
- [174] L. S. Ornstein and F. Zernike, “Accidental deviations of density and opalescence at the critical point of a single substance,” *Amsterdam Proc. Sec. Sci.*, vol. 17, p. 793, 1914.
- [175] A. A. Ovchinnikov, D. V. Dmitriev, V. Y. Krivnov, and V. O. Cheranovskii, “Antiferromagnetic ising chain in a mixed transverse and longitudinal magnetic field,” *Physical Review B*, vol. 68, dec 2003.
- [176] J. C. Bridgeman, A. O’Brien, S. D. Bartlett, and A. C. Doherty, “Multi-scale entanglement renormalization ansatz for spin chains with continuously varying criticality,” *Phys. Rev. B*, vol. 91, p. 165129, Apr 2015.
- [177] J. M. Luttinger, “An exactly soluble model of a many-fermion system,” *Journal of Mathematical Physics*, vol. 4, p. 1154–1162, Sep 1963.
- [178] D. C. Mattis and E. H. Lieb, “Exact solution of a many-fermion system and its associated boson field,” *Journal of Mathematical Physics*, vol. 6, p. 304–312, Feb 1965.
- [179] Y. Niu, S. B. Chung, C.-H. Hsu, I. Mandal, S. Raghu, and S. Chakravarty, “Majorana zero modes in a quantum ising chain with longer-ranged interactions,” *Physical Review B*, vol. 85, Jan 2012.
- [180] W. DeGottardi, M. Thakurathi, S. Vishveshwara, and D. Sen, “Majorana fermions in superconducting wires: Effects of long-range hopping, broken time-reversal symmetry, and potential landscapes,” *Phys. Rev. B*, vol. 88, p. 165111, Oct 2013.
- [181] A. Alecce and L. Dell’Anna, “Extended kitaev chain with longer-range hopping and pairing,” *Phys. Rev. B*, vol. 95, p. 195160, May 2017.

-
- [182] M. Thakurathi, A. A. Patel, D. Sen, and A. Dutta, “Floquet generation of majorana end modes and topological invariants,” *Physical Review B*, vol. 88, Oct 2013.
 - [183] P. Molignini, W. Chen, and R. Chitra, “Universal quantum criticality in static and floquet-majorana chains,” *Phys. Rev. B*, vol. 98, p. 125129, Sep 2018.
 - [184] P. Molignini, E. van Nieuwenburg, and R. Chitra, “Sensing floquet-majorana fermions via heat transfer,” *Phys. Rev. B*, vol. 96, p. 125144, Sep 2017.
 - [185] R. Ghosh, A. Sen, and K. Sengupta, “Ramp and periodic dynamics across non-ising critical points,” *Phys. Rev. B*, vol. 97, p. 014309, Jan 2018.

- Are you sure you lost them here?
- Oh no, I lost them in the park!
- Then why would you search here?
- Well, here we have light, of course.